

Cover Page



Universiteit Leiden



The handle <http://hdl.handle.net/1887/62452> holds various files of this Leiden University dissertation

Author: Heer, Paul de

Title: Advanced imaging and spectroscopy techniques for body magnetic resonance

Date: 2018-05-23



**ADVANCED
IMAGING AND
SPECTROSCOPY
TECHNIQUES FOR
BODY MAGNETIC
RESONANCE**

PAUL DE HEER

COLOFON

© 2018 Paul de Heer
Leiden, the Netherlands

All rights reserved. No part of this book may be reproduced or transmitted in any form or by any means without permission if the copyright owner. Copyright of the published chapters is held by the publisher of the journal in which the work appeared.

The research in this thesis was supported by the Nederlands Organisatie voor Wetenschappelijk Onderzoek TOP grant and the Dutch Kidney Foundation.

Financial support by the Dutch Heart Foundation and the Dutch Kidney Foundation for the publication of this thesis is gratefully acknowledged

ISBN

978-94-90858-56-8

Printing & dtp

Drukkerij Mostert & Van Onderen, Leiden
drukkerijmostert.nl

Design & concept

dennisdegraaff.nl
dennis-degraaff.squarespace.com

**ADVANCED
IMAGING
AND
SPECTRO-
SCOPY
TECHNIQUES
FOR BODY
MAGNETIC
RESONANCE**

Promotiecommissie

Promotores

Prof. Dr. A.G. Webb

Prof. Dr. H.J. Lamb

Copromotor

Dr. A.P.J. de Vries

Leden promotiecommissie

Prof. Dr. B.P.F. Lelieveldt

Prof. Dr. T. Leiner (Universitair Medisch Centrum Utrecht)

Dr. M.J. Versluis (Philips Medical Systems International B.V)

Dr. H.E. Kan

**Advanced Imaging and Spectroscopy
Techniques for Body Magnetic Resonance**

Proefschrift

ter verkrijging van
de graad van Doctor aan de Universiteit Leiden,
op gezag van Rector Magnificus prof.mr. C.J.J.M. Stolker,
volgens besluit van het College voor Promoties
te verdedigen op woensdag 23 mei 2018
klokke 13:45 uur

door

Paul de Heer

geboren te Heemskerk

in 1983

**1 GENERAL
INTRODUCTION**
PAGE 9

**MR OF
MULTI-ORGAN
INVOLVEMENT IN
THE METABOLIC
SYNDROME**
PAGE 25

**INCREASING
SIGNAL HOMO-
GENEITY AND IMAGE
QUALITY IN ABDOMI-
NAL IMAGING AT 3T
WITH VERY HIGH
PERMITTIVITY
MATERIALS**
PAGE 39

**IMPROVED
CARDIAC PROTON
MAGNETIC RESONANCE
SPECTROSCOPY AT 3T
USING HIGH PERMITTI-
VITY PADS**
PAGE 51

**PARAMETER
OPTIMIZATION
FOR REPRODUCIBLE
CARDIAC ¹H-MR
SPECTROSCOPY
AT 3 TESLA**
PAGE 71

**IMAGING
FATTY KIDNEY BY
CLINICAL PROTON
MAGNETIC RESONANCE
SPECTROSCOPY:
A FIRST VALIDATION
AND DIETARY INTER-
VENTION STUDY USING
PORCINE KIDNEYS**
PAGE 109

**DUTCH SUMMARY /
NEDERLANDSE
SAMENVATTING**
PAGE 137

**APPENDICES:
LIST OF PUBLICATIONS
ACKNOWLEDGEMENTS
CURRICULUM VITAE**
PAGE 141

**METABOLIC IMAGING
OF HUMAN KIDNEY
TRIGLYCERIDE
CONTENT:
REPRODUCIBILITY OF
PROTON MAGNETIC
RESONANCE
SPECTROSCOPY**
PAGE 97

**SUMMARY
AND GENERAL
DISCUSSION**
PAGE 127

1

**GENERAL
INTRODUCTION**

INTRODUCTION

Towards High Field Body MR

Since Goldsmith et al. performed the first successful body Magnetic Resonance Imaging (MRI) scan in 1977 (Figure 1) much effort has been put into improving the (diagnostic) quality of body MR images. This improvement has been realized through enhanced gradient systems, receive/transmit coils, and pulse sequences, as well as, increased field strength of the MR systems. By increasing the field strength of the MR scanner a larger effective magnetization of the spins is produced resulting in an increase in the signal-to-noise ratio (SNR). Furthermore, with increasing field strength, the contrast of the images change, specifically when using contrast agents, creating new scanning possibilities.

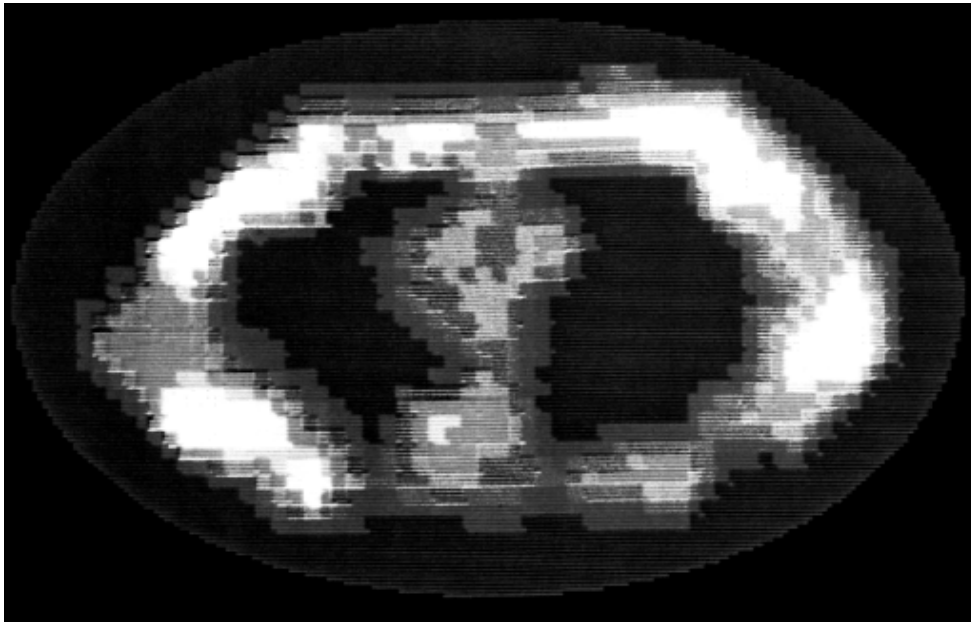


FIGURE 1: First MRI body image recorded by Goldsmith et al. By today's standards this image has an extremely low (coarse) resolution, however, basic structures like the heart and lungs are visible in the image.

High Field Advantages

In the early days, when Goldsmith recorded his first body MR image, field strengths of the scanners were well below 0.5 Tesla (T). In the following years, the field strength of clinical body MR scanners increased to 1.5 T increasing SNR and thereby improving image quality.

In the last decade, high field scanners (defined as ≥ 3 T) are increasingly used in clinical practice. High field systems are favoured over 1.5 T systems for multiple applications because of the higher SNR it provides. The additional SNR can be used to increase the resolution for imaging smaller structures (pathologies). Alternatively, the increase in SNR allows for a reduction in scan time by lowering the number of signal averages (NSA). Furthermore, high field systems can reduce acquisition time even further due to increased performance of parallel imaging methods (e.g. Spatial Encoding Using Multiple

Radio Frequency Coils, SENSitivity Encoding, GeneRALized Autocalibrating Partial Parallel Acquisition) at higher field strength.¹⁻³ Due to the changes in contrast at higher field imaging, an increased efficacy of contrast agents, such as gadolinium (percentage T1 reduction due to gadolinium is higher), makes higher field strength more suitable for dynamic contrast enhancement (DCE) scans. Furthermore, functional neuroimaging can benefit of an increased Blood-oxygen-level dependent contrast (BOLD) response due to stronger spin-spin interaction (lower T2*) enabled by a stronger magnetic field.^{4,5} In MR spectroscopy, separation of the resonance frequencies improves due to an increased chemical shift resulting in improved spectral quality and specificity.

Challenges for High Field Body MR

Despite these clear advantages of higher field scanners, clinical body imaging is still predominantly performed on 1.5 T MR scanners since the advantages previously described are not yet fully translated to clinical practice.

The main reason for this is the increase in imaging artefacts often accompanied by a higher magnetic field strength. Such artefacts are often caused by an increase in; transmit field (B_1^+) inhomogeneities (dielectric effects), static field (B_0) inhomogeneities, motion artefacts (respiratory, cardiac and bowel) and susceptibility effects. When comparing field strengths of 1.5 T and 3 T in cardiac functional imaging, Michaely et al (2006) observed only a minimal increase in SNR at 3 T.⁶ Greenman et al. (2003) reported that blood suppression was comparable between 1.5 T and 3 T systems in cardiac imaging.⁷ However, a decrease in SNR was found in the myocardial wall for 3 T compared to 1.5 T. This decrease in SNR was mainly attributed to the variance in the B_1^+ field. Furthermore, studies comparing 1.5 T to 3 T often report an increase in imaging artefacts.⁸ Specifically artefacts caused by increased sensitivity to motion and increased magnetic susceptibility, but also B_1^+ field inhomogeneities are observed.^{9,10} Another important factor to consider when moving from 1.5 T to 3 T is that the Specific Absorption Rate (SAR) will be four times higher since this is quadratically related to the magnetic field strength.^{11,12} This could complicate transferring a scan sequence from 1.5 T to 3 T since the radio frequency (RF) heating limits can be reached and changes have to be made to stay within the SAR constraints.⁶

All these challenges clearly demonstrate that it is complicated to fully exploit the theoretical advantages of higher field strengths. Additionally, the purchase and maintenance cost of high field scanners are significantly higher. Therefore, if these challenges are not addressed properly, the benefits of a higher magnetic field strength will not outweigh the higher cost.

Transmit Field (B_1^+) Variations

As mentioned in the previous paragraph, transmit field inhomogeneity is a major contributor to artefacts with increasing field strength. These artefacts represented by hyper and hypo intense areas in the image (Figure 2). This inhomogeneous B_1^+ field results in signal voids in the image and has been reported by multiple researchers.^{8,13-16} As stated by Bernstein "Image shading and uneven contrast resulting from spatial variation in the transmit B_1^+ field remains one of the biggest unsolved problems for routine clinical 3 T imaging today".⁸ This inhomogeneity is even more prominent in patients with ascites but also in pregnant women resulting in these populations to be scanned at lower field strengths (1.5 T).

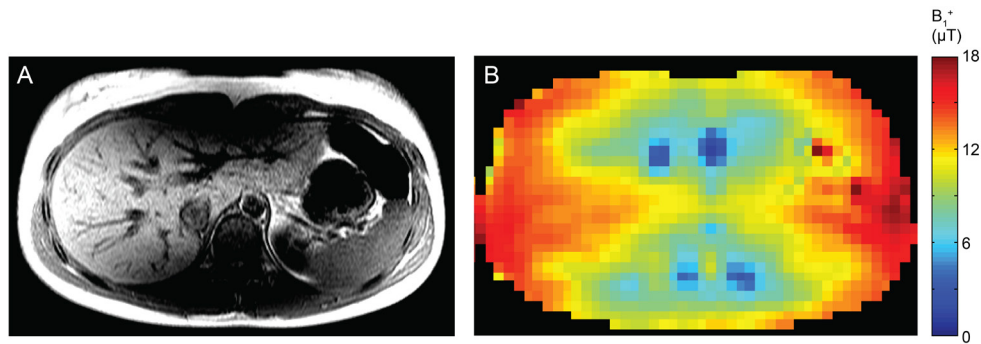


FIGURE 2: (A) T1-weighted turbo-spin echo image at 3 T with clear image hypo and hyper intensities caused by an inhomogeneous transmit field.

(B) The corresponding transmit field map shows a low transmit field in the areas where the T1-weighted image has strong hypo intensities.

When looking at an unloaded birdcage coil the transmit field is very homogeneous for both the 1.5 and 3 T scanners. However, when a lossy object like the body is placed in the coil, the disturbance introduced by the body will cause the transmit field to be less homogeneous. This disturbance of the field is caused by a shortening of the wavelength in the body as well as attenuation of the transmit field. This is often referred to as the standing wave effect which becomes problematic when the wavelength of the transmit signal is equal or smaller than the size of the object imaged (wavelength in muscle tissue at 3 T \approx 29cm). Both the wavelength as well as the attenuation is dependent on the field strength, with a more severe disturbance at higher field strength scanners.

MR manufacturers recognize the problem of B_1^+ inhomogeneities and are addressing it by using multi transmit set-ups. Such a multi transmit splits the standard quadrature body coil in effectively two (or more) linear transmit coils that can be independently driven with an optimized phase and amplitude. The two degrees of freedom (relative amplitudes and relative phases of the two channels) compared to only one (absolute amplitude) for a conventional single transmit system can produce considerable increases in RF transmit homogeneity^{17,18} which has long been known theoretically and investigated extensively for imaging at ultra-high field (7 T).^{19–21} Despite improved performance with dual-channel systems, it does not consistently solve the problem of image inhomogeneities. Experimental and simulation work has suggested that further improvement is possible using an eight channel transmit body coil, but such a setup is currently not commercially available.^{22,23}

A second approach to address the issue of transmit field inhomogeneity in 3 T body imaging is the use of “dielectric pads”.^{24–27} Dielectric materials have a strong impact on the magnetic field. The extent of this effect is determined by the shape and material properties (specifically permittivity and conductivity) of these dielectrics. When a dielectric material is carefully designed it can be used to correct the inhomogeneous RF field to make it more homogeneous. Furthermore, it can increase the receive sensitivity, resulting in increased SNR. Previously these pads were made from ultrasound gel (low relative permittivity, $\mu_r < 100$) with dissolved paramagnetics, such as manganese chloride, to

provide a short T2 and hence low background MR signal. Some institutions reported that such dielectric pads are used locally for most abdominal scans²⁵, whereas others report that they are not commonly used in the wider community.⁸ Recently it was proposed that new high dielectric materials, including calcium titanate and barium titanate, would have more freedom in shaping the transmit field.^{28,29} Furthermore, compared to the pads made of low permittivity materials, these pads can be made thinner which facilitates their application (Figure 3).



FIGURE 3: Example of a high dielectric pad placed on the liver. With this high dielectric pad it is possible to shape the transmit field to make it more homogeneous.

MR Spectroscopy

MR spectroscopy is a technique often used in research applications in body MR since it enables assessment of metabolites in the body. Instead of measuring the (water) proton densities (as in MR imaging) it is possible to measure separate metabolites and to quantify the abundance of such a metabolite. Commonly measured metabolites are triglyceride and creatine which play an important role in various diseases (e.g. metabolic syndrome and cardiovascular disease).^{30–33}

However, as in MR imaging, it is challenging to translate MR spectroscopy to higher field scanners. Challenges such as an increase in transmit field (B_1^+) in-homogeneities, static field (B_0) inhomogeneities, motion artefacts (respiratory, cardiac and bowel) and susceptibility effects previously described, apply here as well. In several MR spectroscopy studies it has been shown that the potential benefits (increased SNR, better metabolite separation) are not fully utilized. For example, in brain spectroscopy a comparison between 1.5 T and 3 T Barker et al. (2001) showed an increase in SNR of only 28% and 6% of the N-acetylaspartate signal, where a gain of 100% would be expected.³⁴ In a second study comparing 1.5 T and 3 T spectroscopy, in both patients with mild cognitive impairment and patients with Alzheimer disease, there was no advantage in diagnostic value when using a higher field strength.¹⁰ Both studies acclaimed the lower SNR gain to broader linewidths stressing the need for better static magnetic field (B_0) shimming methods at higher field. Another study that measured myocardial lipids showed an SNR gain of 76% for in-vivo and 45% for ex-vivo measurements, also not reaching the theoretical 100% SNR gain of doubling the scanner field strength. This suboptimal increase in SNR was also attributed to B_0 inhomogeneity as well as an increase in susceptibility and motion artefacts.³⁵

Overall, body MR spectroscopy can be a challenging technique to perform specifically on high field scanners. This can also be seen from the studies that were performed to test reproducibility of the technique.^{31,33,36–42} In the liver the reproducibility (coefficient of

variation) ranged from 3.6% to 10% while in the heart it ranged from 6.5% to 18%. This shows that the reproducibility of spectroscopy varies strongly between organs but also between studies themselves. No studies evaluating the reproducibility of renal ^1H -MR spectroscopy for detection of renal triglyceride content had been performed prior to this thesis.

MR spectroscopy background

To understand why MR spectroscopy can be challenging to perform, specifically at high field, some background information is needed. By placing an object in a strong external magnetic field the protons in the object will align with the direction of this field. The protons will also precess (rotate around the magnetic field direction) at a frequency ω_0 that depends on the strength of the magnetic field B_0 as well as the gyromagnetic ratio γ .

$$\omega_0 = \gamma B_0 \quad (\text{Equation 1})$$

The gyromagnetic ratio γ is a constant and is 42.6 MHz/T for hydrogen protons. In an average clinical scanner with a field strength of 1.5 T the hydrogen protons will precess at 64 MHz. To interact with the protons in the object an RF pulse with the same frequency as the precession frequency (resonance frequency) of the protons is transmitted. The magnetization of the protons then rotates from the longitudinal plane into the transversal plane. When the RF pulse excitation ends, the magnetization of the protons will slowly return to their natural state in the direction of the applied magnetic field. During this relaxation process the object transmits a signal which can be measured by the MR scanner. By applying a Fourier transformation, the received signal is transferred from time domain into its separate frequency components.

Chemical shift

As mentioned before protons will precess at a frequency described by equation 1. However, if all protons would always precess at the same frequency we would see only one single peak in the MR spectroscopy frequency spectrum not allowing us to discriminate between different metabolites. However, the precession frequency is not solely dependent on the applied magnetic field and the gyro-magnetic ratio. There is also a third component that describes the amount of electrons surrounding (chemical environment) the protons. The electrons surrounding a proton will shield it from the external magnetic field thereby lowering the precession frequency of the proton. The effect of shielding of the electrons can be expressed in a shielding constant σ and can be applied to equation 1 to determine the effective precession frequency.

$$\omega_0 = \gamma B_0(1 - \sigma) \quad (\text{Equation 2})$$

The phenomena that protons experience a different magnetic field dependent on their chemical environment is called chemical shift. In MR spectroscopy we can exploit this property to discriminate between different metabolites which have different chemical environments. When an MR spectroscopy experiment is performed the received signal (after Fourier transformation) will consist of multiple peaks with each peak representing protons in a certain type of environment. Figure 4 displays an example of a liver spectrum that consists of multiple peaks that represent different metabolites. Generally, the

chemical shift is expressed in parts per million (ppm) by dividing the precession frequency (in Hz) by the field strength of the scanner to create an output independent of the scanner field strength. Some structures, like triglyceride, consist of multiple moieties each with their own chemical environment and thus, resonance frequency. The most prominent resonances of triglyceride are CH_3 (0.9 ppm), $(\text{CH}_2)_n$ (1.3 ppm), $\text{CH}_2\text{CH} = \text{CHCH}_2$ and CH_2COO (2.1 ppm). By quantitatively measuring the concentrations of triglyceride in organs, assessment of cellular damage from lipotoxicity can be performed. Moreover, proton MRS enables measurement of metabolites involved in the energy supply of the body such as creatine (3 ppm). Furthermore, the amount of water (4.7 ppm) can be measured which is often used as an internal reference to quantify other metabolites.

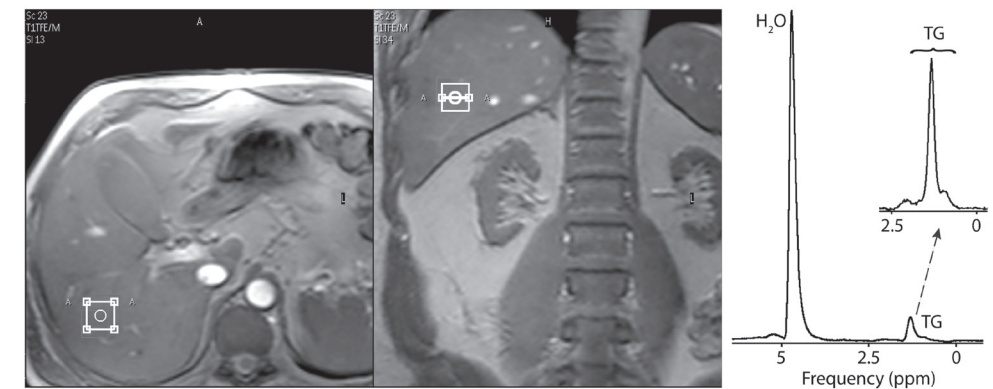


FIGURE 4: Example MR spectroscopy (single voxel) measurement in the liver with an elevated triglyceride water ratio ($>5\%$) compared to a healthy liver. The two images show the measurement location (white voxel) in the transverse and coronal direction. On the right the MR spectrum is shown with resonances of triglycerides (0.9, 1.3, 2.1 ppm) and water (4.7 ppm).

Even though MR spectroscopy is one of the few techniques that enables quantification of various metabolites in the body, clinical applications are currently limited to neurology, and more recently, the prostate.⁴³⁻⁴⁵ Body MR spectroscopy applications are still restricted to the research domain due to the fact that it is a challenging technique to perform reliably. This is due to problems described earlier such as transmit field fluctuations, static field fluctuations as well as an inherent low SNR of the metabolites of interest.

Clinical applications of high field body MR - Metabolic Syndrome

Data of the International Diabetes Federation (IDF) shows that a quarter of the world's adult population meets the criteria for Metabolic Syndrome (MetS).⁴⁶ The IDF defined metabolic syndrome as "a cluster of the most dangerous risk factors including diabetes and prediabetes, abdominal obesity, high cholesterol and high blood pressure" increasing the risk of serious health problems like diabetes, heart failure, non-alcoholic liver disease, renal failure and stroke.⁴⁷

- Raised plasma triglyceride level; > 150 mg/dL (> 1.7 mmol/L)
- Reduced plasma HDL cholesterol; < 40 mg/dL (1.03 mmol/L) in males and < 50 mg/dL (< 1.29 mmol/L) in females
- Raised blood pressure; systolic BP ≥ 130 or diastolic BP ≥ 85 mm Hg
- Raised fasting plasma glucose; ≥ 100 mg/dL (≥ 5.6 mmol/L)

Due to the globally increasing prevalence of obesity, as well as higher life expectancy, MetS is increasingly diagnosed as it is correlated with elevated body mass index as well as advancing age.

Although the exact underlying cause of MetS is still not fully understood, insulin resistance is considered to be a significant factor in the development of MetS. Insulin is a hormone which is produced by beta-cells in the pancreas to facilitate uptake of glucose from the blood into tissue such as liver, kidney and muscle cells. When the body becomes less sensitive to insulin, the uptake of glucose from the blood is reduced, resulting in high

blood glucose levels. To compensate for these increased blood glucose levels, the beta-cells increase insulin production. This in turn increases the load on the beta-cells until the maximum insulin production is reached and glucose builds up in the blood. This effect is labelled hyperglycemia and is linked to excessive triglyceride levels in parts of the body including the liver, skeletal muscle, and heart, and renal tissue. Such raised lipids levels, described as ectopic fat deposition, interfere with cellular function and can cause cell death through a phenomena known as lipotoxicity, which plays an important role in the pathogenesis of MetS [Figure 5].^{30,48}

Hallmarks of MetS in the heart, liver and kidney

A description of the full extent of the impact of MetS on the body is beyond the scope of this thesis and therefore, we focused on the three primarily affected organs; the heart, liver and kidney.

In the heart elevated myocardial triglyceride content has been linked to an increased chance of heart failure.^{49,50} As shown in animal studies, increased storage of myocardial triglyceride reflects an abundance of toxic lipids that impair cardiomyocyte integrity and function. Myocardial steatosis may be an early sign of diabetic cardiomyopathy, because it is an independent predictor of diastolic dysfunction.

In the liver, the blood glucose is converted into glycogen or fatty acids which serve as an energy source. However, when excessive glucose is present in the blood, it will be converted to vacuoles of triglyceride lipid and stored in the liver cells. This process is called hepatic steatosis and is diagnosed in case a liver biopsy shows that more than five percent of the hepatocytes contain vacuoles of triglyceride lipid. If hepatic steatosis is not treated it can progress to non alcoholic steatotic hepatitis (NASH), characterized by inflammation of the hepatocytes. A quarter of patients with NASH develop fibrosis (scarring of the liver tissue).⁵¹ In a subgroup of these patients, NASH eventually results in cell death of the hepatocytes (necrosis) which often necessitates a liver transplant.

How MetS, in particular obesity, can lead to incipient chronic kidney disease remains unclear. Recently ectopic lipid accumulation in the kidney (fatty kidney) has been proposed as a potential pathway.⁵²⁻⁵⁵ Notably, obesity and type 2 diabetes have been associated with renal lipid accumulation in both human and porcine kidneys with differences in anatomical distribution between glomeruli and tubuli, as well as the cortex and medulla.^{53,56} Increased renal lipid content has also been linked to functional and structural renal hyperfiltration, obesity-related glomerulopathy, and type 2 diabetic nephropathy.^{52,56-57} Various rodent models have shown that intervention in cellular lipid pathways attenuated obesity-related glomerulopathy or diet-induced chronic kidney disease.⁵⁸

At present, MetS is diagnosed by a cluster of the most dangerous risk factors. Several organizations have described such criteria (eg. IDF, WHO, ADA) and even though these diagnostic criteria are not the same they often include factors like prediabetes, abdominal obesity, high cholesterol and high blood pressure. However, these criteria provide limited information to what extent the different organs are affected. To improve treatment strategies, organ-specific (imaging) biomarkers are needed to gain more insight in the underlying mechanisms and risk stratification of MetS. Since many disease pathologies related to MetS are believed to be closely correlated to the increased storage of lipids in the organs, shown to be a precursor for lipotoxicity, a reliable technique to measure the amount of ectopic lipids in the organs is highly needed.

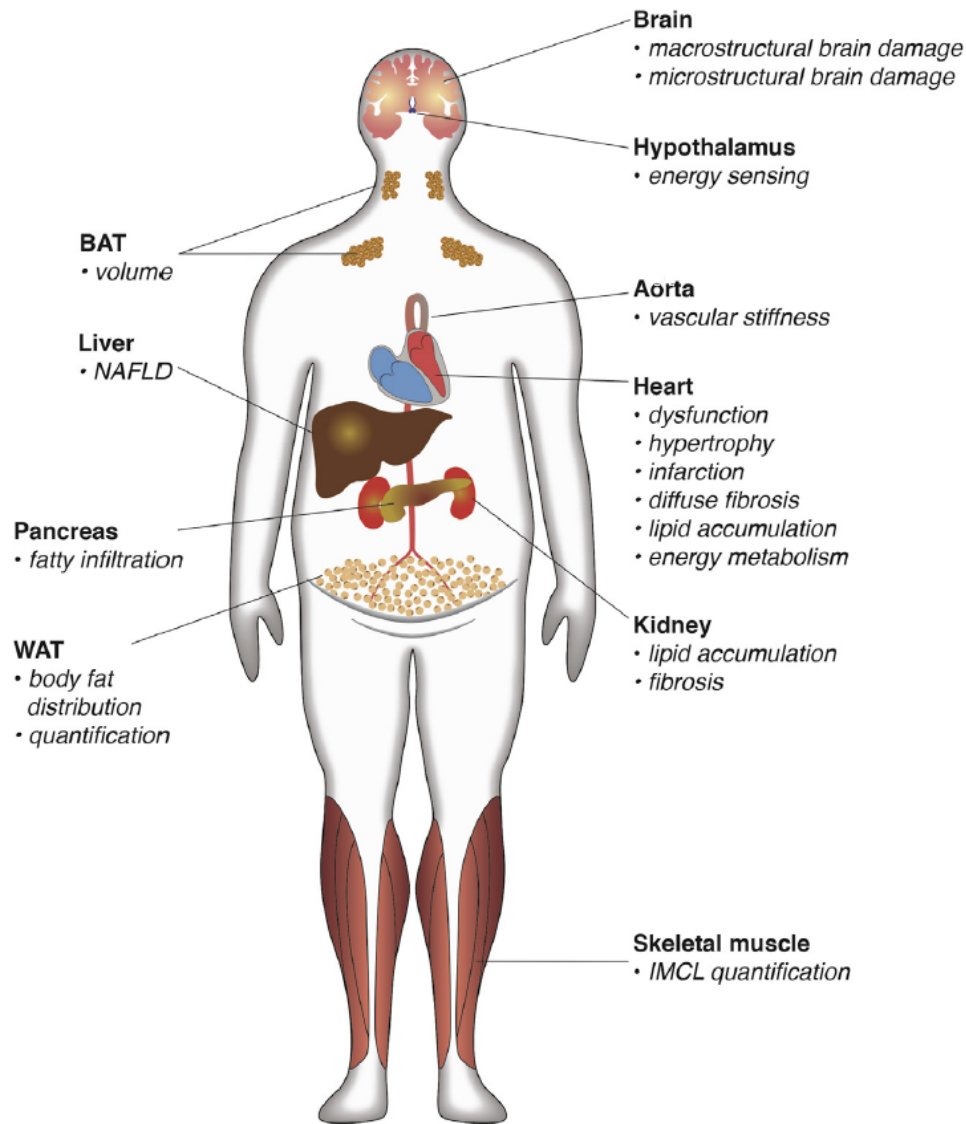


FIGURE 5: Extent of impact of metabolic syndrome that can be measured using MR. (Magnetic Resonance Imaging Clinics of North America 2015 Feb;23(1):41-58, with permission.)

AIM OF THIS THESIS

The aim of this thesis is to further develop advanced body MR techniques to gain more insight in the metabolic syndrome (MetS). This was realized by optimizing MR imaging and spectroscopy measurements in the body, as well as ex-vivo. One of the optimization steps includes development of high dielectric materials to increase sensitivity of the body MR measurements.

OUTLINE OF THIS THESIS

In **Chapter one** a general introduction is given to body MR and the challenges of high field body MR are discussed. Basic background information for dielectric pads is given, which can be applied to address a major challenge of high field body MR. Moreover some basic principles of MR spectroscopy are explained. Furthermore, the metabolic syndrome and the use of high field body MR to evaluate this syndrome are described. In the first part of this thesis we aimed to develop new techniques for high field body MR which are described in chapters two, three, and four. **Chapter two** (Increasing Signal Homogeneity and Image Quality in Abdominal Imaging at 3 T with Very High Permittivity Materials) examines whether inhomogeneous transmit fields (a major challenge in high field body MR), can be improved by passive shimming. High dielectric materials were designed, simulated and tested for liver imaging to increase image quality. **Chapter three** (Improved Cardiac Proton Magnetic Resonance Spectroscopy at 3 T Using High Permittivity Pads) demonstrates how a similar passive shimming approach can be applied in cardiac spectroscopy to increase the SNR of the spectra. In **Chapter four** (Parameter Optimization for Reproducible Cardiac ¹H-MR Spectroscopy at 3 Tesla) we investigated how cardiac proton MR spectroscopy measurements can be optimized for high field and reports results on reproducibility. In the second part of this thesis, consisting of chapters five, six and seven, the techniques described in chapters 2, 3 and 4 are applied in clinical studies in order to gain additional insight in the development/treatment of the Metabolic Syndrome (MetS). In **Chapter five** (MR of Multi-Organ Involvement in the Metabolic Syndrome) a review is presented on multi-organ involvement in the metabolic syndrome and how this can be evaluated using magnetic resonance techniques. **Chapter six** (Metabolic Imaging of Human Kidney Triglyceride Content: Reproducibility of Proton Magnetic Resonance Spectroscopy) reports the results of a feasibility study of in-vivo renal proton MR spectroscopy and describes the reproducibility of this measurement. **Chapter seven** (Imaging Fatty Kidney by Clinical Proton Magnetic Resonance Spectroscopy (¹H-MRS): a First Validation and Dietary Intervention Study using Porcine Kidneys) validates renal proton MR spectroscopy in comparison to biopsies in porcine kidneys. Furthermore, the effects of dietary intervention on renal lipids are assessed. In **Chapter eight** all chapters are summarized and discussed.

REFERENCES

- Sodickson DK, Manning WJ. Simultaneous acquisition of spatial harmonics (SMASH): Fast imaging with radiofrequency coil arrays. *Magn Reson Med*. 1997;38(4):591-603. doi:10.1002/mrm.1910380414.
- Pruessmann KP, Weiger M, Scheidegger MB, Boesiger P. ¹H-SENSE sensitivity encoding for fast MRI.pdf. *Magn Reson Med Off J Soc Magn Reson Med / Soc Magn Reson Med*. 1999;42(5):952-962. <http://www.ncbi.nlm.nih.gov/pubmed/10542355>.
- Griswold MA, Jakob PM, Heidemann RM, et al. Generalized Autocalibrating Partially Parallel Acquisitions (GRAPPA). *Magn Reson Med*. 2002;47(6):1202-1210. doi:10.1002/mrm.10171.
- Jesmanowicz A, Bandettini PA, Hyde JS. Single-shot half k-space high-resolution gradient-recalled EPI for fMRI at 3 Tesla. *Magn Reson Med*. 1998;40(5):754-762. doi:10.1002/mrm.1910400517.
- Krüger G, Kastrup A, Glover GH. Neuroimaging at 1.5 T and 3.0 T: Comparison of oxygenation-sensitive magnetic resonance imaging. *Magn Reson Med*. 2001;45(4):595-604. doi:10.1002/mrm.1081.
- Michaely HJ, Nael K, Schoenberg SO, et al. Analysis of cardiac function - Comparison between 1.5 tesla and 3.0 tesla cardiac cine magnetic resonance imaging: Preliminary experience. *Invest Radiol*. 2006;41(2):133-140. doi:10.1097/01.rli.0000192023.96494.af.
- Greenman RL, Shirosky JE, Mulkern RV, Rofsky NM. Double inversion black-blood fast spin-echo imaging of the human heart: A comparison between 1.5T and 3.0T. *J Magn Reson Imaging*. 2003;17(6):648-655. doi:10.1002/jmri.10316.
- Bernstein MA, Huston J, Ward HA. Imaging artifacts at 3.0T. *J Magn Reson Imaging*. 2006;24(4):735-746. doi:10.1002/jmri.20698.
- Kuhl CK, Textor J, Gieseke J, et al. Acute and subacute ischemic stroke at high-field-strength [3.0-T] diffusion-weighted MR imaging: intraindividual comparative study. *Radiology*. 2005;234(2):509-516. doi:10.1148/radiol.2342031323.
- Kantarci K, Reynolds G, Petersen RC, et al. Proton MR spectroscopy in mild cognitive impairment and Alzheimer disease: comparison of 1.5 and 3 T. *AJNR Am J Neuroradiol*. 2003;24(5):843-849. doi:10.3174/ajnr.A1192.
- Collins CM, Smith MB. Signal-to-noise ratio and absorbed power as functions of main magnetic field strength, and definition of "90°" RF pulse for the head in the birdcage coil. *Magn Reson Med*. 2001;45(4):684-691. doi:10.1002/mrm.1091.
- Vaughan JT, Garwood M, Collins CM, et al. 7T vs. 4T: RF power, homogeneity, and signal-to-noise comparison in head images. *Magn Reson Med*. 2001;46(1):24-30. doi:10.1002/mrm.1156.
- Cornfeld D, Weinreb J. Simple changes to 1.5-T MRI abdomen and pelvis protocols to optimize results at 3 T. *AJR Am J Roentgenol*. 2008;190(2):140-150. doi:10.2214/AJR.07.2903.
- Dietrich O, Reiser MF, Schoenberg SO. Artifacts in 3-T MRI: Physical background and reduction strategies. *Eur J Radiol*. 2008;65(1):29-35. doi:10.1016/j.ejrad.2007.11.005.
- Yang RK, Roth CG, Ward RJ, deJesus JO, Mitchell DG. Optimizing Abdominal MR Imaging: Approaches to Common Problems. *RadioGraphics*. 2010;30(1):185-199. doi:10.1148/rg.301095076.
- Merkle EM, Dale BM. Abdominal MRI at 3.0 T: the basics revisited. *AJR Am J Roentgenol*. 2006;186(6):1524-1532. doi:10.2214/AJR.05.0932.
- Nelles M, König RS, Gieseke J, et al. Dual-source parallel RF transmission for clinical MR imaging of the spine at 3.0 T: intraindividual comparison with conventional single-source transmission. *Radiology*. 2010;257(3):743-753. doi:10.1148/radiol.10092146.
- Willinek WA, Gieseke J, Kukuk GM, et al. Dual-source parallel radiofrequency excitation body MR imaging compared with standard MR imaging at 3.0 T: initial clinical experience. *Radiology*. 2010;256(3):966-975. doi:10.1148/radiol.10092127.
- Adriany G, Van de Moortele P-F, Wiesinger F, et al. Transmit and receive transmission line arrays for 7 Tesla parallel imaging. *Magn Reson Med*. 2005;53(2):434-445. doi:10.1002/mrm.20321.
- Vaughan JT, Snyder CJ, DelaBarre LJ, et al. Whole-body imaging at 7T: Preliminary results. *Magn Reson Med*. 2009;61(1):244-248. doi:10.1002/mrm.21751.
- Kraff O, Bitz AK, Kruszona S, et al. An eight-channel phased array RF coil for spine MR imaging at 7 T. *Invest Radiol*. 2009;44(11):734-740. doi:10.1097/RLI.0b013e-3181b24ab7.
- Van den Berg CAT, van den Bergen B, Van de Kamer JB, et al. Simultaneous B1 + homogenization and specific absorption rate hotspot suppression using a magnetic resonance phased array transmit coil. *Magn Reson Med*. 2007;57(3):577-586. doi:10.1002/mrm.21149.
- Vernickel P, Röschmann P, Findelee C, et al. Eight-channel transmit/receive body MRI coil at 3T. *Magn Reson Med*. 2007;58(2):381-389. doi:10.1002/mrm.21294.

24. Franklin KM, Dale BM, Merkle EM. Improvement in B1-inhomogeneity artifacts in the abdomen at 3T MR imaging using a radiofrequency cushion. *J Magn Reson Imaging*. 2008;27(6):1443-1447. doi:10.1002/jmri.21164.
25. Sreenivas M, Lowry M, Gibbs P, Pickles M, Turnbull LW. A simple solution for reducing artefacts due to conductive and dielectric effects in clinical magnetic resonance imaging at 3T. *Eur J Radiol*. 2007;62(1):143-146. doi:10.1016/j.ejrad.2006.11.014.
26. Takayama Y, Nonaka H, Nakajima M, Obata T, Ikehira H. Reduction of a high-field dielectric artifact with homemade gel. *Magn Reson Med Sci*. 2008;7(1):37-41. <http://www.ncbi.nlm.nih.gov/pubmed/18460847>. Accessed August 21, 2017.
27. Kataoka M, Isoda H, Maetani Y, et al. MR imaging of the female pelvis at 3 Tesla: evaluation of image homogeneity using different dielectric pads. *J Magn Reson Imaging*. 2007;26(6):1572-1577. doi:10.1002/jmri.21173.
28. Teeuwisse WM, Brink WM, Haines KN, Webb AG. Simulations of high permittivity materials for 7 T neuroimaging and evaluation of a new barium titanate-based dielectric. *Magn Reson Med*. 2012;67(4):912-918. doi:10.1002/mrm.24176.
29. Teeuwisse WM, Brink WM, Webb AG. Quantitative assessment of the effects of high-permittivity pads in 7 Tesla MRI of the brain. *Magn Reson Med*. 2012;67(5):1285-1293. doi:10.1002/mrm.23108.
30. Iozzo P. Myocardial, perivascular, and epicardial fat. *Diabetes Care*. 2011;34 Suppl 2(Supplement_2):S371-9. doi:10.2337/dc11-s250.
31. Machann J, Stefan N, Schick F. (1)H MR spectroscopy of skeletal muscle, liver and bone marrow. *Eur J Radiol*. 2008;67(2):275-284. doi:10.1016/j.ejrad.2008.02.032.
32. Lee SS, Park SH. Radiologic evaluation of nonalcoholic fatty liver disease. *World J Gastroenterol*. 2014;20(23):7392. doi:10.3748/wjg.v20.i23.7392.
33. van der Meer RW, Doornbos J, Kozerke S, et al. Metabolic imaging of myocardial triglyceride content: reproducibility of 1H MR spectroscopy with respiratory navigator gating in volunteers. *Radiology*. 2007;245(1):251-257. doi:10.1148/radiol.2451061904.
34. Barker PB, Hearshen DO, Boska MD. Single-voxel proton MRS of the human brain at 1.5 T and 3.0 T. *Magn Reson Med*. 2001;45(5):765-769.
35. Venkatesh BA, Lima JAC, Bluemke DA, Lai S, Steenbergen C, Liu CY. MR proton spectroscopy for myocardial lipid deposition quantification: A quantitative comparison between 1.5T and 3T. *J Magn Reson Imaging*. 2012;36(5):1222-1230. doi:10.1002/jmri.23761.
36. Johnson NA, Walton DW, Sachinwalla T, et al. Noninvasive assessment of hepatic lipid composition: Advancing understanding and management of fatty liver disorders. *Hepatology*. 2008;47(5):1513-1523. doi:10.1002/hep.22220.
37. Szczepaniak LS, Nurenberg P, Leonard D, et al. Magnetic resonance spectroscopy to measure hepatic triglyceride content: prevalence of hepatic steatosis in the general population. *Am J Physiol Endocrinol Metab*. 2005;288(2):E462-8. doi:10.1152/ajpendo.00064.2004.
38. Thomas EL, Hamilton G, Patel N, et al. Hepatic triglyceride content and its relation to body adiposity: a magnetic resonance imaging and proton magnetic resonance spectroscopy study. *Gut*. 2005;54(1):122-127. doi:10.1136/gut.2003.036566.
39. van Werven JR, Hoogduin JM, Nederveen AJ, et al. Reproducibility of 3.0 Tesla magnetic resonance spectroscopy for measuring hepatic fat content. *J Magn Reson Imaging*. 2009;30(2):444-448. doi:10.1002/jmri.21837.
40. Felblinger J, Jung B, Slotboom J, Boesch C, Kreis R. Methods and reproducibility of cardiac/respiratory double-triggered (1)H-MR spectroscopy of the human heart. *Magn Reson Med*. 1999;42(5):903-910. <http://www.ncbi.nlm.nih.gov/pubmed/10542349>. Accessed August 24, 2017.
41. Szczepaniak LS, Dobbins RL, Metzger GJ, et al. Myocardial triglycerides and systolic function in humans: in vivo evaluation by localized proton spectroscopy and cardiac imaging. *Magn Reson Med*. 2003;49(3):417-423. doi:10.1002/mrm.10372.
42. Ith M, Stettler C, Xu J, Boesch C, Kreis R. Cardiac lipid levels show diurnal changes and long-term variations in healthy human subjects. *NMR Biomed*. 2014;27(11):1285-1292. doi:10.1002/nbm.3186.
43. Thompson J, Lawrentschuk N, Frydenberg M, Thompson L, Stricker P. The role of magnetic resonance imaging in the diagnosis and management of prostate cancer. *BJU Int*. 2013;112(S2):6-20. doi:10.1111/bju.12381.
44. Barentsz JO, Richenberg J, Clements R, et al. ESUR prostate MR guidelines 2012. *Eur Radiol*. 2012;22(4):746-757. doi:10.1007/s00330-011-2377-y.
45. van der Graaf M. In vivo magnetic resonance spectroscopy: basic methodology and clinical applications. *Eur Biophys J*. 2010;39(4):527-540. doi:10.1007/s00249-009-0517-y.
46. National Cholesterol Education Program (NCEP) Expert Panel on Detection, Evaluation and T of HBC in A [Adult TPI. Third Report of the National Cholesterol Education Program (NCEP) Expert Panel on Detection, Evaluation, and Treatment of High Blood Cholesterol in Adults (Adult Treatment Panel III) final report. *Circulation*. 2002;106(25):3143-3421. <http://www.ncbi.nlm.nih.gov/pubmed/12485966>. Accessed January 9, 2017.
47. IDF T. IDF Consensus Worldwide Definition of the Metabolic Syndrome. http://www.idf.org/webdata/docs/IDF_Meta_def_final.pdf. 2006.
48. Després J-P, Lemieux I. Abdominal obesity and metabolic syndrome. *Nature*. 2006;444(7121):881-887. doi:10.1038/nature05488.
49. van der Meer RW, Lamb HJ, Smit JWA, de Roos A. MR Imaging Evaluation of Cardiovascular Risk in Metabolic Syndrome. *Radiology*. 2012;264(1):21-37. doi:10.1148/radiol.12110772.
50. Bizino MB, Hammer S, Lamb HJ. Metabolic imaging of the human heart: clinical application of magnetic resonance spectroscopy. *Heart*. 2014;100(11):881-890. doi:10.1136/heartjnl-2012-302546.
51. Schuppan D, Schattenberg JM. Non-alcoholic steatohepatitis: Pathogenesis and novel therapeutic approaches. *J Gastroenterol Hepatol*. 2013;28:68-76. doi:10.1111/jgh.12212.
52. de Vries APJ, Ruggerenti P, Ruan XZ, et al. Fatty kidney: emerging role of ectopic lipid in obesity-related renal disease. *Lancet Diabetes Endocrinol*. 2014;2(5):417-426. doi:10.1016/S2213-8587(14)70065-8.
53. Bobulescu IA, Lotan Y, Zhang J, et al. Triglycerides in the Human Kidney Cortex: Relationship with Body Size. *Norata GD, ed. PLoS One*. 2014;9(8):e101285. doi:10.1371/journal.pone.0101285.
54. D'Agati VD, Chagnac A, de Vries APJ, et al. Obesity-related glomerulopathy: clinical and pathologic characteristics and pathogenesis. *Nat Rev Nephrol*. 2016;12(8):453-471. doi:10.1038/nrneph.2016.75.
55. Guebre-Egziabher F, Alix PM, Koppe L, et al. Ectopic lipid accumulation: A potential cause for metabolic disturbances and a contributor to the alteration of kidney function. *Biochimie*. 2013;95(11):1971-1979. doi:10.1016/j.biochi.2013.07.017.
56. Li Z, Woollard JR, Wang S, et al. Increased glomerular filtration rate in early metabolic syndrome is associated with renal adiposity and microvascular proliferation. *Am J Physiol Renal Physiol*. 2011;301(5):F1078-87. doi:10.1152/ajprenal.00333.2011.
57. Rutledge JC, Ng KF, Aung HH, Wilson DW. Role of triglyceride-rich lipoproteins in diabetic nephropathy. *Nat Rev Nephrol*. 2010;6(6):361-370. doi:10.1038/nrneph.2010.59.
58. Wang XX, Jiang T, Shen Y, et al. The farnesoid X receptor modulates renal lipid metabolism and diet-induced renal inflammation, fibrosis, and proteinuria. *Am J Physiol Renal Physiol*. 2009;297(6):F1587-96. doi:10.1152/ajprenal.00404.2009.
59. Brink WM, van der Jagt AMA, Versluis MJ, Verbist BM, Webb AG. High permittivity dielectric pads improve high spatial resolution magnetic resonance imaging of the inner ear at 7 T. *Invest Radiol*. 2014;49(5):271-277. doi:10.1097/RLI.000000000000026.
60. Straubinger K, Schick F, Lutz O. Pulse Angle Dependence of Double-Spin-Echo Proton NMR Spectra of Citrate--Theory and Experiments. *J Magn Reson Ser B*. 1996;110:188-194. https://ac.els-cdn.com/S106418669600291/1-s2.0-S106418669600291-main.pdf?_tid=fc32b39c-c31f-11e7-ad30-00000aacb35d&acdnat=1509992961_1710296761d5b549ac51ecbb90245564. Accessed November 6, 2017.
61. Kreis R. Quantitative localized ¹H MR spectroscopy for clinical use. *J Prog Nucl Magn Reson Spectrosc*. 1997;31:155-195. https://ac.els-cdn.com/S0079656597000149/1-s2.0-S0079656597000149-main.pdf?_tid=0ce2de-c31c-11e7-ba6f-00000aacb35e&acdnat=1509991324_99dea03b2bc60aa03df3774d91c184fa. Accessed November 6, 2017.
62. Ryner LN, Ke Y, Thomas MA. Flip Angle Effects in STEAM and PRESS--Optimized versus Sinc RF Pulses. *J Magn Reson*. 1998;131:118-125. https://ac.els-cdn.com/S1090780797913331/1-s2.0-S1090780797913331-main.pdf?_tid=d813bf3a-c31d-11e7-a7f0-00000aab0f27&acdnat=1509992041_c5d5b005b902da08b5edeaf15216ab9. Accessed November 6, 2017.
63. Tal A, Gonen O. Spectroscopic localization by simultaneous acquisition of the double-spin and stimulated echoes. *Magn Reson Med*. 2015;73(1):31-43. doi:10.1002/mrm.25112.
64. Moonen CT, von Kienlin M, van Zijl PC, et al. Comparison of single-shot localization methods (STEAM and PRESS) for in vivo proton NMR spectroscopy. *NMR Biomed*. 1989;2(5-6):201-208. <http://www.ncbi.nlm.nih.gov/pubmed/2641894>. Accessed November 6, 2017.
65. Fuss TL, Cheng LL. Evaluation of Cancer Metabolomics Using ex vivo High Resolution Magic Angle Spinning (HRMAS) Magnetic Resonance Spectroscopy (MRS). *Metabolites*. 2016;6(1):11. doi:10.3390/metabo6010011.
66. Ulmer S, Backens M, Ahlhelm FJ. Basic Principles and Clinical Applications of Magnetic Resonance Spectroscopy in Neuroradiology. *J Comput Assist Tomogr*. 2016;40(1):1-13. doi:10.1097/RCT.0000000000000322.
67. in 't Zandt H, van Der Graaf M, Heerschap A. Common processing of in vivo MR spectra. *NMR Biomed*. 2001;14(4):224-232. <http://www.ncbi.nlm.nih.gov/pubmed/11410940>. Accessed August 24, 2017.
68. Drost DJ, Riddle WR, Clarke GD, AAPM MR Task Group #9. Proton magnetic resonance spectroscopy in the brain: report of AAPM MR Task Group #9. *Med Phys*. 2002;29(9):2177-2197. doi:10.1118/1.1501822.

PART ONE
TECHNICAL
DEVELOP-
MENTS
HIGH FIELD
BODY MR

**INCREASING SIGNAL
HOMOGENEITY AND
IMAGE QUALITY IN
ABDOMINAL IMAGING
AT 3 T WITH VERY
HIGH PERMITTIVITY
MATERIALS**

2 INCREASING SIGNAL HOMOGENEITY AND IMAGE QUALITY IN ABDOMINAL IMAGING AT 3 T WITH VERY HIGH PERMITTIVITY MATERIALS

Adapted from *Magnetic Resonance in Medicine* 2012 Oct;68(4):1317-2.

Authors

P. de Heer,^{1,2} W. M. Brink,² B. J. Kooij,¹ and A. G. Webb^{2*}

¹ Department of Telecommunications, Technical University of Delft, Delft, The Netherlands.

² C.J. Gorter Center for High Field MRI, Department of Radiology, Leiden University Medical Center, Leiden, The Netherlands.

ABSTRACT

The appearance of severe signal drop-outs in abdominal imaging at 3 T arises primarily from areas of very low B_1^+ transmit field in the body, and is problematic in both obese as well as very thin subjects. In this study, we show how thin patient-friendly pads containing new high permittivity materials can be designed and optimized, and when placed around the subject increase substantially the B_1^+ uniformity and the image quality. Results from nine healthy volunteers show that inclusion of these dielectric pads results in statistically significant decreases in the coefficient of variance of the B_1^+ field, with stronger and more uniform fields being produced. In addition there are statistically significant decreases in time-averaged power required for scanning. These differences are present in both quadrature-mode operation (coefficient of variance decrease, $P < 0.0001$, mean $25.4 \pm 10\%$: power decrease, $P = 0.005$, mean $14 \pm 14\%$) and also for the RF shimmed case (coefficient of variance decrease, $P = 0.01$, mean $16 \pm 13\%$: power decrease, $P = 0.005$, mean $22 \pm 11\%$) of a dual-transmit system.

INTRODUCTION

The appearance of signal voids in abdominal MRI in both volunteers and patients at 3 T has been noted by many researchers.¹⁻⁶ Some report that severely obese patients present the worst situation,² others that this effect also occurs for very thin patients.^{1,3} As noted by Bernstein¹ "Image shading and uneven contrast resulting from spatial variation in the transmit B_1^+ field remains one of the biggest unsolved problems for routine clinical 3 T imaging today." The phenomenon of signal loss is often referred to as "dielectric resonance." Pregnant women and patients with ascites are universally problematic, and subsequently are almost always studied at 1.5 T.^{5,6} The clinical, and implicitly financial, importance of this situation is emphasized by the recent commercial introduction of dual-transmit RF systems at 3 T, in which the quadrature body coil is effectively split into two linear coils, each of which can be driven with an independently controlled magnitude and phase. The two degrees of freedom (relative amplitudes and relative phases of the two channels) compared to only one (absolute amplitude) for a conventional single transmit system can produce considerable increases in RF transmit homogeneity,^{7,8} as has long been known theoretically and investigated extensively for imaging at 7 T.⁹⁻¹¹ However, experience at our institution and elsewhere indicates that, despite improved performance, dual-channel 3 T systems do not consistently solve the problem of image inhomogeneities. Experimental and simulation work has suggested that there are still further improvements using an eight channel transmit body coil,^{12,13} but such a setup is not currently commercially available.

A second approach to address the issues of RF inhomogeneity in 3 T abdominal imaging is the use of "dielectric pads".¹⁴⁻¹⁷ Previous very simple pads typically are made from ultrasound gel with dissolved paramagnetics such as manganese chloride to give a short T^2 and hence low background MR signal. Some institutions report that these are used locally for most abdominal scans,¹⁵ whereas others report that they are not commonly used in the wider community.¹ There are several problems with this approach as currently implemented. From a practical point-of-view the pad is 3 cm thick and therefore somewhat patient-unfriendly. In the usual implementation, a single pad is placed centrally on top of the patient irrespective of the patient size: the large thickness makes it impractical to place a second one underneath the patient to improve the transmit field in the posterior regions. Perhaps most importantly, no optimization of the properties (size, shape, thickness, placement, or relative permittivity) of the dielectric pad or material has been shown.

In this article, we present both electromagnetic (EM) simulations and experimental data using thin pads with high permittivity materials based upon aqueous suspensions of metal titanates which have a relative permittivity of 300.^{18,19} Placement of two of these thin (1 cm) pads anterior and posterior to the subject is shown to improve significantly both the transmit field homogeneity and the overall image quality. The imaging performance both with and without dielectric pads is compared experimentally to that of a dual-channel RF system in quadrature mode, as well as the combined approach using both the dielectric pads and RF shimming. Significant improvements in homogeneity due to the pads are found when the scanner is used in the conventional quadrature mode, and the best performance is found using RF shimming combined with the high permittivity pads.

METHODS

EM Simulations

A commercial package based on a finite difference time domain method (xFDTD, Remcom, PA) was used for all simulations. The RF coil was modeled as a 16 rung high pass birdcage coil with a diameter of 61 cm, length 56 cm, driven in quadrature mode by 32 ideal current sources with an impedance of 50 Ω . This corresponds to a dual transmit system being operated in the conventional quadrature or fixed phase mode, in which the phase relationship between the two channels is fixed at 90°. One male (Duke, body mass index 23) or one female (Ella, body mass index 22) model from the virtual family was placed in the center of the coil.²⁰ An isotropic grid cell size of 2.5 mm was used with a seven-layer perfectly matched absorbing boundary. A sinusoidal current was applied at 128 MHz, with a timestep of 4.8 ps. A criterion of -50 dB was set for convergence of the steady-state fields, and typical simulation times were 30 min using a graphics processing unit. The transmit magnetic field (B_1^+), electric (E) field, and specific absorption rate (SAR) were simulated for each configuration: normalization was to 1 W dissipated power.

To determine the optimal pad permittivity, a grid search was used in which the relative permittivity values of two pads (one anterior, one posterior), each of thickness 1 cm, were varied from 1 to 650 in steps of 50. For comparison, a 3 cm thick commercially available water pad was included in the simulations.^{14,15} The coefficient of variation (C_v) of the B_1^+ field, i.e., 100 multiplied by the standard deviation of the B_1^+ divided by its mean value, across the simulated B_1^+ map (transverse orientation) was evaluated in MATLAB (Mathworks, Natick, MA). In the transverse slices, the value of C_v is calculated throughout the entire cross-section (not considering the arms). For coronal slices, a rectangular region of interest is assigned through the thorax and abdominal region of the body.

Production of High Permittivity Pads

High permittivity pads were produced based on the approach described previously.¹⁹ Briefly, barium titanate ($BaTiO_3$) powder (Alfa Aesar GmbH) was mixed with water until a saturated suspension was reached since the aim was to produce as high a permittivity as possible. Approximately, a 4:1 weight/weight ratio of barium titanate powder to water was used. The dielectric constant was measured using a dielectric probe kit (85070E, Agilent Technologies, Santa Clara, CA) and a network analyzer, and had a value of 300. This is substantially higher than reported in a previous publication,¹⁹ and emphasizes the fact that the permittivity that can be reached is critically dependent upon the surface properties and size of the barium titanate powder used. Two pads, each 1 cm thick, of the suspension were heat-sealed within polypropylene pads, with dimensions 28 x 22 cm² (left/right and head/foot dimensions, respectively). The weight of these pads was approximately 2 kg, significantly less both in thickness and weight compared to a commercial water-based pad (3 cm thick and 3.2 kg weight).

MRI Protocols

All experiments were approved by the Leiden University Medical Center Committee for Medical Ethics, and performed on a dual-transmit 3 T Philips Achieva. Nine volunteers (seven male, two female), with ages between 25 and 50, and body mass indices (BMIs) between 18 and 38, were imaged. The transmit coil was the inbuilt body resonator, and a six-element "cardiac array" was used for signal reception: this consisted of three elements anterior and three elements posterior to the patient. All experiments were

performed first with the pads in place, the pads were then removed with as little subject motion as possible, and rescanning without the pads was performed. Figure 1 shows a schematic of the EM simulation setup accompanied by a photograph of the positioning of the thin pad on the anterior side of the volunteer. The transmit field of the body coil was mapped using the method of Yarnykh at 2.5 mm isotropic resolution with a target angle of 45° to avoid ambiguity for any actual tip angle close to or greater than 90°. Imaging parameters: three-dimensional gradient echo sequence: echo time = 20 ms, TR1 = 100 ms, TR2 = 250 ms, nominal flip angle 50°, 64 x 64 data matrix, transverse slice thickness 10 mm, 1 mm slice gap, field-of-view ~ 250 x 450 x 120 mm³ with slight variations dependent upon subject size. Tip angle maps were generated from the ratio of the signal intensities obtained with the two different pulse repetition time values. Tip angle maps were then converted to transmit sensitivity (B_1^+ per square root of power) for direct comparison with EM simulations. Coefficient of variation values were calculated as described in the previous section. For assessment of image quality, T1-weighted turbo gradient echo sequences were run with the following parameters: echo time = 2.3 ms, pulse repetition time = 10 ms, tip angle = 15°, 252 x 149 data matrix, slice thickness = 7 mm, 1 mm slice gap, field-of-view = 297 x 375 x 77 mm³, acquisition time = 13.5 s for six slices, linear phase encoding, scan percentage 75%, turbo echo factor 149, no flow compensation. Images were acquired during breathhold (exhalation).

Four different settings were used to investigate the separate effects of RF shimming and the dielectric pads. First, RF shimming was turned off forcing the conventional quadrature relationship between the two separate transmit channels. Second, RF shimming was enabled, in which a rapid grid search is performed by the Philips system with a free range of relative amplitudes and phase difference between the two channels. RF shimming was performed separately for the cases with and without the dielectric pads in place. Measurements of the time-averaged power during the imaging sequence are recorded in the log file of the scanner. These measurements are performed directly at the amplifier, and measure both the forward and reflected powers, the difference between the two being the power delivered to the system (losses in cables and connectors between the RF amplifiers and the RF coil may be up to 15%, but this percentage does not vary significantly with absolute power).



FIGURE 1. (left) Schematic of the setup for the EM simulations with a dielectric pad (red) with thickness 1 cm placed on the abdomen. An identically shaped pad (green) is placed on the back, in the same position. (right) photo-

graph of a volunteer with the pads in place. [Color figure can be viewed in the online issue, which is available at wileyonlinelibrary.com.]

Statistical Analysis

Statistical analysis was performed using Graphpad Prism (La Jolla, CA). Paired two-sided Student's t-tests were performed for conditions of with/without dielectric pads for data acquired with and without the dielectric pads.

RESULTS

EM Simulations

Figure 2 shows simulation results of the B_1^+ field in the male Duke model. The grid search gave an optimum configuration with relative permittivities of 400 for the anterior pad and 500 for the posterior pad for a pad thickness of 1 cm. In practice, the highest permittivity that could be achieved was 300 using essentially a saturated suspension of barium titanate powder in water.

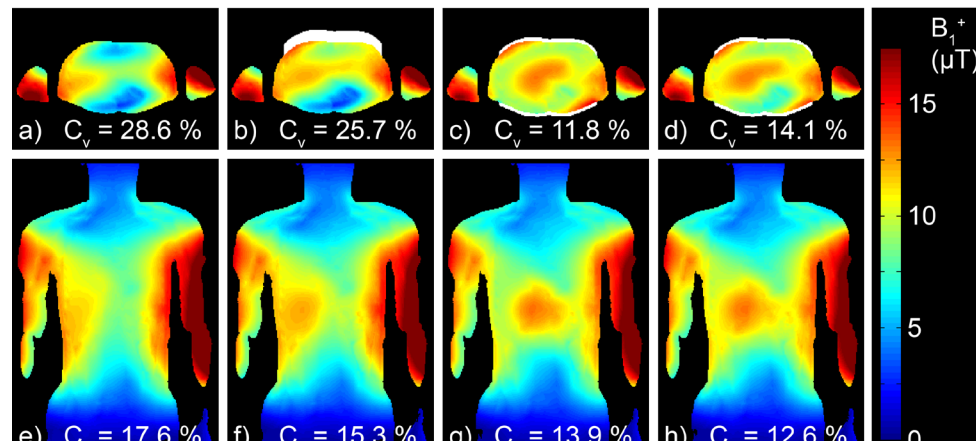


FIGURE 2. EM simulations of the B_1^+ field in the "Duke" model. (a)–(d) transverse slice through the centre of the liver, (e)–(h) corresponding coronal slices. (a) and (e) no dielectric pads, (b) and (f) a 3 cm thick "commercial" water-based pad, (c) and (g) the optimum solution for two 1

cm thick pads with $\epsilon_r = 400$ for the anterior pad and $\epsilon_r = 500$ for the posterior pad, (d) and (h) the practically realizable situation with two 1 cm pads each with $\epsilon_r = 300$. The coefficient of variation is shown for each configuration.

In Figure 2, the values of C_v are given for the situations of no pads, the commercial pad (3 cm thick, water-based, $\epsilon_r = 80$), the optimum configuration of the two pads placed anterior and posterior, and the practical configuration of two pads with relative permittivities of 300. As outlined in the methods section, in the transverse slice, the value of C_v is calculated throughout the entire cross-section (not considering the arms), and for the coronal slice through the thorax and abdominal region of the body. There are considerable improvements in the B_1^+ homogeneity for the anterior/posterior high permittivity pads compared to both the situation with no pads, and also the asymmetric placement of the commercial pad on only the anterior side of the subject. It should be noted that, since optimization was performed on the transverse slice due to the much more defined region-of-interest (essentially the entire slice without the arms), the value of C_v in the coronal plane can actually be slightly lower for the $\epsilon_r = 300$ case than the "optimum" permittivity value.

Figure 3 shows corresponding plots for the female Ella model. In this case, the optimum configuration was found to correspond to relative permittivities of 300 for the front and back. The dependence of the value of C_v on the permittivities of the two pads for both the Duke and Ella model is shown in Figure 4. As can be seen, there is a relatively smooth minimum for values around 300 – 500, but the increase is quite severe for values below about 300 or above 500. These results confirm the simulation results in Figure 2 which demonstrate that there is a very small increase in C_v when operating with pads with permittivity of 300 compared to the optimum values of 400/500.

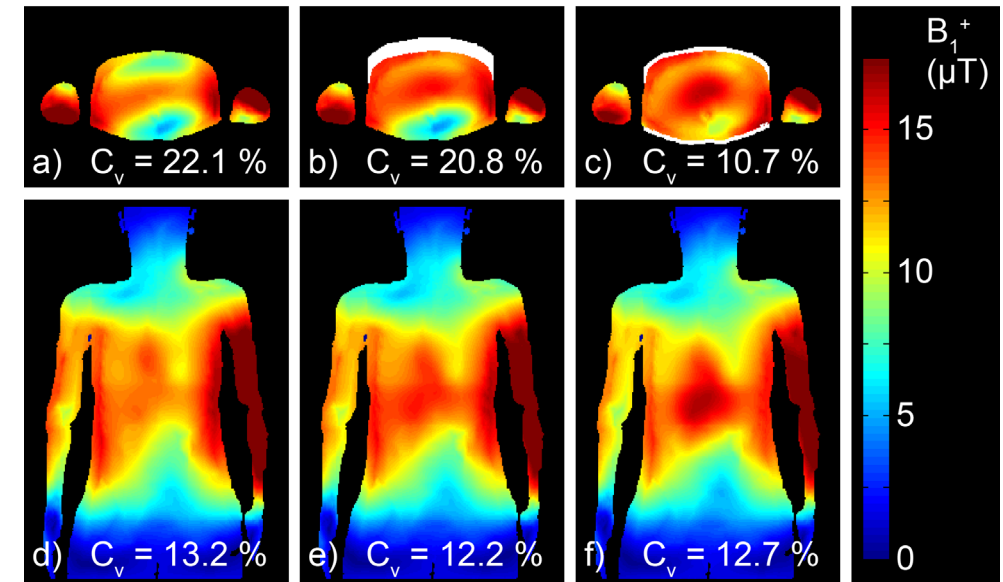


FIGURE 3. EM simulations of the B_1^+ field in the "Ella" model. (a)–(c) transverse slice through the centre of the liver, (d)–(f) corresponding coronal slices. (a) and (d) no dielectric pads, (b) and (e) a 3 cm thick "commercial"

water-based pad, (c) and (f) the optimum solution for two 1 cm thick pads each with $\epsilon_r = 300$. The coefficient of variation is shown for each configuration.

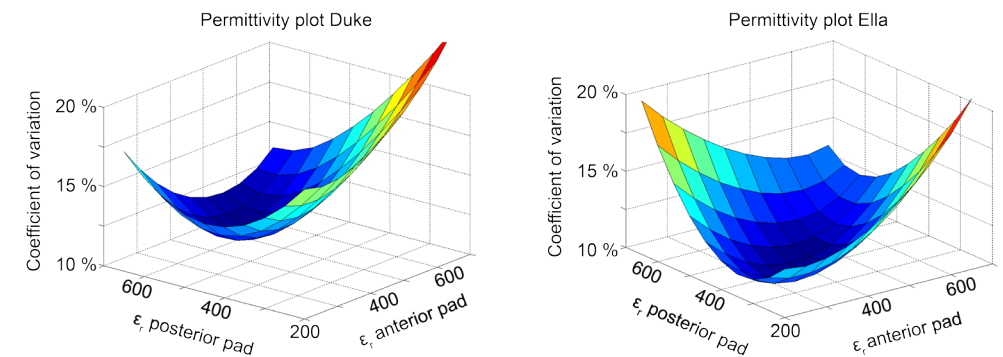


FIGURE 4. Plots of the coefficient of variation (vertical axis) versus the permittivities of both the anterior and posterior pads. (left) Duke and (right) Ella models.

[Color figure can be viewed in the online issue, which is available at wileyonlinelibrary.com.]

To determine whether the high permittivity pads increase either the local or global SAR values, Figure 5 shows transverse and coronal plots of the local (1 g tissue average) SAR values for the Duke model generated by the quadrature-driven body coil. The highest values are generally found in the arms (since they are in the region of the highest electric field of the RF coil), and all values in the body are at least a factor-of-two lower. There are negligible differences introduced by either the commercial or new high permittivity pads. Very similar results were found for Ella (data not shown). These results correspond to the conventional quadrature-driven body coil, but it is anticipated that similar effects occur in the RF-shimmed case.

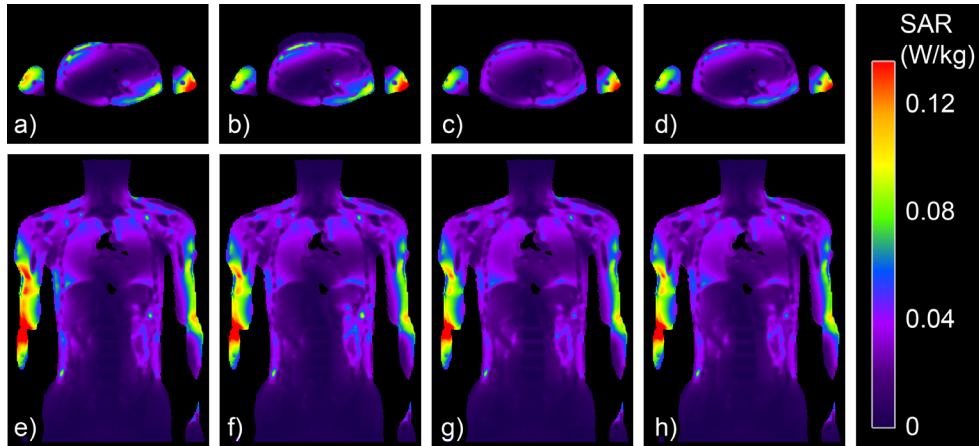


FIGURE 5. EM simulations of the 1-g averaged SAR in the "Duke" model. a–d: transverse slice through the centre of the liver, (e)–(h) corresponding coronal slices. (a) and (e) no dielectric pads, (b) and (f) a 3 cm thick "commercial" water-based pad, (c) and (g) the optimum solution for two 1 cm thick pads with $\epsilon_r = 400$ for the anterior pad and $\epsilon_r = 500$ for the posterior pad, (d) and (h) the practically realizable situation with two 1 cm pads each with $\epsilon_r = 300$. [Color figure can be viewed in the online issue, which is available at wileyonlinelibrary.com.]

Experimental Results

Figure 6 shows transverse slices acquired for five of the nine volunteers (for clarity) for all four configurations of with/without RF shimming and with/without high permittivity pads. Clear improvements in image homogeneity are evident with the addition of the pads.

Figure 7 demonstrated the B_1^+ maps acquired without and with the dielectric pads in place for the same volunteers and the same conditions as shown in Figure 6. There is good agreement with the simulated results presented in Figure 2.

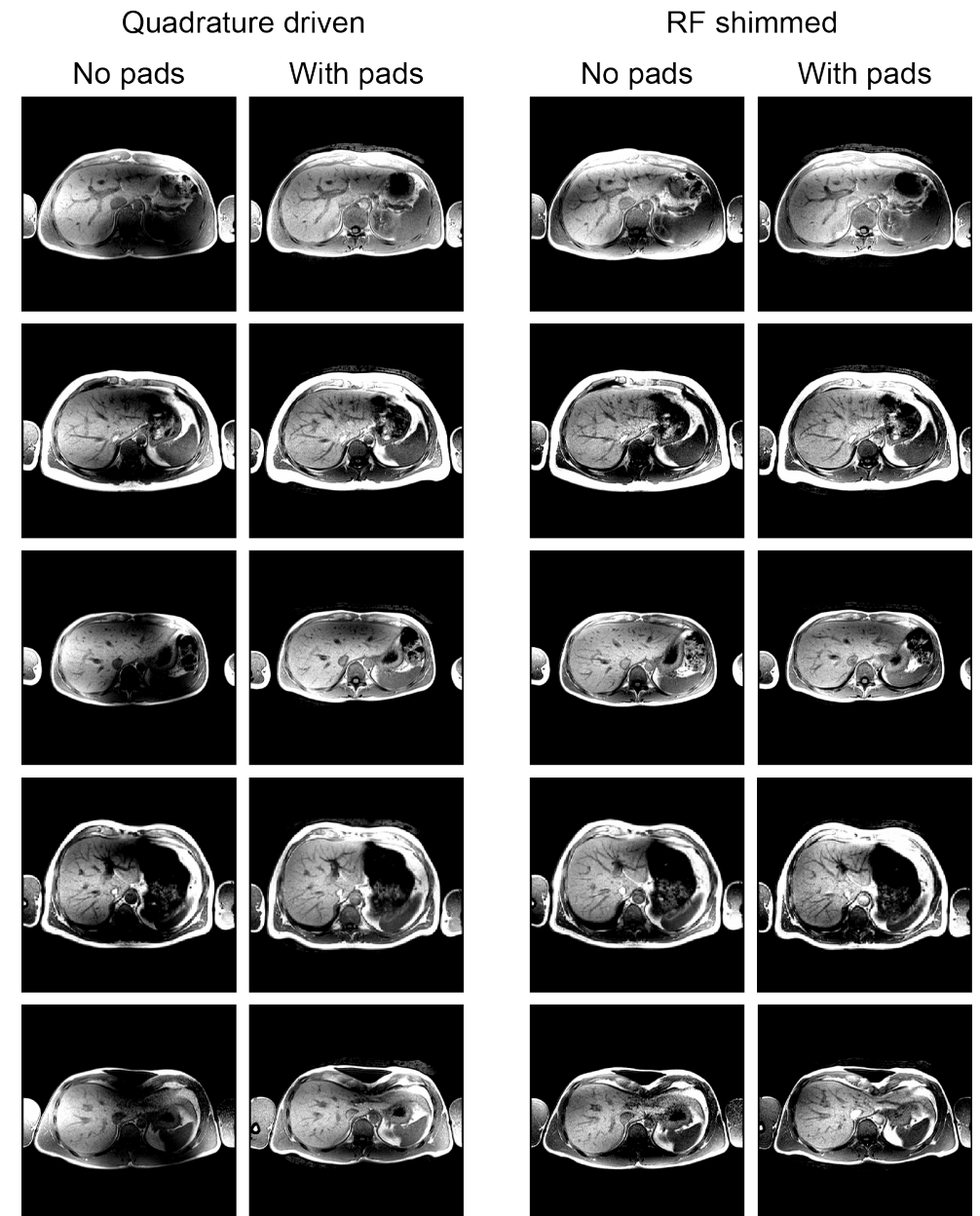


FIGURE 6. Comparison of T₁-weighted turbo-spin echo images acquired from five volunteers with BMI values between 18 and 24 for four different configurations of

quadrature/RF-shimmed drive and without/with dielectric pads.

Figure 8 shows a plot of the C_v for all nine volunteers for the four different imaging conditions. For the quadrature drive, the C_v decreased in all cases, and often by a substantial amount (mean $25.4 \pm 10\%$), with the addition of the dielectric pads. In the RF shimmed case, a decrease (mean $16 \pm 13\%$) in C_v for all but one case was achieved using the pads. Statistical analysis showed a significant decrease ($P < 0.0001$) in C_v between quadrature mode without and with the dielectric pads, and also in the RF shimmed case without and with the pads ($P = 0.005$).

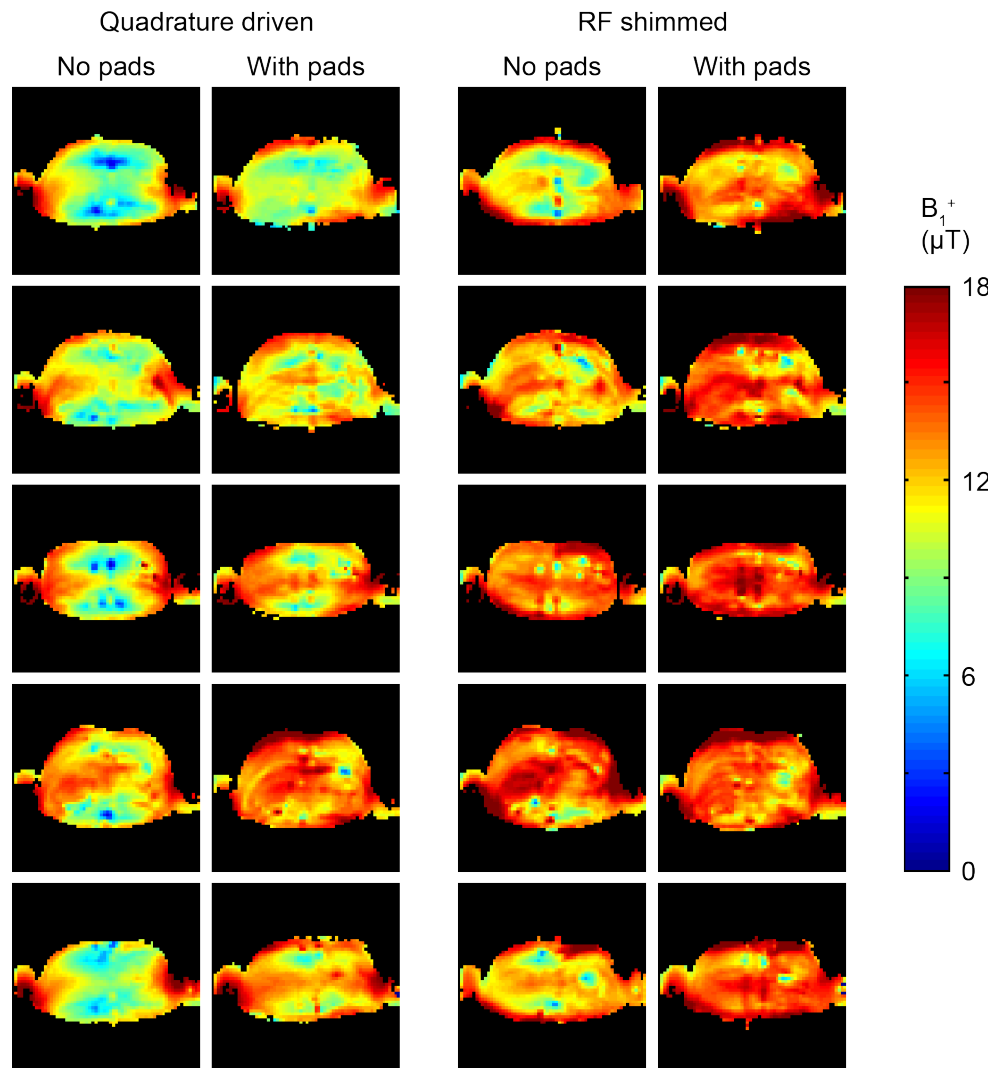


FIGURE 7. Measured B_1^+ maps from the same volunteers as in Fig. 6 for the same four configurations. [Color figure can be viewed in the online issue, which is available at wileyonlinelibrary.com.]

In terms of the RF power required for image acquisition, there were also statistically significant reductions in both the peak power and time-averaged power using the dielectric pads. As with most power optimization algorithms on commercial systems, the average flip angle across the central transverse slice is calibrated. In the case of an inhomogeneous B_1^+ distribution, this causes overtipping in areas of high transmit efficiency, and undertipping in areas of low efficiency. Figure 9 shows the time-averaged power needed for the T1-weighted turbo gradient echo sequence used to produce the images in Figure 6: these powers were read from the log file that was stored on the scanner, with the powers being measured at the output of the RF amplifier as described in the methods section. The power demands were in all but one case lower with pads than without pads. Statistical analysis showed a significant decrease in average power when the high permittivity pads were in place for both the quadrature-driven mode ($P = 0.01$) and RF shimmed mode ($P = 0.0004$).

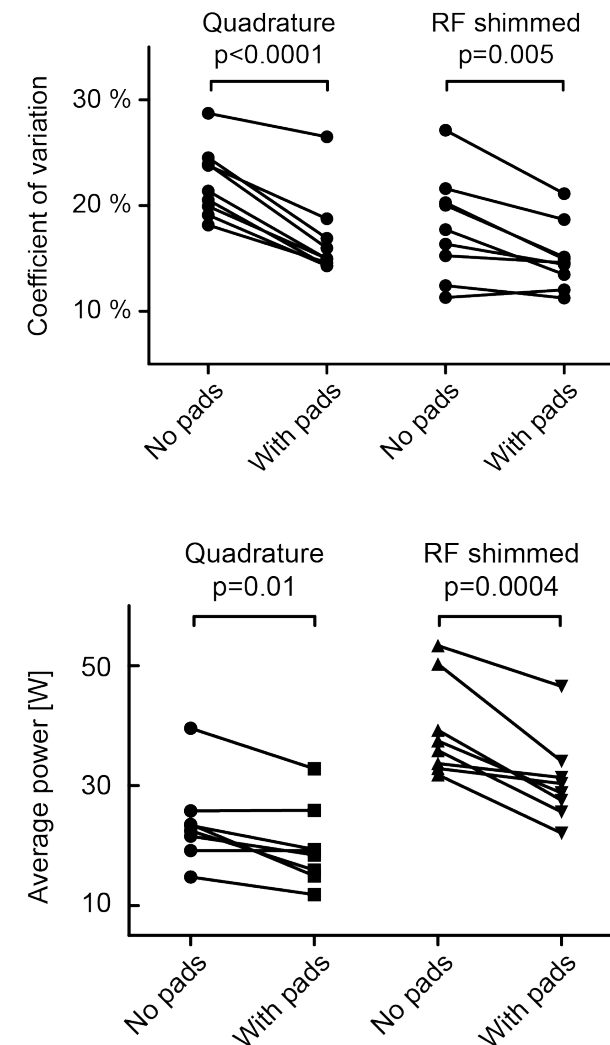


FIGURE 8. Plot of coefficient of variation for all nine volunteers. Statistically significant decreases are shown for both quadrature driven and RF-shimmed cases when introducing the dielectric pads.

FIGURE 9. Plot of time averaged power measured for the images acquired in Fig. 6 for all nine volunteers. Statistically significant decreases are shown for both quadrature-driven and RF-shimmed cases when introducing the dielectric pads.

DISCUSSION AND CONCLUSION

The intrinsic inhomogeneity introduced by imaging an elliptical object with a quadrature RF coil is well known,²² and different patient geometries may mitigate or exacerbate this effect. The recent commercial introduction of dual-transmit systems has shown substantial improvement in image quality, but does not yet represent a complete solution to the problem. The “ability” of high permittivity materials²³ to increase the homogeneity of the transmit magnetic field has been shown primarily for neuroimaging at high field either with water bags²⁴ or materials formed from metal titanates.^{18,19,25} Recently, improvements for neuroimaging at 3 T have also been reported using large water pads.²⁶ The lower the magnetic field, the higher the permittivity must be to compensate for B_1 inhomogeneities since displacement currents are proportional to the operating frequency. In neuroimaging at 7 T, the optimum value of the permittivity was found to be 100.²⁰ In this current work, we have demonstrated that statistically significant improvements in transmit efficiency for abdominal imaging at 3 T can be achieved using thin, high permittivity pads placed anterior and posterior to the subject. There are large measured improvements when operating the system in quadrature mode, which corresponds to the vast majority of single channel 3 T systems currently available in the world. Even when operating in dual transmit mode with RF shimming on a state-of-the-art multichannel system, the dielectric pads provided a statistically significant increases in image homogeneity, as well as a reduction in the total power absorbed by the body.

The geometry which we studied is relatively simple, consisting only of two pads of 1 cm thickness, and certainly it can be anticipated that further improvements may result from optimized geometries including more pads in a more complex geometry. Another refinement would be to optimize the coefficient of variance over the entire three-dimensional imaging volume, rather than just a central slice as in this work. Higher permittivity materials should bring further increases in image quality, as well as reduction in the thickness of the required pads, particularly in the case of patients with higher body mass index values than in healthy volunteers studied here. The current study does not have enough volunteers, or volunteers with sufficient range of BMI values, to be able to relate directly the improvements afforded by the dielectric pads to the BMI, or probably even more relevant to the geometry of the body. Future clinical studies including patients with much higher BMI will be required to establish such a relationship. In this work no increases in global SAR (assuming body loss dominance) were evident, and indeed a reduction in local SAR was simulated for the quadrature-driven body coil. This was experimentally demonstrated by measuring substantial reductions in average power levels on the MR system both for the quadrature-driven mode, and also the RF shimmed mode.

ACKNOWLEDGMENTS

The authors are grateful to Sukhoon Oh and Chris Collins at the Hershey Medical Center for providing the body coil model, and to Wouter Teeuwisse for helping in data acquisition.

REFERENCES

- Bernstein MA, Huston J, III, Ward HA. Imaging artifacts at 3.0T. *J Magn Reson Imaging* 2006;24:735–746.
- Cornfeld D, Weinreb J. Simple changes to 1.5-T MRI abdomen and pelvis protocols to optimize results at 3 T. *Am J Roentgenol* 2008; 190:W140–W150.
- Chang KJ, Kamel IR. Abdominal imaging at 3T: challenges and solutions. *Appl Radiol* 2010;39:22–31.
- Dietrich O, Reiser MF, Schoenberg SO. Artifacts in 3-T MRI: Physical background and reduction strategies. *Eur J Radiol* 2008;65:29–35.
- Yang RK, Roth CG, Ward RJ, deJesus JO, Mitchell DG. Optimizing abdominal MR imaging: approaches to common problems. *Radiographics* 2010;30:185–199.
- Merkle EM, Dale BM. Abdominal MRI at 3.0 T: the basics revisited. *Am J Roentgenol* 2006;186:1524–1532.
- Nelles M, Konig RS, Gieseke J, Guerland-van Battum MM, Kukuk GM, Schild HH, Willinek WA. Dual-source parallel RF transmission for clinical MR imaging of the spine at 3.0 T: intraindividual comparison with conventional single-source transmission. *Radiology* 2010; 257:743–753.
- Willinek WA, Gieseke J, Kukuk GM, Nelles M, Konig R, Morakkabati-Spitz N, Traber F, Thomas D, Kuhl CK, Schild HH. Dual-source parallel radiofrequency excitation body MR imaging compared with standard MR imaging at 3.0 T: initial clinical experience. *Radiology* 2010;256:966–975.
- Adriany G, van de Moortele PF, Wiesinger F, et al. Transmit and receive transmission line arrays for 7 Tesla parallel imaging. *Magn Reson Med* 2005;53:434–445.
- Vaughan JT, Snyder CJ, DelaBarre LJ, Botan PJ, Tian J, Bolinger L, Adriany G, Andersen P, Strupp J, Ugurbil K. Whole-body imaging at 7T: preliminary results. *Magn Reson Med* 2009;61:244–248.
- Kraff O, Bitz AK, Kruszona S, Orzada S, Schaefer LC, Theysohn JM, Maderwald S, Ladd ME, Quick HH. An eight-channel phased array RF coil for spine MR imaging at 7 T. *Invest Radiol* 2009;44:734–740.
- van den Berg CA, van den Bergen B, Van de Kamer JB, Raaymakers BW, Kroeze H, Bartels LW, Lagendijk JJ. Simultaneous B_1 homogenization and specific absorption rate hotspot suppression using a magnetic resonance phased array transmit coil. *Magn Reson Med* 2007;57:577–586.
- Vernickel P, Roschmann P, Findeklee C, Ludeke KM, Leussler C, Overweg J, Katscher U, Grasslin I, Schunemann K. Eight-channel transmit/receive body MRI coil at 3T. *Magn Reson Med* 2007;58:381–389.
- Franklin KM, Dale BM, Merkle EM. Improvement in B_1 -inhomogeneity artifacts in the abdomen at 3T MR imaging using a radiofrequency cushion. *J Magn Reson Imaging* 2008;27:1443–1447.
- Sreenivas A, Lowry M, Gibbs P, Pickles M, Turnbull LW. A simple solution for reducing artefacts due to conductive and dielectric effects in clinical magnetic resonance imaging at 3 T. *Eur J Radiol* 2007;62:143–146.
- Takayama Y, Nonaka H, Nakajima M, Obata T, Ikehira H. Reduction of a high-field dielectric artifact with homemade gel. *Magn Reson Med Sci* 2008;7:37–41.
- Kataoka M, Isoda H, Maetani Y, et al. MR imaging of the female pelvis at 3 Tesla: evaluation of image homogeneity using different dielectric pads. *J Magn Reson Imaging* 2007;26:1572–1577.
- Teeuwisse WM, Brink WM, Webb AG. Quantitative assessment of the effects of high-permittivity pads in 7 Tesla MRI of the brain. *Magn Reson Med* 2012;67:1285–1293.
- Teeuwisse WM, Brink WM, Haines K, Webb AG. Simulations of high permittivity materials for 7 T neuroimaging and evaluation of a new barium titanate-based dielectric. *Magn Reson Med* 2012;67: 912–918.
- Christ A, Kainz W, Hahn EG, et al. The Virtual Family-development of surface-based anatomical models of two adults and two children for dosimetric simulations. *Phys Med Biol* 2010;55:N23–N38.
- Yarnykh VL. Actual flip-angle imaging in the pulsed steady state: A method for rapid three-dimensional mapping of the transmitted radiofrequency field. *Magn Reson Med* 2007;57:192–200.
- Sled JG, Pike GB. Standing-wave and RF penetration artifacts caused by elliptical geometry: an electrodynamic analysis of MRI. *IEEE Trans Med Imaging* 1998;17:653–662.
- Webb AG. Dielectric materials in magnetic resonance. *Concepts Magn Reson* 2011;38A:48–84.
- Yang QX, Mao W, Wang J, Smith MB, Lei H, Zhang X, Ugurbil K, Chen W. Manipulation of image intensity distribution at 7.0 T: passive RF shimming and focusing with dielectric materials. *J Magn Reson Imaging* 2006;24:197–202.
- Snaar JE, Teeuwisse WM, Versluis MJ, van Buchem MA, Kan HE, Smith NB, Webb AG. Improvements in high-field localized MRS of the medial temporal lobe in humans using new deformable highdielectric materials. *NMR Biomed* 2011;24:873–879.
- Yang QX, Wang JL, Wang JH, Collins CM, Wang CS, Smith MB. Reducing SAR and Enhancing Cerebral Signal-to-Noise Ratio with High Permittivity Padding at 3 T. *Magn Reson Med* 2011;65:358–362.



IMPROVED CARDIAC
PROTON MAGNETIC
RESONANCE
SPECTROSCOPY
AT 3 T USING HIGH
PERMITTIVITY PADS

3 IMPROVED CARDIAC PROTON MAGNETIC RESONANCE SPECTROSCOPY AT 3 T USING HIGH PERMITTIVITY PADS

Adapted from *Investigative Radiology*. 2016 Feb;51(2):134-8.

Authors

Paul de Heer, MSc,¹ Maurice B. Bizino, MD,² Maarten J. Versluis, PhD,¹ Andrew G. Webb, PhD,¹ and Hildo J. Lamb, MD, PhD²

¹ C.J. Gorter Center for High Field MRI, Department of Radiology, Leiden University Medical Center, Leiden, the Netherlands.

² Department of Radiology, Leiden University Medical Center, Leiden, the Netherlands.

ABSTRACT

Objective:

The aim of this study was to determine whether high permittivity (HP) pads can be used to increase the signal-to-noise ratio (SNR) of cardiac proton magnetic resonance spectroscopy at 3 T, allowing faster data acquisition.

Materials and Methods:

The institutional review board approved the study protocol, and written informed consent was obtained from all participants. In 22 healthy volunteers, water-suppressed localized spectra were acquired in the interventricular septum without and with HP pads. The SNR and myocardial triglyceride content (MTGC) were measured without and with the HP pads, and the results were compared with a paired sample Student t test.

Results:

Application of HP pads increased mean (SD) SNR from 27.9 (15.6) to 42.3 (24.4) ($P < 0.0001$), a mean gain of 60%. The acquisition time can thereby be reduced from just under 5 minutes to just under 2 minutes while maintaining the same SNR. The mean (SD) MTGC was 0.39% (0.17%) without pads and 0.38% (0.15%) with pads ($P = 0.83$) for the healthy volunteers, showing that no bias is introduced by using the pads. No difference in spectral linewidth was measured ($P = 0.80$), the values being 17.4 (4.9) Hz without and 17.1 (3.2) Hz with pads. Both transmit and receive maps showed increases in sensitivity due to the presence of the HP pads.

Conclusions:

High permittivity pads improve cardiac proton magnetic resonance spectroscopy at 3 T by increasing the SNR on average by 60%, which can be used to reduce data acquisition time significantly, allowing fast assessment of MTGC without compromising spectral quality. The SNR increase arises primarily from the increase in receive sensitivity of the phased array, which is more closely coupled to the body via the HP pads. In addition, the transmit efficiency is also increased, allowing shorter or lower power radiofrequency pulses.

INTRODUCTION

Myocardial triglyceride content (MTGC) reflects the process of ectopic intracellular fat accumulation, which is linked to the development of heart failure.¹ This process is called steatosis and has proved to be an important parameter in the field of cardiovascular disease related to obesity, metabolic syndrome, and type 2 diabetes mellitus.²⁻⁸ Myocardial steatosis can be reversed using therapeutic procedures, a fact which emphasizes the importance of a reliable measurement technique to monitor the cardiac MTGC. The criterion standard for the quantification of cardiac MTGC is proton magnetic resonance spectroscopy (¹H-MRS). However, cardiac ¹H-MRS is challenging due to an intrinsic low signal-to-noise ratio (SNR) as well as static and dynamic fluctuations in both the main magnetic field (B_0) as well as in the transmit field (B_1^+). To increase the SNR, many signal averages must be coadded, often between 32 and 128 averages at a field strength of 1.5 T. This will result in long acquisition times, more than 10 minutes, limiting the use of cardiac ¹H-MRS in a practical clinical protocol in which many other types of scan must also be acquired. Another method to increase SNR is to acquire data at a higher field strength.⁹ However, cardiac ¹H-MRS at 3 T is even more challenging than at 1.5 T due to increases in the degree of static and dynamic B_0 and B_1^+ inhomogeneities. Dynamic B_0 fluctuations, caused mainly by respiratory motion, result in phase and frequency variations between consecutive signal averages, thereby decreasing signal intensity and increasing linewidths (as well as changing line shape from Gaussian to Voigt) and complicating MTGC quantification. Dynamic B_1^+ inhomogeneities, caused also by respiratory motion, result in fluctuations in signal intensity per signal average.

Recent work has shown that it is possible to increase the quality of 3 T cardiac imaging, simultaneously increasing B_1^+ homogeneity over the volume of interest (VOI) and decreasing the required power, using high permittivity (HP) pads.¹⁰ Therefore, the purpose of this study was to determine whether the application of HP pads can increase the SNR in cardiac ¹H-MRS at 3 T, allowing shorter data acquisition times.

MATERIALS AND METHODS

Participants

The institutional review board approved the study protocol, and written informed consent was obtained from all participants. The study was conducted according to the principles expressed in the Declaration of Helsinki. Twenty-two healthy volunteers underwent cardiac ¹H-MRS from December 2013 until February 2014. Because of a voxel placement error (contamination with pericardial lipid), 2 volunteers were excluded from further analysis. The remaining 20 volunteers consisted of 12 female and 8 male subjects with a mean (SD) age of 29 (11) years (range, 19–53 years) and with a mean (SD) body mass index of 23 (3) kg/m² (range, 19.7–34.1 kg/m²).

Data Acquisition

Experiments were performed on a 3 T Ingenia whole-body magnetic resonance imaging scanner (Philips Healthcare, Best, the Netherlands) with dual-channel transmit capability. The body coil was used for transmission and an anterior (16 elements) and posterior (12 elements) array for reception. The entire scan protocol was performed twice: once without the HP pads and once with the HP pads placed between the patient and the receive array on the anterior and posterior sides of the thorax. To reduce any potential confounding factors, such as the duration that the volunteer had to lie in the magnet, data

were acquired with a random choice of which configuration was used first. Proper placement of the pads was confirmed by a 30-second survey scan. A series of scout scans was performed to localize the MRS voxel, 15 mL ($40 \times 15 \times 25 \text{ mm}^3$), within the myocardial interventricular septum (Figure 1A). Point resolved spectroscopy spectra were acquired with an echo time of 35 milliseconds without water suppression (repetition time: 9 seconds, 16 averages) and with selective excitation water suppression (repetition time: 3.5 seconds, 12–48 averages).¹¹ The unsuppressed spectrum was used as a reference for triglyceride quantification. Before each scan radiofrequency (RF) pulse power optimization, pencil beam B_0 shimming and resonance frequency determination were performed using 5 breath-holds (exhalation). All spectral acquisitions were respiratory navigator gated.¹² With a mean (SD) navigator efficiency of 57% (10%), this resulted in a mean acquisition time of 4 minutes and 55 seconds for the water-suppressed spectra (48 averages). The preparation time was on average 1 minute and 56 seconds, and the acquisition of the reference signal was 4 minutes and 15 seconds, resulting in a mean total scan time of 11 minutes and 6 seconds. Individual signal averages were saved separately for subsequent data processing. The navigator axis was placed along the lung-liver interface. Measurements were performed to determine the most stable

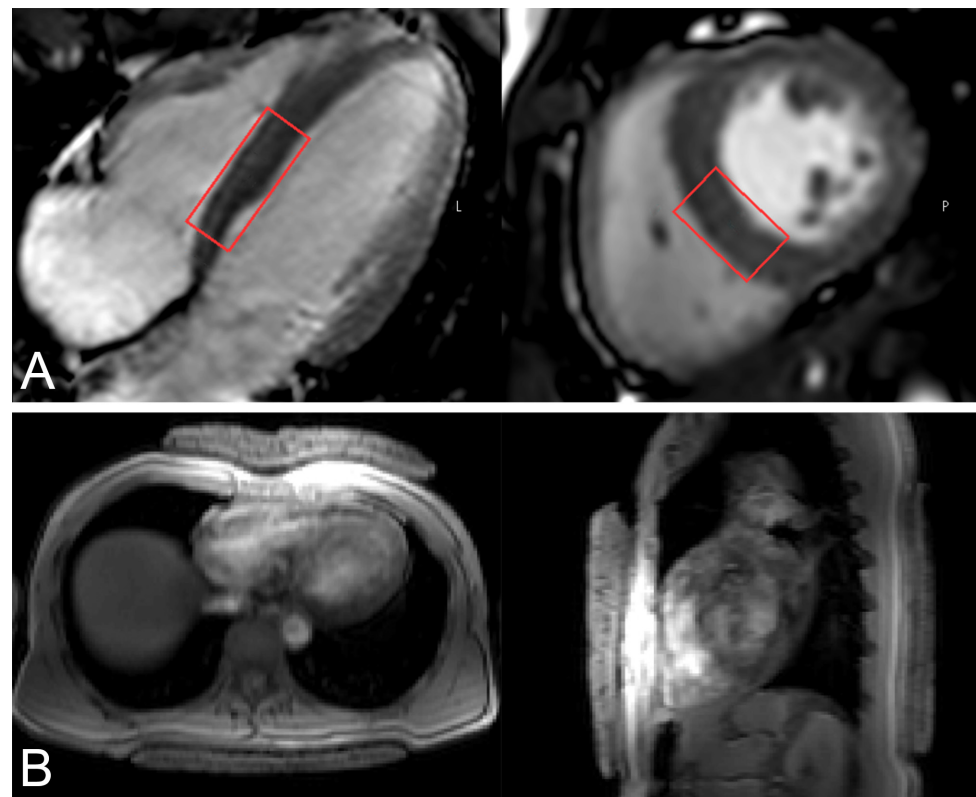


FIGURE 1. A, Placement of the spectroscopy voxel (red box) in the interventricular septum on the 4-chamber and short axis view. **B,** Placement of the HP pads shown on the transverse and sagittal survey scan. Both the anterior and

posterior HP pads were centered on the location of the spectroscopy VOI in both the feet-head and left-right direction. Figure 1 can be viewed online in color at www.investigativeradiology.com.

cardiac phase for the electrocardiographical triggering delay and resulted in a post R-wave delay of 200 to 250 milliseconds, depending on the heart rate, which agrees with results from previous authors.¹³ For 11 volunteers, transmit field (B_1^+) maps were measured based on the saturated double-angle method.¹⁴ Reception sensitivity (B_1^-) maps were calculated in 4 volunteers. This was done by acquiring electrocardiography-triggered 3-dimensional (3D) gradient-echo sequence with a flip angle of 5 degrees, geometrically aligned with the B_1^+ map. The resulting image is proportional to the product of the receive sensitivity and the B_1^+ , as described by Wang et al.¹⁵ The receive sensitivity is then calculated by dividing the 3D gradient-echo image by the B_1^+ .

Preparation of HP Pads

The HP pads were constructed using an aqueous (H_2O) suspension of barium titanate with a 4:1 mass-mass ratio.¹⁰ This results in a very dense mixture with a relative permittivity of approximately 300. Two HP pads, one 2 cm thick (placed anterior) and the other 1 cm thick (placed posterior), with a dimension of $20 \times 20 \text{ cm}^2$ were respectively centered above and below the location of the spectroscopy VOI in both the feet-head and left-right direction (Figure 1B). The weights of these HP pads were 2.3 kg and 1.3 kg, respectively.

Data Processing

The spectra were fitted in the time domain to a Gaussian line shape using the advanced method for accurate, robust, and efficient spectral fitting algorithm in Java-Based Magnetic Resonance User Interface (jMRUI v5.0; MRUI Project).¹⁶ As prior knowledge, the linewidth of the CH_3 resonance was set to be equal to that of the $(\text{CH}_2)^n$ groups, and the frequency of the CH_3 peak was fixed at -0.4 ppm with respect to the frequency of the $(\text{CH}_2)^n$ peak. The SNR is defined as the summed amplitude of the spectral component of the triglyceride-methyl (CH_3) and the triglyceride-methylene (CH_2)ⁿ peaks divided by the SD of the noise. The noise was taken from the last 100 data points of the time-domain free induction decay, which was confirmed to be signal free. The total MTGC was calculated using the following equation;

$$\text{MTGC} = \frac{\text{triglyceride methyl } (\text{CH}_3) + \text{triglyceride methylene } (\text{CH}_2)^n}{\text{water} + \text{triglyceride methyl } (\text{CH}_3) + \text{triglyceride methylene } (\text{CH}_2)^n} \times 100\% \quad (\text{Equation 1})$$

The SNR for reduced scan times was calculated for 48 to 36, 24, and 12 averages, reducing the mean acquisition times from 5 to 3.75, 2.5, and 1.25 minutes, respectively, to study the effect of scan time on SNR without and with pads. To test the effect of the HP pads on the linewidth, the full width at half maximum of the water peak was measured in all volunteers. The average transmit power values from the RF amplifier were read from the log file produced by the scanner.

Statistical Analysis

All statistical analyses were performed by using statistical software IBM SPSS Statistics (version 20, IBM, Chicago, IL). Numerical data were reported as mean (SD). A paired samples Student t test was performed to compare SNR, spectral linewidths, fat fraction, and RF transmit power without and with the HP pads. Data were considered statistically significant at P values less than 0.05.

RESULTS

Signal-to-Noise Ratio

Three different spectra from a single volunteer are shown in Figure 2. The SNR is increased by 90% for this volunteer by applying the HP pads, as shown by comparing the middle and left spectra. A comparison of the middle and right spectra shows that the same spectral SNR can be achieved using the pads with 60% fewer signal averages.

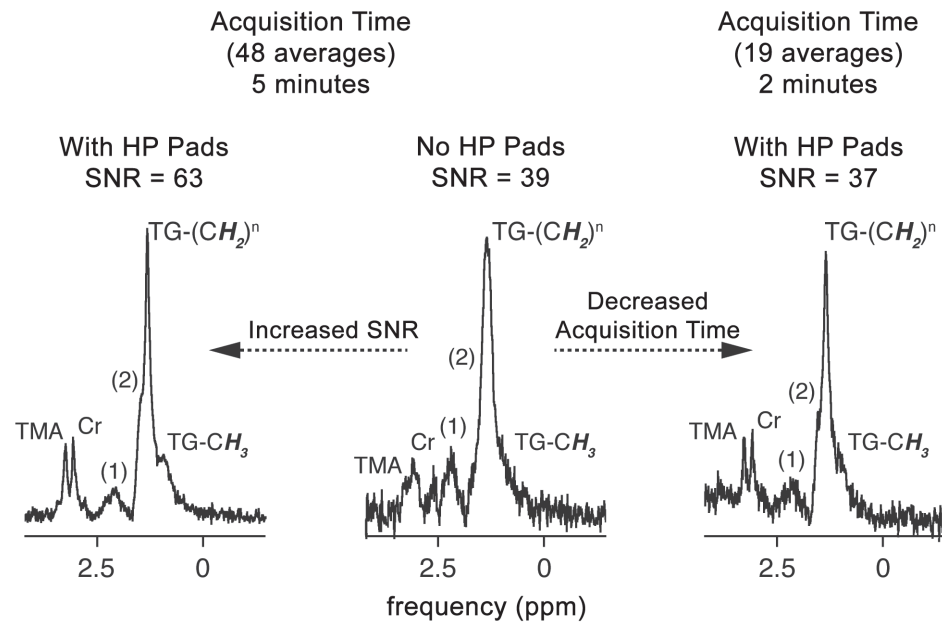


FIGURE 2. Three water-suppressed spectra of a single volunteer. The spectrum on the left was acquired with the HP pads, and the spectrum in the center was acquired without the pads in place. The spectrum on the right is identical to the left spectrum (with HP pads) but has been reconstructed with only the first 19 averages of the total 48

averages. Multiple triglyceride resonances [CH₃ at 0.9 ppm, [CH₂]ⁿ at 1.3 ppm, CH₂CH₂COO marked with number 2 at 1.5 ppm, CH₂CH = CHCH₂ and CH₂COO marked with number 1 around 2.1 ppm], a creatine methyl resonance at 3.0 ppm, and a trimethylammonium resonance at 3.2 ppm can be distinguished in the spectrum.

In Figure 3, the MTG SNR is plotted for each volunteer without and with HP pads. The mean (SD) SNR increased from 27.9 (15.6) to 42.3 (24.4) ($P < 0.0001$), and the SNR change ranged from -4.0 to $+44.0$ with an average increase of 14.2. The mean gain in SNR by using the HP pads is 60%. Measurements of the noise showed a significant increase with the pads in place ($3.36e^{-6}$ [8.04] without, $4.06e^{-6}$ [9] and with pads), implying a closer coupling to the region of interest, resulting in an overall increase in SNR.

In Figure 4, the SNR of the MTG signal as a function of the acquisition time is shown for a single volunteer. It can be seen that significant reductions in time, for this volunteer from 5 minutes to a just over 2 minutes (similar to the data shown in Figure 2), can be achieved by using the HP pads while maintaining the same SNR equal compared with the scan without the HP pads.

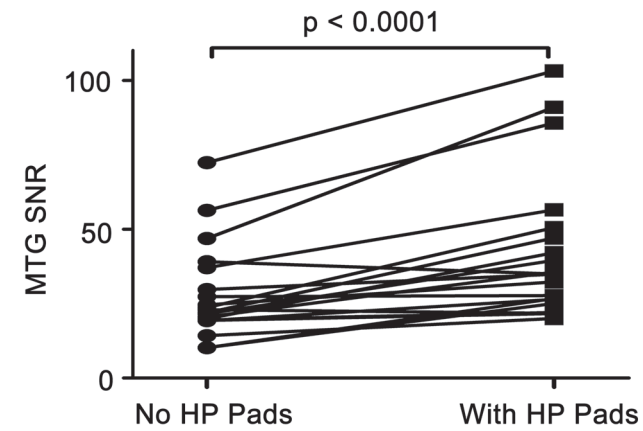


FIGURE 3. Myocardial triglyceride SNR for all 20 volunteers without and with the HP pads (48 averages).

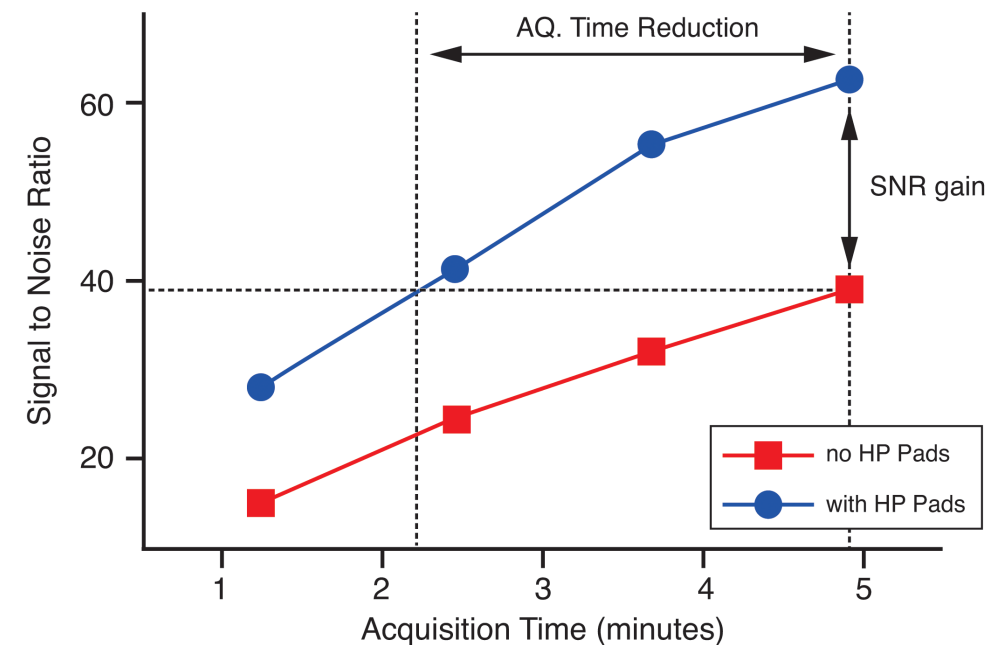


FIGURE 4. Signal-to-noise ratio of the MTG signal against acquisition time, acquired in the same volunteer as shown in Figure 2, without and with the HP pads. The horizontal dotted line is the SNR level of the total acquisition (5 minutes) without the HP pads. This plot shows the SNR of

the full scan without pads is reached in just over 2 minutes when using the HP pads effectively cutting acquisition time more than half. Figure 4 can be viewed online in color at www.investigativeradiology.com.

Linewidth

There was no significant difference ($P = 0.80$) in the linewidths without and with the HP pads, the values being 17.4 (4.9) Hz and 17.1 (3.2) Hz, respectively.

Transmit and Receive Sensitivities

The peak B_1^+ available on the scanner is 13.5 μT . Without the HP pads, the transmit field strength in the VOI was 11.2 (1.4) μT , whereas with the pads, a transmit field of 12.5 (1.3) μT was reached ($P = 0.0001$). This translates to an average increase in B_1^+ of 12% in the VOI. The average required power for the scan was 20.9 W without the HP pads and 17.1 W with the HP pads ($P < 0.0001$). The receive sensitivity (B_1^-) increased from 326 (50) without the HP pads to 424 (45) with the HP pads. This translates to an average increase in B_1^- of 30% in the VOI. Figure 5A shows transmit (B_1^+) fields per square root of input power in a single volunteer without and with the HP pads. The field is plotted along the long axis of the selected volume shown in Figure 1. Figure 5B shows the corresponding B_1^+ field achieved with the slice-selective power optimization on the scanner, and Figure 5C shows the calculated receive sensitivity (B_1^-) maps.

Myocardial Triglyceride Content

The MTGC was calculated to be 0.39% (0.17%) without the HP pads and 0.38% (0.15%) with the HP pads ($P = 0.83$).

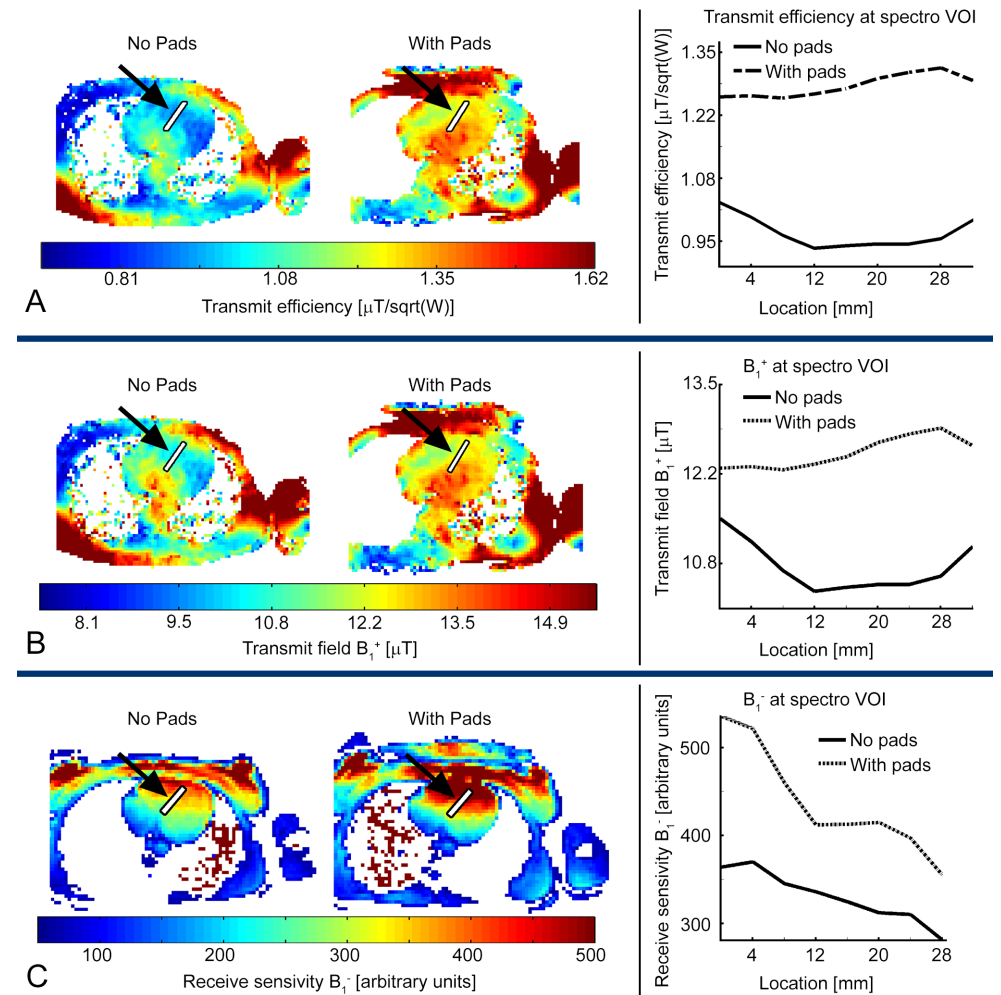


FIGURE 5. A, The transmit efficiency is shown in the left panel for a single volunteer with and without pads. On the right the transmit efficiency is plotted along the voxel of interest. **B,** On the left the B_1^+ maps are shown for a single volunteer without and with the HP pads. The gain in SNR was 40% for this volunteer. The maximum transmit field from the body coil is set at 13.5 μT . On the right, the B_1^+ intensity is plotted at the location of the spectroscopy voxel

that is noted as a white line from anterior to posterior in the B_1^- maps. **C,** The left panel shows B_1^- maps of a single volunteer without and with the HP pads placed. The gain in SNR was 110% for this volunteer. In the right panel, B_1^- intensity is plotted at the location of the voxel of interest that is noted as a white line from anterior to posterior in the B_1^- maps. Figure 5 can be viewed online in color at www.investigativeradiology.com.

DISCUSSION

The main finding of this study is that the HP pads significantly increase the SNR of cardiac ^1H -MRS at 3 T. The increased SNR can be exploited to reduce the number of required signal averages, reducing the mean acquisition time by 60%. The acquisition time for our standard MRS protocol can in this way be reduced from 5 minutes to only 2 minutes for the same spectral quality. These results are in line with a previous study on the effects of HP pads on cardiac imaging,¹⁰ although in that particular study quantitative analysis was performed across the entire cardiac volume, rather than the much smaller section of the myocardial wall from which spectra were acquired in this study. The authors found significant increases in receive sensitivity close to the anterior section of the heart, with Figure 5 displaying an approximately 30% increase in receive sensitivity, very similar to that quantitatively determined in this current study.

Our results show that the main factor responsible for the increased SNR is the 30% increase in receive sensitivity due to an increased coupling between the coil array and the body by using the HP pads. The transmit field increased by 12% on average accompanied by an 18% decrease in average power resulting in a significantly increased transmit efficiency. This effect was also seen in a previous study, which considered the effects of the HP pads in cardiac imaging.¹⁰ No significant differences in spectral linewidth were measured using the HP pads, which can be explained by the large distance between HP pads and the VOI. From the SNR results for all volunteers, it was noted that, in 2 of the total 20 volunteers, adding the pads decreased the SNR. This did not seem to be related to body size or sex and is most likely related to faulty placement of the pads. We also observed a large variance in spectral SNR between the different volunteers. This variance did not seem to be correlated with body mass index but more likely to the chest size and subcutaneous fat levels. Although volunteers noted the extra weight of the HP pad in addition to that of the receive array on their chest, they did not rate this as uncomfortable. The effect on the SAR of the HP pads has been described previously in the study by Brink and Webb¹⁰ (Figure 3). They showed that the local increase in transmit efficiency resulted in lower input power being required to produce a given transmit field, which therefore reduced the local SAR throughout the body.

Despite the clear increase in SNR afforded by the use of the HP pads, it is important that their use does not introduce a measurement bias into the MTGC quantification. Our results showed statistically identical values without (0.39% [0.17%]) and with (0.38% [0.15%]) the HP pads ($P = 0.83$), meaning that lipid quantification is not affected by using the pads. The MTGC for the healthy volunteers was in agreement with previous studies.^{17–19}

In conclusion, HP pads improve cardiac ^1H -MRS at 3 T by increasing the SNR on average by 60%, which can be used to reduce data acquisition time, significantly allowing fast assessment of MTGC without compromising spectral quality. The same pads as the Brink and Webb (MRM 2014) study were used for this study. This set of pads was optimized to “maximize the average transmit efficiency and to minimize the B_1 inhomogeneity (s), over the entire 3D heart volume”. As such, there may be some improvements that could be made because we are interested in a relatively small subsection of the heart for spectroscopy.

REFERENCES

1. Bizino MB, Hammer S, Lamb HJ. Metabolic imaging of the human heart: clinical application of magnetic resonance spectroscopy. *Heart*. 2014;100:881–890.
2. Bottomley PA, Weiss RG. Non-invasive magnetic-resonance detection of creatine depletion in non-viable infarcted myocardium. *Lancet*. 1998;351:714–718.
3. Kankaanpää M, Lehto HR, Pärkkä JP, et al. Myocardial triglyceride content and epicardial fat mass in human obesity: relationship to left ventricular function and serum free fatty acid levels. *J Clin Endocrinol Metab*. 2006;91:4689–4695.
4. McGavock JM, Lingvay I, Zib I, et al. Cardiac steatosis in diabetes mellitus: a ^1H -magnetic resonance spectroscopy study. *Circulation*. 2007;116:1170–1175.
5. Nakae I, Mitsunami K, Omura T, et al. Proton magnetic resonance spectroscopy can detect creatine depletion associated with the progression of heart failure in cardiomyopathy. *J Am Coll Cardiol*. 2003;42:1587–1593.
6. Reingold JS, McGavock JM, Kaka S, et al. Determination of triglyceride in the human myocardium by magnetic resonance spectroscopy: reproducibility and sensitivity of the method. *Am J Physiol Endocrinol Metab*. 2005;289:E935–E939.
7. Szczepaniak LS, Dobbins RL, Metzger GJ, et al. Myocardial triglycerides and systolic function in humans: in vivo evaluation by localized proton spectroscopy and cardiac imaging. *Magn Reson Med*. 2003;49:417–423.
8. van der Meer RW, Doornbos J, Kozerke S, et al. Metabolic imaging of myocardial triglyceride content: reproducibility of ^1H MR spectroscopy with respiratory navigator gating in volunteers. *Radiology*. 2007;245:251–257.
9. Stephenson MC, Gunner F, Napolitano A, et al. Applications of multi-nuclear magnetic resonance spectroscopy at 7T. *World J Radiol*. 2011;3:105–113.
10. Brink WM, Webb AG. High permittivity pads reduce specific absorption rate, improve B_1 homogeneity, and increase contrast-to-noise ratio for functional cardiac MRI at 3 T. *Magn Reson Med*. 2014;71:1632–1640.
11. Bottomley PA. Spatial localization in NMR spectroscopy in vivo. *Ann NY Acad Sci*. 1987;508:333–348.
12. Schär M, Kozerke S, Boesiger P. Navigator gating and volume tracking for double-triggered cardiac proton spectroscopy at 3 Tesla. *Magn Reson Med*. 2004;51:1091–1095.
13. Carlsson Åsa, Sohlín Maja, Ljungberg Maria, et al. The cardiac triggering time delay is decisive for the spectrum quality in cardiac ^1H MR Spectroscopy. *Proc Intl Soc Mag Reson Med*. 2012;20:1793.
14. Cunningham CH, Pauly JM, Nayak KS. Saturated double-angle method for rapid B_1^+ mapping. *Magn Reson Med*. 2006;55:1326–1333.
15. Wang J, Yang QX, Zhang X, et al. Polarization of the RF field in a human head at high field: a study with a quadrature surface coil at 7.0 T. *Magn Reson Med*. 2002;48:362–369.
16. Naressi A, Couturier C, Devos JM, et al. Java-based graphical user interface for the MRUI quantitation package. *MAGMA*. 2001;12:141–152.
17. Weiss K, Martini N, Boesiger P, et al. Cardiac proton spectroscopy using large coil arrays. *NMR Biomed*. 2013;26:276–284.
18. Rial B, Robson MD, Neubauer S, et al. Rapid quantification of myocardial lipid content in humans using single breath-hold ^1H MRS at 3 Tesla. *Magn Reson Med*. 2011;66:619–624.
19. Faller KM, Lygate CA, Neubauer S, et al. ^1H -MR spectroscopy for analysis of cardiac lipid and creatine

4

PARAMETER
OPTIMIZATION FOR
REPRODUCIBLE
CARDIAC ^1H -MR
SPECTROSCOPY
AT 3 TESLA

4 PARAMETER OPTIMIZATION FOR REPRODUCIBLE CARDIAC ¹H-MR SPECTROSCOPY AT 3 TESLA

Adapted from *Journal of Magnetic Resonance Imaging*. 2016 Nov;44(5):1151-1158

Authors

Paul de Heer, MSc,¹ Maurice B. Bizino, MD,² Hildo J. Lamb, MD, PhD,² and Andrew G. Webb, PhD¹

¹ C.J. Gorter Center for High Field MRI, Department of Radiology, Leiden University Medical Center, Leiden, the Netherlands.

² Department of Radiology, Leiden University Medical Center, Leiden, the Netherlands.

ABSTRACT

Purpose:

To optimize data acquisition parameters in cardiac proton MR spectroscopy, and to evaluate the intra- and intersession variability in myocardial triglyceride content.

Materials and Methods:

Data acquisition parameters at 3 Tesla (T) were optimized and reproducibility measured using, in total, 49 healthy subjects. The signal-to-noise-ratio (SNR) and the variance in metabolite amplitude between averages were measured for: (i) global versus local power optimization; (ii) static magnetic field (B_0) shimming performed during free-breathing or within breathholds; (iii) post R-wave peak measurement times between 50 and 900 ms; (iv) without respiratory compensation, with breathholds and with navigator triggering; and (v) frequency selective excitation, Chemical Shift Selective (CHESS) and Multiply Optimized Insensitive Suppression Train (MOIST) water suppression techniques. Using the optimized parameters intra- and intersession myocardial triglyceride content reproducibility was measured. Two cardiac proton spectra were acquired with the same parameters and compared (intrasession reproducibility) after which the subject was removed from the scanner and placed back in the scanner and a third spectrum was acquired which was compared with the first measurement (intersession reproducibility).

Results:

Local power optimization increased SNR on average by 22% compared with global power optimization ($P = 0.0002$). The average linewidth was not significantly different for pencil beam B_0 shimming using free-breathing or breathholds (19.1 Hz versus 17.5 Hz; $P = 0.15$). The highest signal stability occurred at a cardiac trigger delay around 240 ms. The mean amplitude variation was significantly lower for breathholds versus free-breathing ($P = 0.03$) and for navigator triggering versus free-breathing ($P = 0.03$) as well as for navigator triggering versus breathhold ($P = 0.02$). The mean residual water signal using CHESS (1.1%, $P = 0.01$) or MOIST (0.7%, $P = 0.01$) water suppression was significantly lower than using frequency selective excitation water suppression (7.0%). Using the optimized

parameters an intrasession limits of agreement of the myocardial triglyceride content of -0.11% to $+0.04\%$, and an intersession of -0.15% to $+0.9\%$, were achieved. The coefficient of variation was 5% for the intrasession reproducibility and 6.5% for the intersession reproducibility.

Conclusion:

Using approaches designed to optimize SNR and minimize the variation in inter-average signal intensities and frequencies/phases, a protocol was developed to perform cardiac MR spectroscopy on a clinical 3 T system with high reproducibility.

INTRODUCTION

Cardiac proton MR spectroscopy (MRS) can be used to study the effects of lipid accumulation and lipid toxicity in the heart by means of quantitative measurement of the myocardial triglyceride content (MTGC).^{1,2} This value is relevant in patients with metabolic syndrome and type 2 diabetes mellitus (DM2), because higher levels have been linked to an increased risk of heart failure.³ Because the metabolic syndrome and DM2 can potentially be reversed by therapy or diet, it is important to have a reliable and quantitative way of measuring cardiac lipid accumulation. Currently, the application of MRS is limited to clinical research mainly due to the complexity of the technique in terms of the number of parameters which need to be optimized. These include breathing-motion compensation technique because motion due to breathing introduce dynamic variations in the local static magnetic field leading to an increase in spectral linewidth and decrease in the signal-to-noise ratio (SNR) of the lipid peaks.

Similar effects are seen due to the motion related to the cardiac cycle, deformation of the septum as well as the in- and outflow of blood, therefore, the acquisition must be triggered to the cardiac cycle. Transmit field ($B^{1\alpha}$) inhomogeneity across the heart leads to under- or overestimation of the tip angle in the myocardial wall if conventional global power optimization routines are used, and subsequently lead to loss in the SNR.^{4,5} It has also been shown that the nonuniform flip angle distribution results in sections of the free right ventricular wall and the mid-ventricular and apical septum being obscured.^{6,7} The low abundance of lipid protons (generally > 100 times less abundant than water protons) means that many signal averages must be acquired, and a high degree of phase stability between averages is required for optimal SNR.^{2,8-11} Because the water signal is much larger than the lipid signal, the water signal needs to be efficiently suppressed to minimize baseline distortions and spurious signals that otherwise complicate metabolite quantification due to vibration induced signal modulations.¹²

The aim of this study is to optimize five of the main parameters and methods used in cardiac proton MRS measurements, namely the method of RF power optimization, B_0 shimming, the measurement point within the cardiac cycle, the method of respiratory motion compensation and the choice of water suppression technique. The choices made also considered the requirement of minimal input from the user to make the overall protocol more robust in order to incorporate it into a clinical scan. Finally, we use these optimized parameters to assess the intra- and intersession reproducibility of cardiac MRS in healthy volunteers.

MATERIALS AND METHODS

Participants

The study was approved by the institutional review board, and written informed consent was obtained from all participants. The study was conducted according to the principles expressed in the Declaration of Helsinki. Forty-nine healthy subjects underwent cardiac MRS between July 2013 and September 2015.

Data Acquisition

Experiments were performed on a 3 Telsa (T) Ingenia whole-body MRI scanner (Philips Healthcare, Best, Netherlands). The body coil was used for transmission and an anterior (16 elements) and a posterior (12 elements) array for reception. The most commonly used sequence in cardiac MRS is point resolved spectroscopy (PRESS)^{8,13-16} due to its availability as a standard “product sequence” on commercial platforms, and the fact that it gives twice the SNR of the stimulated echo acquisition method (STEAM) method.¹⁷ Two disadvantages of PRESS localization compared with STEAM are the increased chemical shift displacement and increased minimal echo time.

However, because for this study we were mainly interested in a small chemical shift range of the lipid peaks (CH_2)ⁿ at 1.3 ppm and CH_3 at 0.9 ppm, this will result in only a minor mismatch in the location of the two metabolites. If both the lipids (1.3 ppm) as well as creatine (3 ppm) are of interest, care should be taken planning the spectroscopy voxel to ensure the creatine still falls within the septum. The water signal (4.7 ppm) used as a reference for the lipid quantification does have a significantly different chemical shift; however, data for non-water-suppressed spectra are acquired with a different transmitter offset, resulting in overlap of the spectroscopic volume of interest (VOI) of the lipid- and water-acquisition. The increased minimal echo time does negate the theoretical double SNR of PRESS localization compared with STEAM; however, this effect is only large when the T^2 of the metabolite of interest low. In a previous study, it has been shown that the use of a high permittivity pads increases the SNR of localized cardiac spectra without affecting spectral linewidth.¹⁸ A similar arrangement was used in this study. A first order pencil beam shimming technique was used to shim the static magnetic field (B_0). This technique requires minimal user input and reconstructs the B_0 distribution in the spectroscopy voxel by capturing multiple (nine) projections.

A 30 s survey and a single breathhold coronal image were acquired to plan the navigator volume. Four-chamber and shortaxis cine images were acquired to plan the MRS voxel in the myocardial interventricular septum. Spectra were recorded using PRESS localization with an echo time (TE) of 35 ms and a repetition time (TR) of 9 s for the non-water-suppressed spectra, and 3.5 s for the water-suppressed spectra to ensure full relaxation of the water and lipid signals. The spectroscopic VOI (15 x 25 x 40 mm³) was placed in the interventricular septum and pencil beam B_0 shimming was performed on this VOI. The bandwidth of the MRS acquisition was 1500 Hz and 2048 samples were acquired resulting in spectral resolution of 0.73 Hz / sample. Five different parameters were optimized as described below:

Power Optimization.

Spectra were acquired in 15 subjects comparing the standard system “global” power optimization with “local” power optimization. Global in this case refers to the fact that power optimization is performed by integrating the signal intensity over an entire trans-

verse slice through the heart, whereas local applies only to the spectroscopic VOI. It is well-known that there is substantial variation in the transmit (B_1^+) field through the body (and within the heart itself) at 3 T, and so global power optimization is unlikely to result in the correct tip angles within the spectroscopic VOI.⁴ Previous studies reported a variation in B_1^+ of 100% over the short axis of the heart.⁵⁻⁷ Local power optimization method was performed by monitoring the intensity of the water peak and incrementing the tip angles of the excitation pulse and the two refocusing pulses in the PRESS sequence in steps of 5% (range, 90%–150% of the global power optimization result), and choosing the power which produced the maximum signal intensity. The SNR of the water signal was compared for the local and global power optimization using a Wilcoxon signed-rank test.

Comparison of Spectral Linewidth for Freebreathing and Breathhold B_0 Shimming.

First order B_0 pencil beam shimming (nine projections) was performed during freebreathing and in two breathholds of 13 s (max. five projections per breathhold) in eight healthy subjects, after which non-water-suppressed spectra (four averages) were acquired. The full width at half maximum (FWHM) of the water peak was determined for each spectrum and compared using a Wilcoxon signed rank test. To determine the reproducibility of the B_0 shimming, each scan was repeated three times in each subject and the standard deviation determined for these three measurements.

Amplitude Stability as a Function of the Measurement Point within the Cardiac Cycle.

Non-water-suppressed spectra (16 averages) were acquired in three subjects at eight different times (50, 150, 200, 250, 300, 500, 700, and 900 ms) after the peak of the R-wave. The variation of the signal was determined by calculating the standard deviation of the water signal amplitude. The average heart rate was recorded for each subject.

Comparison of Signal Reproducibility Between Freebreathing, Breathhold, and Navigator Triggering.

Non-water-suppressed spectra (16 averages) were acquired in seven subjects with free-breathing, breathholds and navigator triggered respiratory compensation.¹³ The breathhold acquisition was performed in eight breathholds of 18 s acquiring two averages per breathhold. The navigator volume was placed on the lung–liver interface and had a gating window of 3 mm. The navigator triggers the spectroscopy sequence and tracks the position of the diaphragm updating the spectroscopy voxel location dynamically with respect to the actual position of the heart. The stability of the amplitude was determined by calculating the standard deviation of the signal for the three respiratory compensation methods. The variations of the center frequency and phase of the water signal were also determined. The amplitude variation, center frequency variation, and phase variations for the three different methods were compared using Friedman's test and post hoc Wilcoxon signed rank test.

Efficiency of Different Water Suppression Methods.

Three different water suppression techniques were assessed in eight subjects: frequency selective excitation,¹⁹ Chemical Shift Selective (CHESS)^{20,21} and Multiply Optimized Insensitive Suppression Train (MOIST) water suppression.²² Frequency selective excitation water suppression uses two selective RF pulses combined with crusher gradients to minimize the water magnetization at the beginning of the acquisition. CHESS water

suppression uses three narrowband chemical shift selective pulses, while MOIST water suppression uses four phase-modulated RF pulses, such that the longitudinal magnetization of the water signal is minimized at the beginning of the acquisition. Four non-water-suppressed averages and 16 water-suppressed averages were acquired for each subject. A residual water fraction was calculated by dividing the water signal in the suppressed spectrum by the water signal in the non-water-suppressed spectrum. A Friedman's test was performed to analyze differences in the residual water signal between the three water suppression techniques, and post hoc tests were performed with the Wilcoxon signed-rank test. Spectra were also visually inspected to assess spectral quality in terms of baseline distortion and the presence of spurious signals from incomplete water suppression.

Assessment of the Inter- and Intrasession Reproducibility of MTGC Quantification

Using the optimized parameters derived in the results section, spectra (6 averages without water suppression, 32 averages with water suppression) were acquired in eight subjects. The MTGC was calculated from the formula:

$$\text{MTGC} = \frac{\text{triglyceride methyl (CH}_3\text{)} + \text{triglyceride methylene (CH}_2\text{)}^n}{\text{water} + \text{triglyceride methyl (CH}_3\text{)} + \text{triglyceride methylene (CH}_2\text{)}^n} \times 100\% \quad (\text{Equation 1})$$

The scan was then repeated and the MTGC of the two scans compared with determine the intrasession reproducibility. In seven of the eight cases (one was not possible due to a 1 h time limit on scanning), the subject was then fully removed from the scanner, positioned back on the patient bed, and the protocol was re-run to determine the intersession reproducibility. To determine the intersession reproducibility, spectra were compared with the first scan acquired. The coefficient of variation (C_V) was determined and the Spearman correlation coefficient was calculated to determine the intra- and intersession correlation and Bland-Altman plots were constructed.

Data Processing

All spectra were fitted in the time-domain using the Java-based MR User Interface (jMRUI).²³ The advanced method for accurate, robust and efficient spectral fitting (AMARES) algorithm was used to fit the resonances to a Gaussian line shape. The water and lipid SNRs were defined as the integrated area under the water peak and the sum of the integrated area under the triglyceride-methyl (CH_3) and the triglyceride-methylene (CH_2)ⁿ peaks, divided by the standard deviation (SD) of the noise, respectively. The noise was taken from the last 100 points of the free induction decay.

Statistical Analysis

All statistical analyses were performed using the statistical software IBM SPSS Statistics (version 20, IBM, Chicago, IL). Plots were created using GraphPad Prism (GraphPad Software, San Diego, CA). Numerical data were reported as mean \pm standard deviation. Data were considered statistically significant at P-values < 0.05.

RESULTS

POWER OPTIMIZATION

Figure 1 shows water-suppressed spectra acquired using global and local power optimizations in a male subject with a body mass index (BMI) of 30.3 kg/m². The SNR of the lipid increased from 17 to 38 arbitrary units (a.u.) using the local power optimization compared with the global power optimization. Figure 2 plots the SNR of the water signal for all 15 subjects. The spectra of 13 of the 15 subjects show a higher SNR using local power optimization compared with global power optimization, while for the remaining two subjects the SNR did not differ. The mean SNR (\pm SD) of the water signal was 1787 (\pm 787) using global power optimization versus 2173 (\pm 626) for local power optimization ($P = 0.0002$).

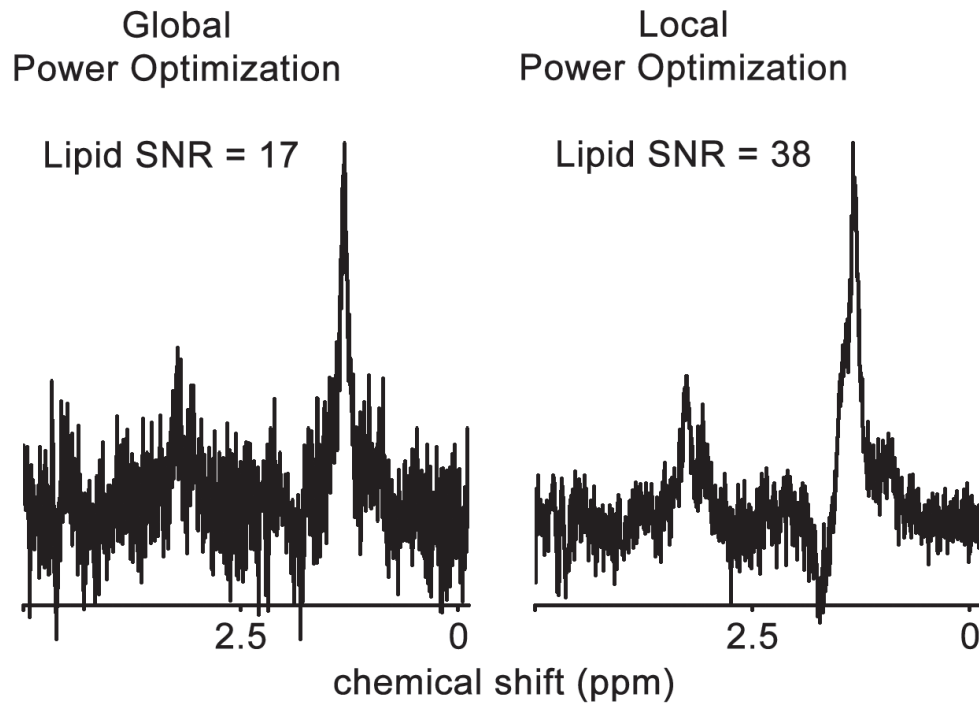


FIGURE 1: Cardiac MR spectrum acquired with global power optimization (left), a spectrum (right), in the same subject, is shown using local power optimization within the spectroscopic VOI.

COMPARISON OF SPECTRAL LINEWIDTHS FOR FREE-BREATHING AND BREATHHOLD B_0 SHIMMING

The mean linewidth after performing pencil-beam B_0 shimming during free-breathing was 19.1 Hz (\pm 3.2 Hz) compared with 17.5 Hz (\pm 4.6 Hz) when shimming was performed during breathholds: these values were not significantly different ($P = 0.15$). The mean of the standard deviation of the three successive linewidth measurements in each volunteer was 2.3 Hz (free-breathing) and 1.5 Hz (breathholds).

Power optimization method

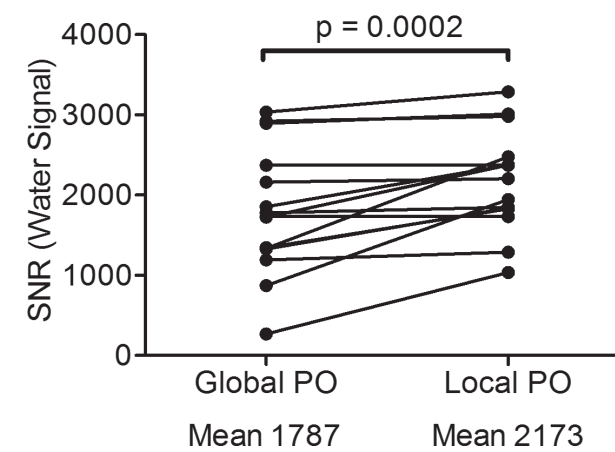


FIGURE 2: SNR of the water signal for global- and local power optimization in 15 subjects. The spectra of 13 of the 15 subjects show a higher SNR using local power optimization compared with global power optimization, while for the remaining two subjects the SNR did not differ.

AMPLITUDE STABILITY AS A FUNCTION OF THE MEASUREMENT POINT WITHIN THE CARDIAC CYCLE

Figure 3 plots the standard deviation of the nonsuppressed water signal as a function of the cardiac trigger delay for three subjects. The average standard deviations were 0.18, 0.06, 0.07, 0.06, 0.22, 0.34, 0.15, and 0.15 for a cardiac trigger delay of 50, 150, 200, 250, 300, 500, and 700 ms, respectively. For all subjects, the SD had a minimum value, corresponding to the highest signal stability, at a trigger delay around 240 ms. This value agrees well with a previous study,²⁴ which is why only a relatively small number of subjects were used for this particular optimization step.

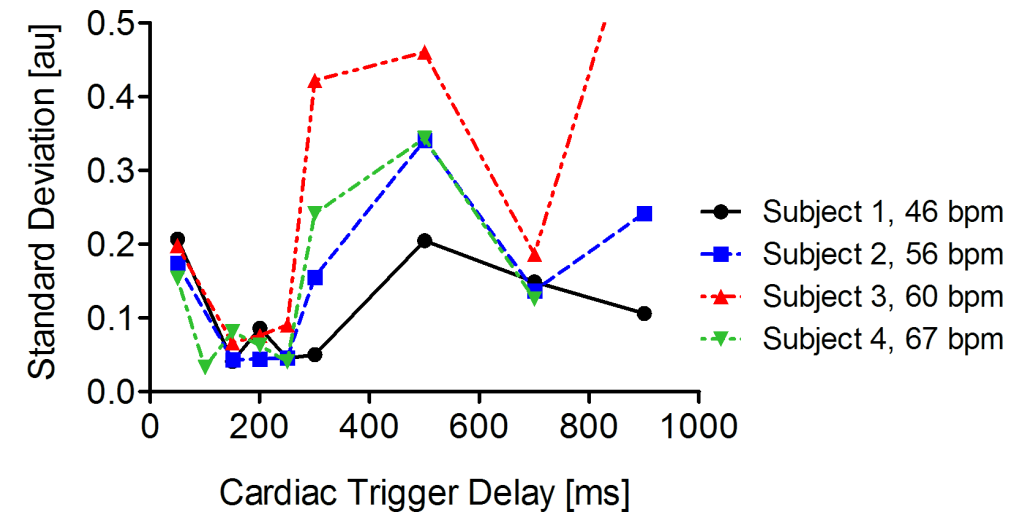


FIGURE 3: Standard deviation of the water signal for eight measurement time points in the cardiac cycle. The lowest standard deviation and thus the most stable measurement point in the cardiac cycle is around 200 ms after the peak of the R-wave. The heart rate is shown in beats per minute (bpm).

COMPARISON OF SIGNAL REPRODUCIBILITY BETWEEN FREE-BREATHING, BREATH-HOLD, AND NAVIGATOR TRIGGERING

The mean variations of the amplitude ($P = 0.001$), frequency ($P = 0.001$) and phase ($P = 0.016$) of the water peak were significantly different for the three different breathing compensation methods (Figure 4). The mean amplitude variation was significantly lower for breathholds versus free-breathing (0.09 versus 0.22; $P = 0.03$) and for navigator triggering versus free-breathing (0.06 versus 0.22; $P = 0.03$), as well as for navigator triggering versus breathhold (0.06 versus 0.09; $P = 0.02$).

The mean variation of the water peak center frequency was 4.81 Hz (± 5.18 Hz), 2.86 Hz (± 2.82 Hz), and 1.37 Hz (± 0.71 Hz) using free-breathing, breathholds, and navigator triggering, respectively ($P = 0.008$). The center frequency variation was significantly lower for breathholds versus free-breathing ($P = 0.05$) and for navigator triggering versus free-breathing ($P = 0.02$). The mean (SD) variation of the signal phase was 0.22 radians (± 0.07 radians), 0.13 radians (± 0.05 radians), and 0.12 radians (± 0.02 radians) using free-breathing, breathholds, and navigator triggering, respectively ($P = 0.016$). The center frequency variation was significantly lower for breathholds versus free-breathing ($P = 0.05$) and for navigator triggering versus freebreathing ($P = 0.02$).

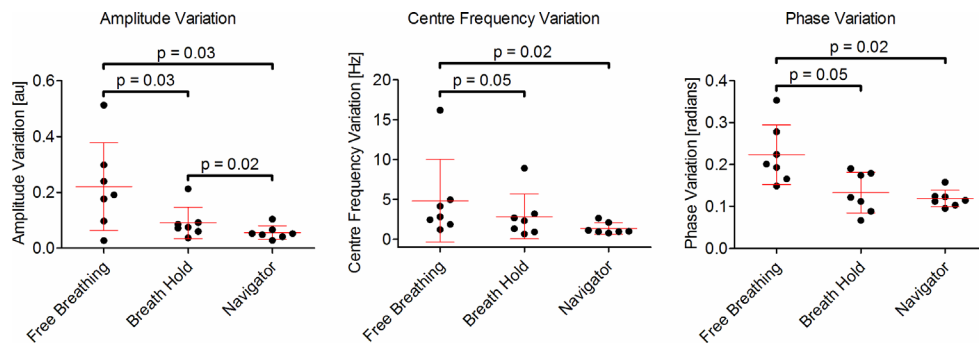


FIGURE 4: Variations in the amplitude, center frequency, and phase of the water signal over 16 acquisitions for free-breathing and two methods of motion compensation. The Friedman's test showed significant differences for the amplitude variation ($P = 0.001$) (left), center frequency variation ($P = 0.001$) (middle), and phase variation ($P = 0.016$) (right). Post hoc tests showed that variations in the

mean amplitude, center frequency and phase were significantly different between free-breathing versus breathholds as well as between free-breathing versus navigator triggering. The mean of the amplitude variation was also significantly different between breathholds and navigator triggering.

EFFICIENCY OF WATER-SUPPRESSION METHODS

Figure 5 shows three water-suppressed spectra with the three different suppression techniques in the same subject. The Friedman's test showed significant differences in the residual water signal for frequency selective excitation, CHES, and MOIST water suppression techniques ($P = 0.001$). Figure 6 shows the results from all subjects. The mean residual water signal was 7.0% (4.8%) using frequency-selective excitation, 1.1% (0.9%) using CHES water-suppression, and 0.7% (0.4%) using the MOIST technique. Both the MOIST ($P = 0.01$) and CHES ($P = 0.01$) techniques gave significantly lower residual water signals than the frequency selective excitation sequence, but there was no statistical significance between MOIST and CHES ($P = 0.46$).

Due to the poor suppression the selective excitation sequence often introduced a significant baseline distortion in the spectrum, making MTGC quantification more difficult. In terms of choosing between the CHES and MOIST techniques, the CHES sequence is relatively long, requiring an increase in the suppression bandwidth to 240 Hz to be able to use a cardiac trigger delay of 200 ms. The length of the MOIST sequence is less than that of CHES, requiring a lower suppression bandwidth of 190 Hz for a trigger delay of 200 ms. Given this, and the slightly higher degree of water suppression, the MOIST sequence was used for MTGC quantitation.

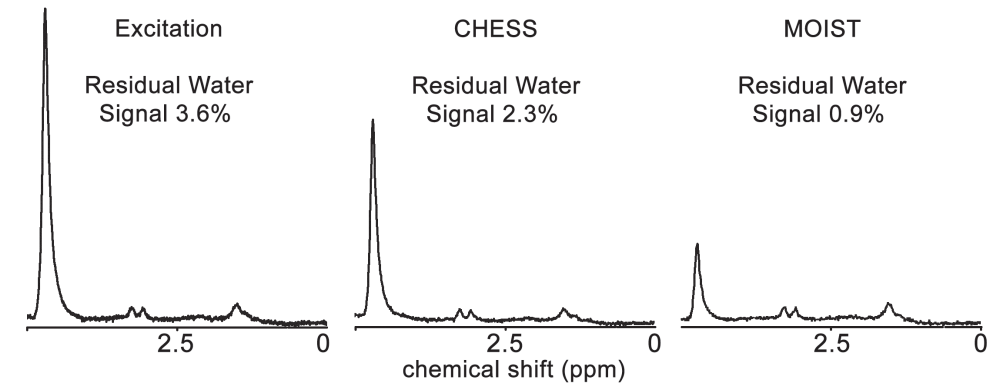


FIGURE 5: Water-suppressed spectra using three different water suppression techniques in the same subject. The residual water signal was calculated by dividing the water peak amplitude from the suppressed spectrum by that in the unsuppressed spectrum.

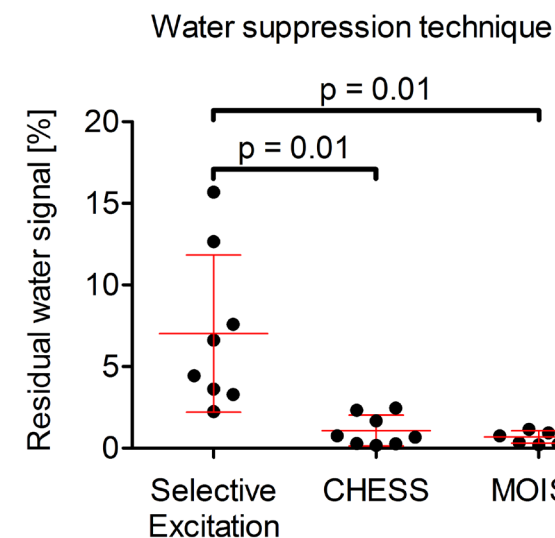


FIGURE 6: Residual water signal for the three different water suppression techniques for all the subjects studied. The residual signals for frequency selective excitation and CHES water suppression were significantly different, as were those for frequency selective excitation and MOIST water suppression.

ASSESSMENT OF THE INTER- AND INTRASESSION REPRODUCIBILITY OF MTGC QUANTIFICATION

Figure 7 shows three spectra acquired from the same volunteer using the optimized scan parameters determined in the previous sections. The spectra on the left and center of Figure 7 were acquired in a single scan session to determine the intrasession reproducibility. The spectrum on the right was acquired in a separate scan session to determine the intersession reproducibility. The mean (\pm SD) MTGC of the intrasessions ($n = 8$) was 0.55% (\pm 0.40%) and 0.59% (\pm 0.42%), with a correlation coefficient $r = 1.000$ ($P < 0.0001$). The coefficient of variation for the intrasession reproducibility was 5% and the Bland-Altman analysis showed a mean difference of 0.04% with limits of agreement from -0.11% to +0.04% (Figure 8A). The mean (\pm SD) MTGC of the intersessions ($n = 7$) was 0.60% (\pm 0.42%) and 0.63% (\pm 0.45%) with a correlation coefficient $r = 1.000$ ($P = 0.0004$). The coefficient of variation for the intersession reproducibility was 6.5% and the Bland-Altman analysis showed a difference of 0.03% and limits of agreement from -0.15% to +0.9% (Figure 8B).

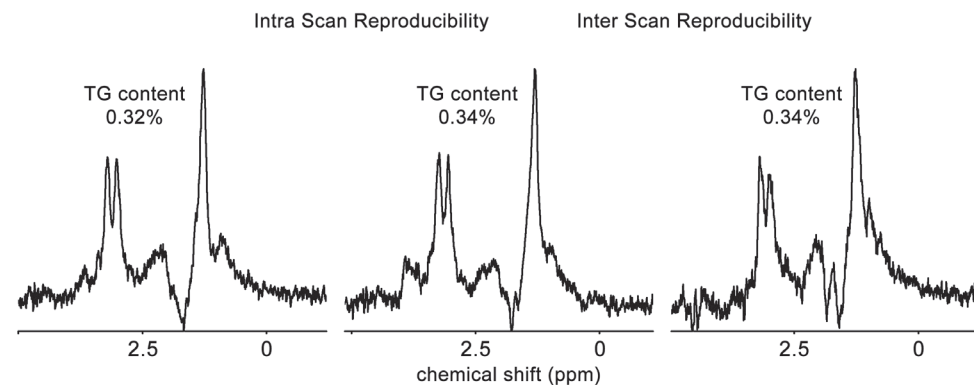


FIGURE 7: Left and center: Two spectra acquired successively are shown to calculate the intrasession reproducibility. Right: A spectrum from the same volunteer acquired in a different scanning session to assess the intersession reproducibility.

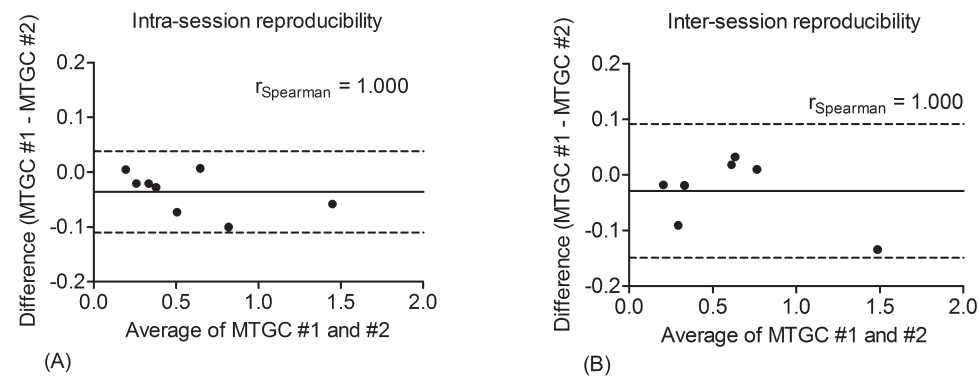


FIGURE 8: Bland-Altman plots for both intra- and intersession reproducibility. The Spearman correlation coefficient was 1.000 for both the intersession (left) and intrasession (right) measurements. The intrasession reproducibility mean difference was 0.04% with limits of agreement from -0.11% to +0.04%. The intersession reproducibility mean difference was 0.03% with limits of agreement from -0.15% to +0.9%.

DISCUSSION

This study looked at the effect of several different data acquisition parameters with the aim of being able to perform reproducible cardiac proton spectroscopy on a clinical 3 T platform. In terms of SNR, using local rather than global power optimization showed a significant increase. Indeed, from the 15 subjects studied there were five cases that resulted in a SNR gain of 35% or more which is in line with a prior study.²⁵ Local power optimization requires no changes to the system software, and so is easy to implement in a clinical setting. We observed that the power underestimation from a global power measurement was greatest in subjects with either high BMI or athletic subjects with high lung volume, but further study would be required to confirm this observation.

With respect to spectral quality, i.e., linewidth and lineshape, there was no statistical difference between performing B_0 shimming during free-breathing or breathholds. In this study we did not compare image-based shimming to the pencil beam technique because the former technique is not implemented on most clinical systems. In the future, this would be interesting to investigate because image-based shimming is generally more robust and gives improved linewidths in cardiac imaging.²⁵

With respect to spectral reproducibility (and SNR because individual spectra are co-added in signal averaging), the key parameters are the measurement point within the cardiac cycle, and the form of motion compensation used. In previous publications some authors have measured in systole and others in the diastolic phase.^{8,9,16,26} The results in this study show that the beginning of the systolic heart phase (200–250 ms after the peak of the R-wave) has the highest stability: this agrees well with the findings of a previous study.²⁴ Given that the range of heart rates was not extensive (range, 46–67 bpm) the optimal measurement point was only minimally affected by the heart rate for these subjects, which can be explained by the small influence of the heart rate on the length of the systolic heart phase.²⁷

In another study of Weiss et al, it was shown that the maximum SNR in cardiac spectroscopy was achieved in midsystole with a trigger delay < 300 ms. However, mid-systole is relatively close to the point that the stability of the signal decreases strongly.²⁸ In that study, they also propose an improved spectroscopy sequence to decrease the sensitivity of the sequence to cardiac motion, using very strong crusher gradients. In earlier studies, it was also shown that respiratory compensation should be used to increase the reproducibility of cardiac MRS.^{13,29,30} Our results show that, by using breathholds, it is possible to increase the signal stability significantly. However, the navigator-based respiratory compensation resulted in significantly lower variations in signal intensity and signal frequency/phase than using breathholds. In addition, many classes of patients have problems maintaining breathholds for prolonged periods of time. Therefore, the navigator-based respiratory compensation is preferred over breathhold.

With respect to water suppression, the CHES and MOIST techniques both showed suppression ratios of approximately 100:1, with MOIST giving slightly better water suppression and more consistent results. However, MOIST is a manufacturer specific variant on the CHES sequence in terms of parameter optimization. Because no statistical difference was measured between the two techniques, the more standard CHES sequence may be able to be substituted where necessary.

Using the optimized protocol proposed in this study, it was possible to get an intersession reproducibility of the MTGC of 6.5% which is in line with the findings of Ith et al.³¹ It should be noted that in that study the creatine signal was used as a reference whereas in our

current study we used the water signal. The reproducibility reported here is also much higher than other studies performed at 1.5 T. For example, it was shown by Felblinger et al that, by using the ECG electrodes to measure the respiratory phase while an optical ECG sensor was used to measure the cardiac cycle, it was possible to get an intersession coefficient of variation of 13%. Szczepaniak et al showed that using a respiratory pressure belt and ECG triggering it was possible to get an intersession coefficient of variation of 17%.³⁰ In van der Meer et al, the coefficient of variation was 17.9% using navigator-based respiratory compensation.⁸ With the optimized protocol proposed in this study the limits of agreement for the Bland Altman analysis lay between -0.15% and $+0.9\%$ compared with -0.14 and $+0.19$ for the study performed by van der Meer et al.

In terms of study limitations, one is that we have only provided optimized parameters for the measurement location in the myocardial septum, which is a relevant region for studying the effects of metabolic syndrome and type 2 diabetes mellitus but not for localized tissue changes such as myocardial infarcts. In this study, the total group of volunteers was relatively large: however, because there were multiple topics of interest the sample size for each individual topic were smaller. We also note that this study was performed on healthy subjects where the efficiency of the navigator is high (around 50%) but some patients tend to have irregular breathing patterns that will most likely result in decreased navigator efficiency and increased scan time.

In conclusion, using the optimized protocol with local power optimization, pencil beam B0 shimming, a cardiac trigger delay of 200 ms, pencil beam navigator-based respiratory compensation, and MOIST water suppression, we were able to achieve an high intra- and intersession reproducibility of the MTGC. The preparation time of the spectroscopy scan was 1 min and 3 s (power optimization 3 s, resonance frequency determination 24 s, and pencil beam B0 shimming 36 s), and the acquisition of the spectra (4 unsuppressed averages and 32 suppressed averages) was 4 min and 24 s with an navigator efficiency of 50%. This resulted in an average total scan time of 5.5 min.

ACKNOWLEDGMENTS

Contract grant sponsor: The Netherlands Organisation for Scientific Research; Contract grant sponsor: the European Research Council. We thank M.J. Versluis and I. Ronen for assistance in data acquisition and analysis, and W.M. Brink for the assistance with the high permittivity pads.

REFERENCES

- Kankaanpää M, Lehto HR, Parkka JP, et al. Myocardial triglyceride content and epicardial fat mass in human obesity: relationship to left ventricular function and serum free fatty acid levels. *J Clin Endocrinol Metab* 2006;91:4689–4695.
- McGavock JM, Lingvay I, Zib I, et al. Cardiac steatosis in diabetes mellitus: a 1H-magnetic resonance spectroscopy study. *Circulation* 2007;116:1170–1175.
- Bizino MB, Hammer S, Lamb HJ. Metabolic imaging of the human heart: clinical application of magnetic resonance spectroscopy. *Heart* 2014;100:881–890.
- Singerman RW, Denison TJ, Wen H, Balaban RS. Simulation of B1 field distribution and intrinsic signal-to-noise in cardiac MRI as a function of static magnetic field. *J Magn Reson* 1997;125:72–83.
- Sung K, Nayak KS. Measurement and characterization of RF nonuniformity over the heart at 3T using body coil transmission. *J Magn Reson Imaging* 2008;27:643–648.
- Greenman RL, Shiroky JE, Mulkern RV, Rofsky NM. Double inversion black-blood fast spin-echo imaging of the human heart: a comparison between 1.5T and 3.0T. *J Magn Reson Imaging* 2003;17:648–655.
- Gutberlet M, Noeske R, Schwinge K, Freyhardt P, Felix R, Niendorf T. Comprehensive cardiac magnetic resonance imaging at 3.0 Tesla: feasibility and implications for clinical applications. *Invest Radiol* 2006; 41:154–167.
- van der Meer RW, Doornbos J, Kozerke S, et al. Metabolic imaging of myocardial triglyceride content: reproducibility of 1H MR spectroscopy with respiratory navigator gating in volunteers. *Radiology* 2007; 245:251–257.
- Rial B, Robson MD, Neubauer S, Schneider JE. Rapid quantification of myocardial lipid content in humans using single breath-hold 1H MRS at 3 Tesla. *Magn Reson Med* 2011;66:619–624.
- Bilet L, van de Weijer T, Hesselink MKC, et al. Exercise-induced modulation of cardiac lipid content in healthy lean young men. *Basic Res Cardiol* 2011;106:307–315.
- Jonker JT, Snel M, Hammer S, et al. Sustained cardiac remodeling after a short-term very low calorie diet in type 2 diabetes mellitus patients. *Int J Cardiovasc Imaging* 2014;30:121–127.
- Clayton DB, Elliott MA, Leigh JS, Lenkinski RE. 1H Spectroscopy without solvent suppression: characterization of signal modulations at short echo times. *J Magn Reson* 2001;153:203–209.
- Schar M, Kozerke S, Boesiger P. Navigator gating and volume tracking for double-triggered cardiac proton spectroscopy at 3 Tesla. *Magn Reson Med* 2004;51:1091–1095.
- Nakae I, Mitsunami K, Omura T, et al. Proton magnetic resonance spectroscopy can detect creatine depletion associated with the progression of heart failure in cardiomyopathy. *J Am Coll Cardiol* 2003; 42:1587–1593.
- Reingold JS, McGavock JM, Kaka S, Tillery T, Victor RG, Szczepaniak LS. Determination of triglyceride in the human myocardium by magnetic resonance spectroscopy: reproducibility and sensitivity of the method. *Am J Physiol Endocrinol Metab* 2005;289:E935–E939.
- Weiss K, Martini N, Boesiger P, Kozerke S. Cardiac proton spectroscopy using large coil arrays. *NMR Biomed* 2013;26:276–284.
- Frahm J, Merboldt KD, Hanicke W. Localized proton spectroscopy using stimulated echoes. *J Magn Reson* (1969) 1987;72:502–508.
- de Heer P, Bizino MB, Versluis MJ, Webb AG, Lamb HJ. Improved cardiac proton magnetic resonance spectroscopy at 3 T using high permittivity pads. *Invest Radiol* 2015;51:134–138.
- Morris GA, Freeman R. Selective excitation in Fourier transform nuclear magnetic resonance. 1978. *J Magn Reson* 2011;213:214–243.
- Haase A, Frahm J, Hanicke W, Matthaei D. 1H NMR chemical shift selective (CHESS) imaging. *Phys Med Biol* 1985;30:341–344.
- Ogg RJ, Kingsley PB, Taylor JS. WET, a T1- and B1-insensitive watersuppression method for in vivo localized 1H NMR spectroscopy. *J Magn Reson B* 1994;104:1–10.
- Murdoch JB, Lampman DA. Beyond WET and DRY: optimized pulses for water suppression. In: *Proceedings of the 12th Annual Meeting of SMRM, New York, 1993.* (abstract 1191).
- Naressi A, Couturier C, Devos JM, et al. Java-based graphical user interface for the MRUI quantitation package. *MAGMA* 2001;12:141–152.
- A°sa Carlsson, Maja Sohlin, Maria Ljungberg, Eva Forssell-Aronsson. The cardiac triggering time delay is decisive for the spectrum quality in cardiac 1H MR Spectroscopy. In: *Proceedings of the 20th Annual Meeting of ISMRM, Melbourne, 2012.* (abstract 1793).
- Sch€ar M, Vonken EJ, Stuber M. Simultaneous B0- and B11-Map acquisition for fast localized shim, frequency, and RF power determination in the heart at 3 T. *Magn Reson Med* 2010;63:419–426.
- Venkatesh BA, Lima JA, Bluemke DA, Lai S, Steenbergen C, Liu CY. MR proton spectroscopy for myocardial lipid deposition quantification: a quantitative comparison between 1.5T and 3T. *J Magn Reson Imaging* 2012;36:1222–1230.

- 27.** Boron WF, Boulpaep EL. Medical physiology. 2nd ed. Philadelphia, PA: Saunders/Elsevier; 2009.
- 28.** Weiss K, Summermatter S, Stoeck CT, Kozerke S. Compensation of signal loss due to cardiac motion in point-resolved spectroscopy of the heart. *Magn Reson Med* 2014;72:1201–1207.
- 29.** Felblinger J, Jung B, Slotboom J, Boesch C, Kreis R. Methods and reproducibility of cardiac/respiratory double-triggered (1)H-MR spectroscopy of the human heart. *Magn Reson Med* 1999;42:903–910.
- 30.** Szczepaniak LS, Dobbins RL, Metzger GJ, et al. Myocardial triglycerides and systolic function in humans: in vivo evaluation by localized proton spectroscopy and cardiac imaging. *Magn Reson Med* 2003;49: 417–423.
- 31.** Ith M, Stettler C, Xu J, Boesch C, Kreis R. Cardiac lipid levels show diurnal changes and long-term variations in healthy human subjects. *NMR Biomed* 2014;27:1285–1292.

DART TWO
CLINICAL
APPLI-
CATIONS
METABOLIC
SYNDROME

**MR OF MULTI-ORGAN
INVOLVEMENT IN THE
METABOLIC SYNDROME**

5 MR OF MULTI-ORGAN INVOLVEMENT IN THE METABOLIC SYNDROME

Adapted from Magnetic Resonance Imaging Clinics of North America. 2015 Feb;23(1):41-58.

Authors

Maurice B. Bizino, MD,¹ Michael L. Sala, MD,¹ Paul de Heer, MSc,² Pieter van der Tol, MSc,¹ Jan W.A. Smit, MD, PhD,³ Andrew G. Webb, PhD,² Albert de Roos, MD, PhD,² Hildo J. Lamb, MD, PhD¹

¹ Department of Radiology, Leiden University Medical Center, Albinusdreef 2, Leiden 2333 ZA, The Netherlands

³ Division of Endocrinology, Department of Medicine, Radboud University Medical Centre, PO Box 9101, 6500 HB, Nijmegen, The Netherlands

² C.J. Gorter Center for High Field MRI, Department of Radiology, Leiden University Medical Center, Albinusdreef 2, Leiden 2333 ZA, The Netherlands

KEY POINTS

- State-of-the-art magnetic resonance (MR) technologies provide whole-body assessment of metabolic syndrome (MetS) pathophysiology and complications.
- MRI and MR spectroscopy image and quantify ectopic lipid accumulation, such as pericardial/perivascular fat, visceral abdominal fat, and fatty infiltration of organs, associated with adverse outcome.
- By using MR elastography, T1-mapping, phosphorus MR spectroscopy, and diffusion-weighted imaging, MR can assist in staging nonalcoholic fatty liver disease.
- Using cardiac MRI, spectroscopy, and mapping techniques, key features of diabetic cardiomyopathy, such as diastolic dysfunction, left ventricular hypertrophy, myocardial steatosis and fibrosis, can be quantified.
- Novel MR techniques, such as magnetization transfer imaging and diffusion tensor imaging, demonstrate microstructural brain damage in MetS.

INTRODUCTION

Epidemiology

About one-third of the United States population of 20 years or older has metabolic syndrome (MetS) and its prevalence increases with advancing age and body mass index,¹ stressing its tight association with the obesity epidemic.

Definition

Diagnosis of MetS requires positive identification of at least 3 out of 5 criteria displayed in Table 1.

Table 1 Diagnosis of MetS

MetS Criteria (NCEP-ATP III Criteria)	Definition
Abdominal obesity: waist circumference	Men > 40 inches Women > 35 inches
Increased plasma triglyceride level	> 150 mg/dL
Decreased plasma HDL level	Men < 40 mg/dL Women < 50 mg/dL
Elevated blood pressure	> 130/85 mm Hg
Increased plasma fasting glucose	> 100 mg/dL

As such, approximately 90% of type 2 diabetes mellitus (DM2) patients have MetS.¹ Patients with MetS are heterogeneous in nature with varying risk of disease and consequently require personalized care, for example, by MR prognosis, in terms of future cardiovascular and cerebrovascular events (Figure 1).²

MRI of Multi-Organ Involvement in the Metabolic Syndrome

MetS is a systemic disease with complex pathophysiology including insulin resistance, atherogenic dyslipidemia, hypertension, ectopic lipid accumulation, low-grade inflammation, prothrombotic state, and fibrosis resulting in end-organ damage.³ MRI and magnetic resonance spectroscopy (MRS) can be used to quantify ectopic lipid accumulation. Importantly, as shown in Figure 2, functional and structural consequences of MetS can be evaluated with MR on a whole body level. In the liver, several techniques — ranging from MRS and water-fat imaging to magnetic resonance elastography (MRE) and T1 mapping — are used to quantify hepatic steatosis and differentiate between stages of nonalcoholic fatty liver disease (NAFLD). In parallel, cardiac MR can quantify myocardial steatosis and associated complications, such as diastolic dysfunction and fibrosis. In the brain, magnetization transfer imaging and diffusion tensor imaging (DTI) can detect microstructural brain damage associated with MetS. The involvement of various other organs ranging from the kidney to pancreas and skeletal muscle can be assessed with MR.

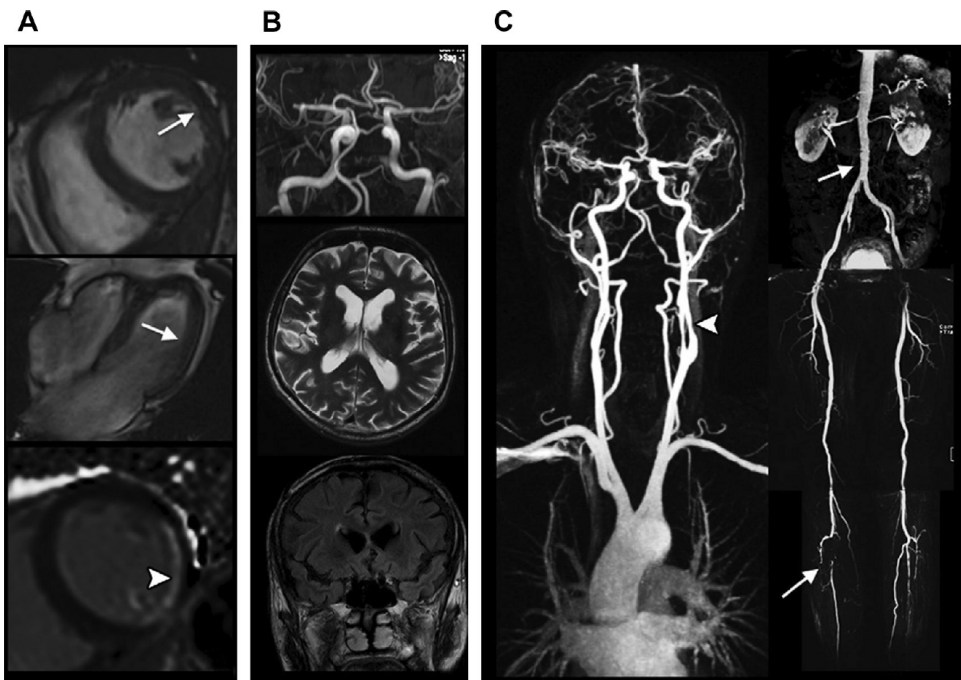


FIGURE 1. Clinical whole-body MR for risk estimation of future cardiovascular events. Images acquired in a 74-year old man with a 21-year history of type 2 diabetes mellitus. **[A]** Cardiac MRI involving cine imaging (top and middle) showing hypokinesia in the anterolateral segment (arrow). The bottom image is a late gadolinium enhanced image displaying subendocardial enhancement (arrowhead) consistent with myocardial infarction. **[B]** Cerebral arteries using time-of-flight angiography (top), an axial T2-weighted brain image (middle) and a coronal fluid-attenuated inversion-recovery image (bottom). These images show no overt brain abnormalities associated with the

metabolic syndrome (MetS). **[C]** Contrast-enhanced MR angiograms of carotid arteries (left) and abdominal and lower extremity arteries (right) with arrowhead and arrows indicating stenosis owing to atherosclerotic disease. Using this 60-minute MR protocol, future cardiac and cerebrovascular events can be predicted in DM patients with higher accuracy compared with clinical characteristics.¹ (From Bamberg F, Parhofer KG, Lochner E, et al. Diabetes mellitus: long-term prognostic value of whole-body MR imaging for the occurrence of cardiac and cerebrovascular events. *Radiology* 2013;269(3):733, with permission.)

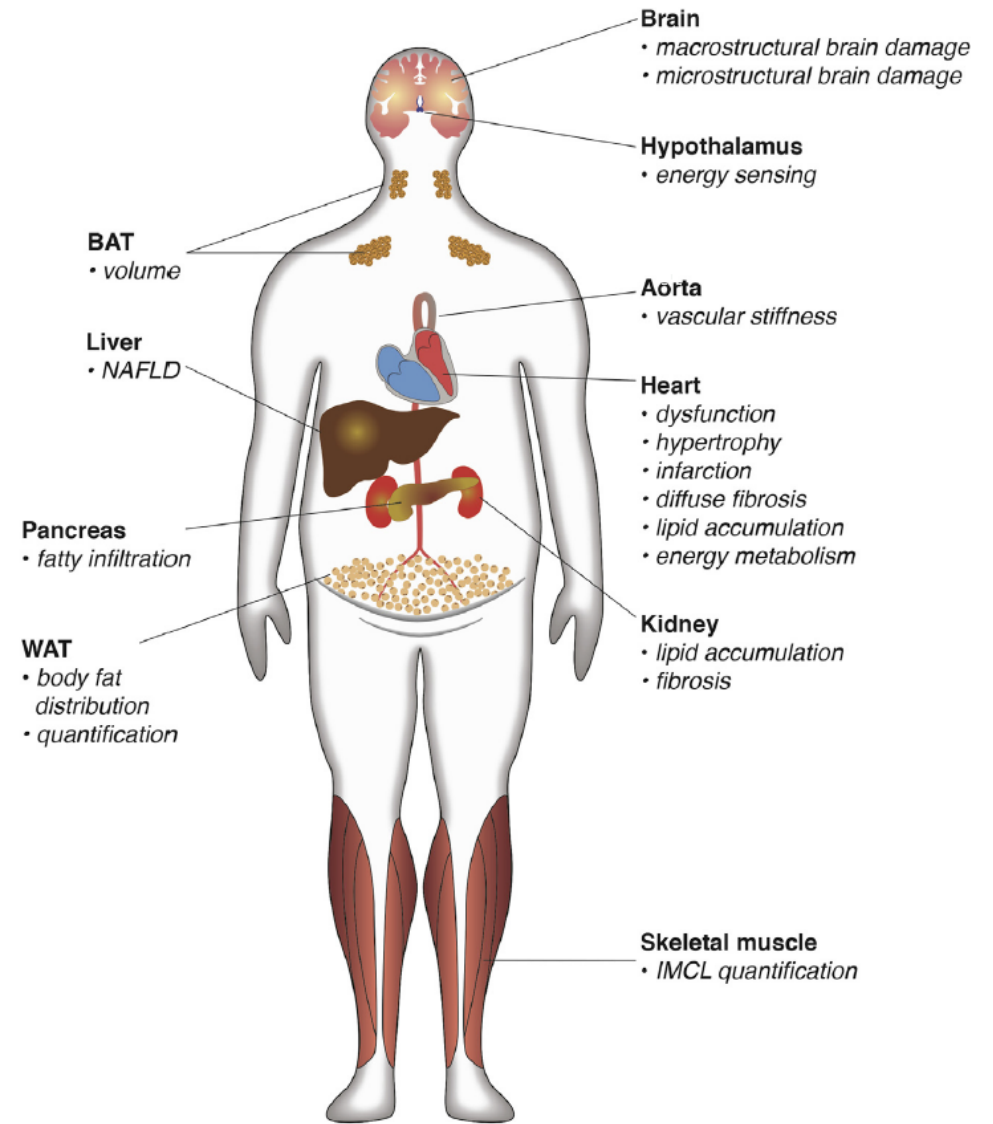


FIGURE 2. Overview of MR assessment of multi-organ involvement in metabolic syndrome. Key features of multiorgan involvement in the metabolic syndrome (MetS) that can be assessed with MR are shown. MRI accurately assesses the distribution of WAT showing an abundance of visceral adipose tissue (VAT) and peri-organ adipose tissue. In contrast, brown adipose tissue volume is diminished in obesity, suggesting that diminished thermogenesis may be involved in the etiology of MetS. Excessive accumulation of triglycerides in the liver, that is, hepatic steatosis, may play a central role in the development of MetS. Hepatic steatosis can progress into nonalcoholic steatohepatitis (NASH), fibrosis, and cirrhosis. Both excessive VAT and hepatic steatosis are strongly linked to

insulin resistance, a key component of MetS. The cardiovascular system can be involved focally (eg, myocardial infarction) or globally (eg, diabetic cardiomyopathy). Cardiac remodeling of the cardiovascular system involves the sequelae of fatty infiltration, inflammation, fibrosis, and ultimately organ failure. Furthermore, brain involvement in MetS is increasingly being studied. In addition to macrostructural changes, such as brain atrophy and cerebral small vessel disease, microstructural changes are important features of MetS brain pathology. Various other organs, such as the kidney, pancreas, and skeletal muscle, undergo pathologic alterations in MetS patients. BAT, brown adipose tissue; WAT, white adipose tissue.

PURPOSE OF REVIEW

This review highlights MR techniques that assess multi-organ involvement in MetS.

ADIPOSE TISSUE**White Adipose Tissue**

Abdominal visceral obesity Ectopic lipid accumulation in white adipose tissue (WAT) predominantly occurs in the visceral abdominal compartment. Visceral white adipocytes can contribute to MetS etiology by secreting excessive amounts of plasma free fatty acids, adipokines, and cytokines. MetS prevalence correlates with waist circumference, reflecting the role of abdominal obesity. However, waist circumference does not differen-

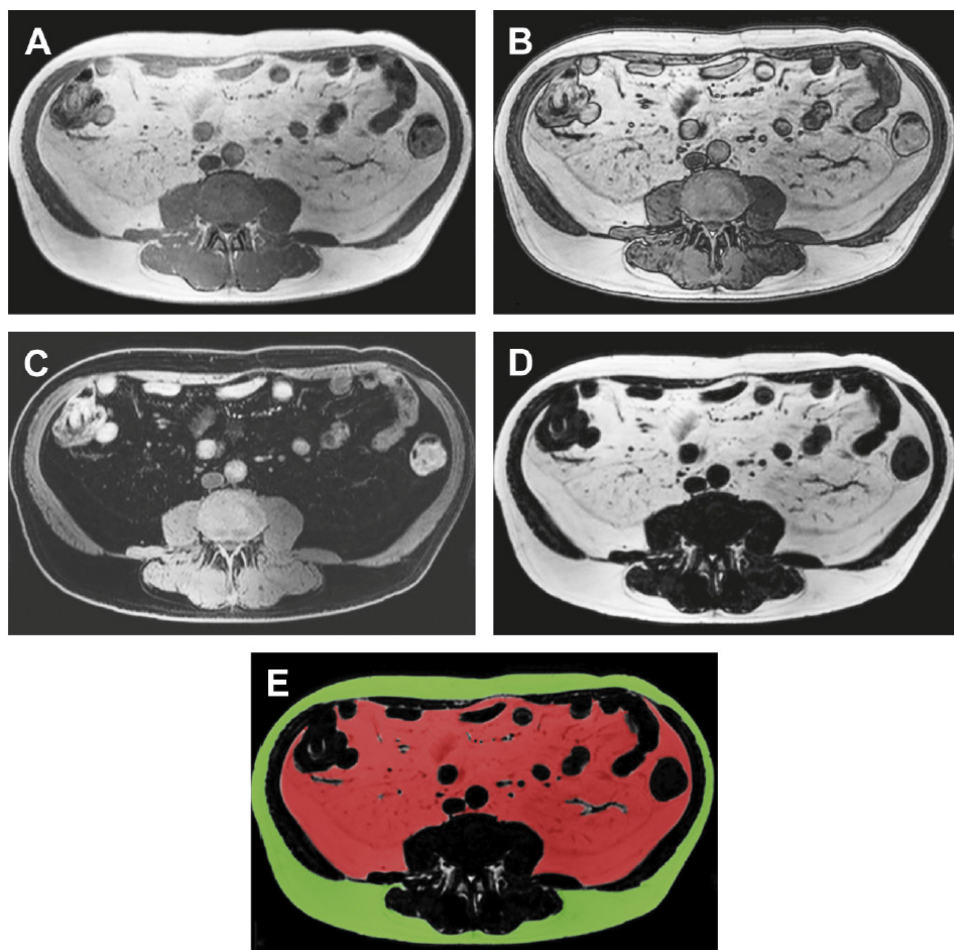


FIGURE 3. Chemical shift imaging of abdominal adipose tissue and subsequent volume quantification. Transverse slice at the level of L5 vertebra acquired with an mDIXON method using 2 echoes, **(A)** 1 in-phase and **(B)** 1 out-of-phase image. From these images, **(C)** a water image and **(D)** fat image can be reconstructed. **(E)** Image post pro-

cessing can be used to semi automatically assess subcutaneous (green) and visceral (red) adipose tissue. This sequence was performed in a patient with longstanding type 2 diabetes mellitus showing relatively large amounts of visceral adipose tissue compared with subcutaneous adipose tissue.

tiating between subcutaneous adipose tissue (SAT) and visceral adipose tissue (VAT). Given that VAT has a stronger association with MetS than SAT, differentiation between SAT and VAT is critical.³ Several MR techniques can be used to reliably quantify SAT and VAT. These include T1-weighted imaging, frequency-selective lipid imaging, and chemical-shift-encoded water-fat imaging, all different methods that can be lumped under the umbrella of water-fat MRI (Figures 3 and 4). An appropriate sequence can be chosen on the basis of local accessibility, available scanning time, and presence of image post-processing expertise. An overview of MR techniques for lipid quantification and their advantages/disadvantages is reviewed by Hu and Kan.⁴

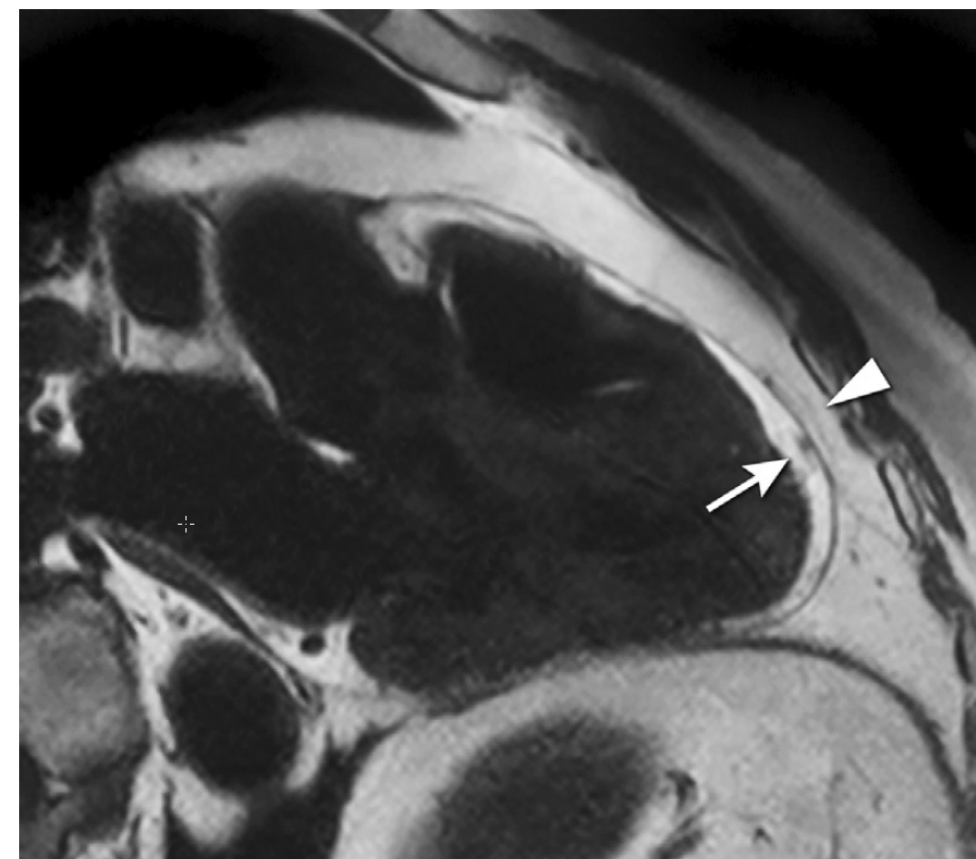


FIGURE 4. Frequency selective imaging of pericardial fat. Three-chamber view acquired with a turbo spin echo sequence with a spectral presaturation with inversion recovery (SPIR) and black blood prepulse sequence during 1 breath-hold at 3 T. This high-resolution sequence enables separate quantification of epicardial (arrow) and paracardial (arrowhead) fat volumes. Note the high paracardial fat mass in this male patient with type 2 diabetes

mellitus. In addition to their different anatomic relation to coronary arteries, epicardial and paracardial fat have a different embryonic origin; epicardial fat has brown adipose tissue characteristics, whereas the paracardial fat does not. Therefore, separate quantification of epicardial and paracardial fat could reveal varying effects on end-organ damage.

Pericardial and perivascular fat

In addition to abdominal VAT, ectopic lipid accumulation around the heart (pericardial fat) and vessels (perivascular fat) is increased in MetS. Pericardial/perivascular fat is physiologically protective in terms of mechanical support and as a source of biochemical substrates, hormones, and cytokines. However, increased pericardial/perivascular lipid accumulation in MetS has been linked with low-grade systemic inflammation, adverse

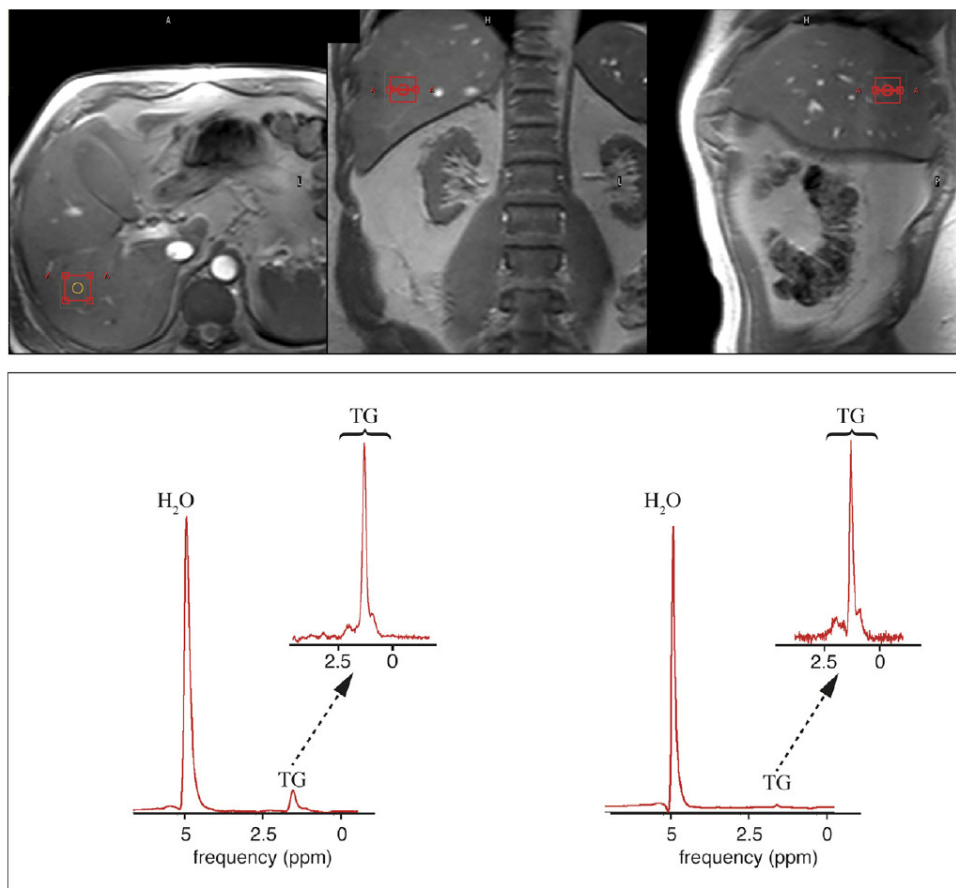


FIGURE 5. Proton magnetic resonance spectroscopy (¹H-MRS) of the liver to quantify hepatic triglyceride content. Voxel planning and examples of proton spectra acquired from the liver at 3 T. ¹H-MRS is based on the fact that different molecules have different chemical environments that translate to small differences in the strength of the magnetic field for the different metabolites. This effect is commonly known as chemical shift. In the recorded spectrum, the difference in magnetic field results in different resonance frequencies, expressed in parts per million (ppm) with respect to that of tetramethylsilane, for the various metabolites. In practice, 1 spectra without water suppression is recorded to use as an internal reference, and 1 or more with water suppression are acquired

for quantification of triglycerides (TG). To be able to measure small metabolite levels, it is necessary to measure a volume much larger than the normal pixel size in MRI. Upper panel, Typical 8-mL voxel for liver ¹H-MRS. Lower panel, Acquired unsuppressed and water-suppressed spectra of an obese (left) and lean (right) volunteer. In liver spectra, TG is mainly represented by 3 different proton moieties, namely, CH₂-CH = CH-CH₂, [-CH₂]ⁿ, and -CH₃. To quantify the fat percentage often the integrals below the [-CH₂]ⁿ and CH₃ peaks are summed and divided by the sum of the integrals of the water and [-CH₂]ⁿ and CH₃ peaks. In this example, the calculated hepatic triglyceride content was 8.26% for the obese subject and 1.24% for the lean subject.

metabolic profile and risk of ischemic heart disease.⁵ Various electrocardiogram-gated MR sequences, including steady-state free precession short axis sequences, fat-selective imaging (see Figure 4), and water-fat MRI, can be used to image pericardial fat and enable volume quantification in a reproducible manner.¹

Brown Adipose Tissue

In contrast to WAT, brown adipose tissue (BAT) volume and activity are diminished in obesity and may play a role in its development. BAT contributes significantly to total resting energy expenditure by dissipating glucose and free fatty acids into heat. The reference method for imaging BAT volume and activity is fluorodeoxyglucose PET-CT after mild cold exposure. The desire for a non-irradiating alternative has led to many MR techniques being evaluated to image BAT. These techniques identify BAT by its higher water fraction compared with WAT. However, MR of BAT is limited by the fact that, in humans, BAT and WAT are not entirely separated anatomically, complicating reliable BAT volume quantification. MRI of BAT activity is still in its infancy, although promising results using T2* imaging have been published recently.⁴

LIVER

Hepatic Steatosis

Ectopic lipid accumulation in the liver, that is, hepatic steatosis, is present in the majority of MetS patients and plays a central role in the pathogenesis of insulin resistance, hyperglycemia, and atherogenic dyslipidemia. The gold standard to determine hepatic steatosis is histology which requires a biopsy. However, several MR techniques can assess hepatic triglyceride (TG) content noninvasively with lower sampling error.¹ Currently, proton MRS (¹H-MRS) is the noninvasive gold standard to quantify hepatic TG content (Figure 5). ¹H-MRS has the best sensitivity for detection of small amounts of fat. A drawback of this technique is the risk of sampling error inherent to quantifying TG content in a small voxel.

Recently, the mDIXON technique using multiple echoes has been shown to enable liver fat quantification (Figure 6). By applying the mDIXON technique, T2* effects caused by the relatively high iron content in the liver can be compensated. The technique is becoming

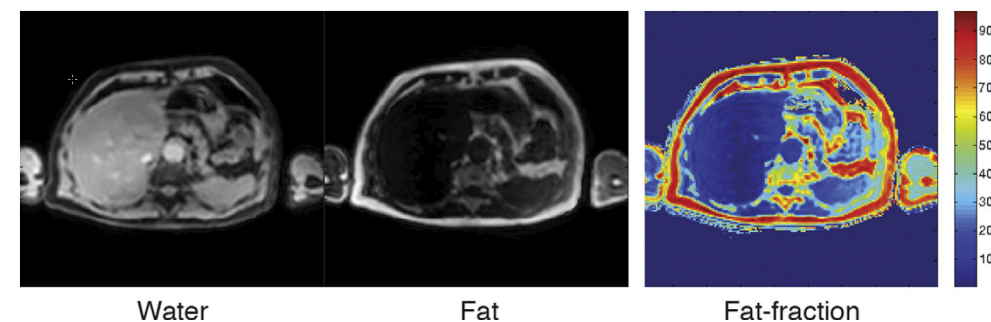


FIGURE 6. DIXON MRI of the liver to quantify hepatic triglyceride content. The left and middle images are the reconstructed water and fat images, respectively. A 6-point DIXON sequence was used with a starting echo time of 0.74 ms and echo spacing of 1 ms. The fat fraction

was calculated on a pixel-by-pixel basis by dividing the fat image by the sum of the water and fat image. For this obese subject, the calculated fat fraction was between 3% and 9%, depending on the location, illustrating the inhomogeneous nature of hepatic steatosis.

increasingly popular because of its advantages of small sampling error (because it is a whole-organ imaging technique) and fast data acquisition.

Multidimensional chemical shift imaging is a multivoxel ^1H -MRS technique that measures a grid of multiple voxels, thus reducing sampling error. The disadvantage of chemical shift imaging is that data acquisition is slow and technically challenging.

Progression of Hepatic Steatosis into Inflammation, Fibrosis, and Cirrhosis

Hepatic steatosis can progress into nonalcoholic steatohepatitis, fibrosis, and ultimately cirrhosis and hepatic failure, a disease spectrum termed NAFLD. MRE, T1 mapping, phosphorus MRS (^{31}P -MRS), and diffusion-weighted imaging (DWI) are the focus of ongoing research to differentiate between NAFLD stages and explore potential advan-

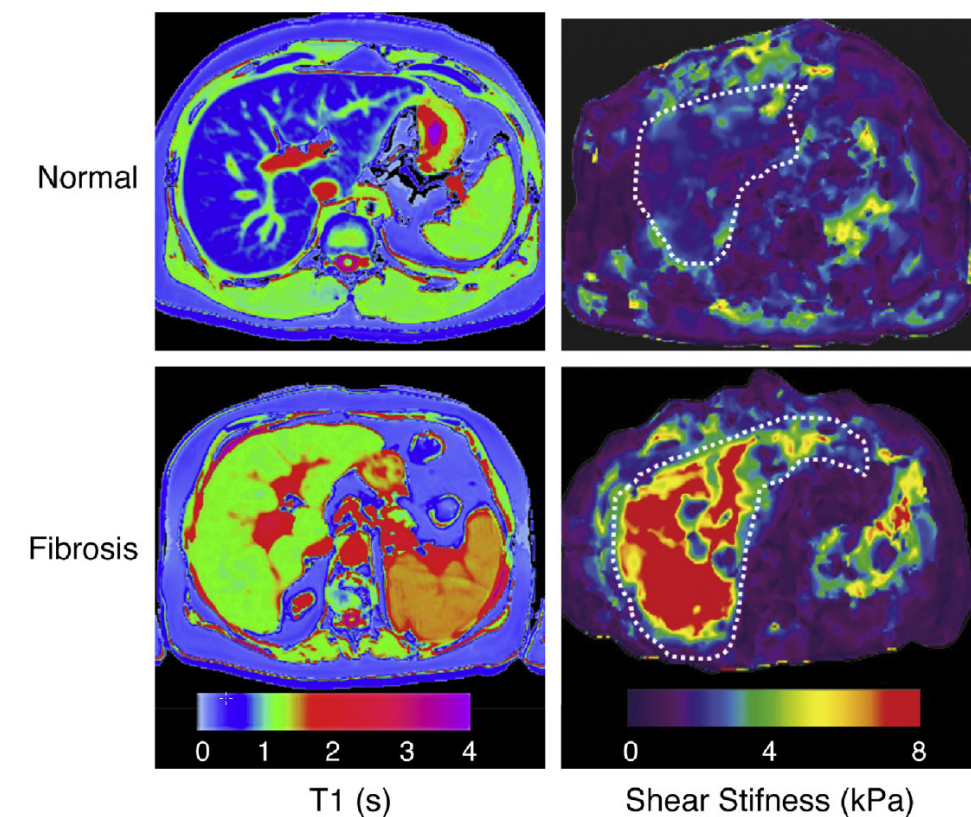


FIGURE 7. Magnetic resonance elastography and T1 mapping: Quantitative imaging of hepatic fibrosis in nonalcoholic fatty liver disease (NAFLD). Examples of T1 mapping (left) and magnetic resonance elastography (MRE; right) in healthy versus fibrotic liver tissue (as assessed by biopsy). T1 maps were acquired with a shortened modified Look-Locker (shMOLL) sequence in a single breath-hold. Increasing T1 values were correlated with increasing degrees of fibrosis. MRE is performed using mechanical waves transmitted by an acoustic pressure driver. Using automated post-processing, data are translated into

quantitative images displaying tissue shear stiffness in kPa. It has been shown that MRE is a useful tool to detect advanced stages of fibrosis. The dotted lines indicate the liver. [From [Left] Banerjee R, Pavlides M, Tunnicliffe EM, et al. Multiparametric magnetic resonance for the non-invasive diagnosis of liver disease. *J Hepatol* 2014;60(1):72, with permission; and [right] Kim D, Kim WR, Talwalkar JA, et al. Advanced fibrosis in nonalcoholic fatty liver disease: noninvasive assessment with MR elastography. *Radiology* 2013;268(2):415, with permission.]

tages compared with histology, that is, lower sampling error and fewer complications.⁶ MRE (Figure 7) is an emerging technique that quantitatively images shear waves in the liver produced by external mechanical waves. A few validation studies have shown MRE's capability of differentiating between stages of NAFLD.⁷

T1 mapping is more readily available than MRE in terms of commercially available imaging sequences. This technique is based on the increased T1 relaxation time of edematous (nonalcoholic steatohepatitis) and fibrotic tissue. In NAFLD, several studies have been performed, showing a strong correlation between increasing T1 and increasing stages of fibrosis (see Figure 7).⁸ In parallel with quantification of extracellular volume (ECV) expansion in cardiac imaging, ECV quantification in the liver is also feasible.⁹ However, validation studies for ECV mapping to quantify liver fibrosis have yet to be published.

^{31}P -MRS can quantify metabolites involved in cell membrane metabolism as well as regulators of fibrosis pathogenesis can be assessed (Figure 8). Additionally, hepatic energy metabolism can be assessed by quantifying high energy phosphates.¹⁰ DWI is a promising technique that measures water movement in extracellular space. Unfortunately, DWI is less reliable in the presence of fat, which limits its use in NAFLD. Future studies must focus on correcting for the influence of fat in order for DWI to become suitable for NAFLD staging.⁶

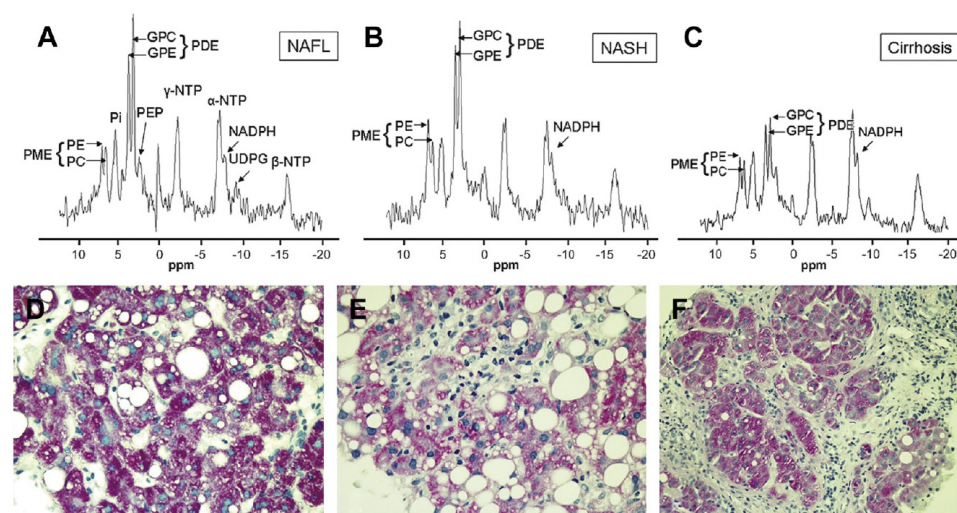


FIGURE 8. Phosphorus magnetic resonance spectroscopy (^{31}P -MRS) of the liver to differentiate between simple steatosis, steatohepatitis, and cirrhosis. Upper panel (A-C). ^{31}P spectra, acquired at 3 T, of simple steatosis (nonalcoholic fatty liver [NAFL]), nonalcoholic steatohepatitis (NASH), and cirrhosis, respectively. This technique quantifies markers of hepatocyte membrane integrity. Corresponding liver biopsy specimens are shown in the lower panel (D-F). The ratio of NADPH/(PME + PDE) was significantly lower in NAFL compared with NASH and cirrhosis, whereas the ratios of PE/(PME + PDE) and GPC/(PME + PDE) were higher in cirrhosis compared with NASH and

NAFL. GPC, glycerophosphocholine; GPE, glycerophosphorylethanolamine; NADPH, nicotinamide adenine dinucleotide phosphate; NTP, nucleoside triphosphate; PC, phosphocholine; PDE, phosphodiester; PE, phosphoethanolamine; PEP, phosphoenolpyruvate; Pi, inorganic phosphate; PME, phosphomonoester; UDPG, uridine diphosphoglucose. [From Sevastianova K, Hakkarainen A, Kotronen A, et al. Nonalcoholic fatty liver disease: detection of elevated nicotinamide adenine dinucleotide phosphate with in vivo 3-T ^{31}P MR spectroscopy with proton decoupling. *Radiology* 2010;256(2):472; with permission.]

HEART

Cardiac MRI (anatomic, functional, angiography, perfusion, late gadolinium enhancement) is an important component in the assessment of a major complication of MetS, namely ischemic heart disease, which is reviewed elsewhere.¹¹ This section covers MR techniques to assess nonischemic remodeling in MetS, that is, “diabetic cardiomyopathy,” which is characterized by diastolic dysfunction, hypertrophy, disrupted cardiac energy metabolism, and ECV expansion related to myocardial fibrosis.

Diastolic Dysfunction

Diastole comprises a combination of active (energy-consuming) relaxation and passive compliance. In MetS, diastolic dysfunction is an early feature and independent predictor of mortality. Diastolic dysfunction is caused by altered myocardial energetics and by diminished ventricular compliance.¹ MR using phase contrast imaging with velocity encoding is a robust technique to quantitatively assess diastolic function (Figure 9). Although the left ventricle (LV) has been the primary focus of research, recent findings show that right ventricular diastolic dysfunction is analogous to LV diastolic dysfunction.¹²

Hypertrophy

LV end-diastolic mass-to-volume ratio is tightly linked to markers of insulin resistance, indicating concentric LV remodeling in MetS.¹¹ Figure 9 shows an example of LV mass quantification with MR.

Cardiac Energy Metabolism

Cardiac energy metabolism is crucial for both systolic and diastolic function. As such, alterations in myocardial energetics may constitute the first step in heart failure pathophysiology.¹³ MRS enables in vivo quantification of myocardial energetics (Figure 10).

Myocardial steatosis

An increased storage of TG in cardiomyocytes is a hallmark of diabetic cardiomyopathy.¹ As shown in animal studies, increased storage of myocardial TG reflects an abundance of toxic lipids that impair cardiomyocyte integrity and function. Myocardial steatosis may be an early sign of diabetic cardiomyopathy, because it is an independent predictor of diastolic dysfunction. Importantly, myocardial steatosis and diastolic dysfunction are reversible, signifying a window of opportunity for therapeutic interventions aimed at preventing overt heart failure.¹ MR is the only modality capable of quantifying myocardial TG content. Figure 11 shows an example of cardiac ¹H-MRS spectroscopy.

High-energy phosphate metabolism: fuel for function

The human heart requires enormous amounts of adenosine triphosphate (ATP) as a primary carrier of chemical energy. As such, the phosphocreatine/ATP ratio is an important indicator of cardiac energy reserve and metabolic efficiency. A decreased ratio is associated with diastolic and systolic dysfunction. The finding that, in DM2 patients with normal cardiac mass and function, the phosphocreatine/ATP ratio was decreased compared with healthy controls, reflects the possibility that disruptions in myocardial energetics might play a role in the pathogenesis of cardiomyopathies.¹³ Figure 12 shows an example of ³¹P-MRS of the heart. Up to now, the use of cardiac ³¹P-MRS has been limited to a research setting in experienced centers because of its complex acquisition.

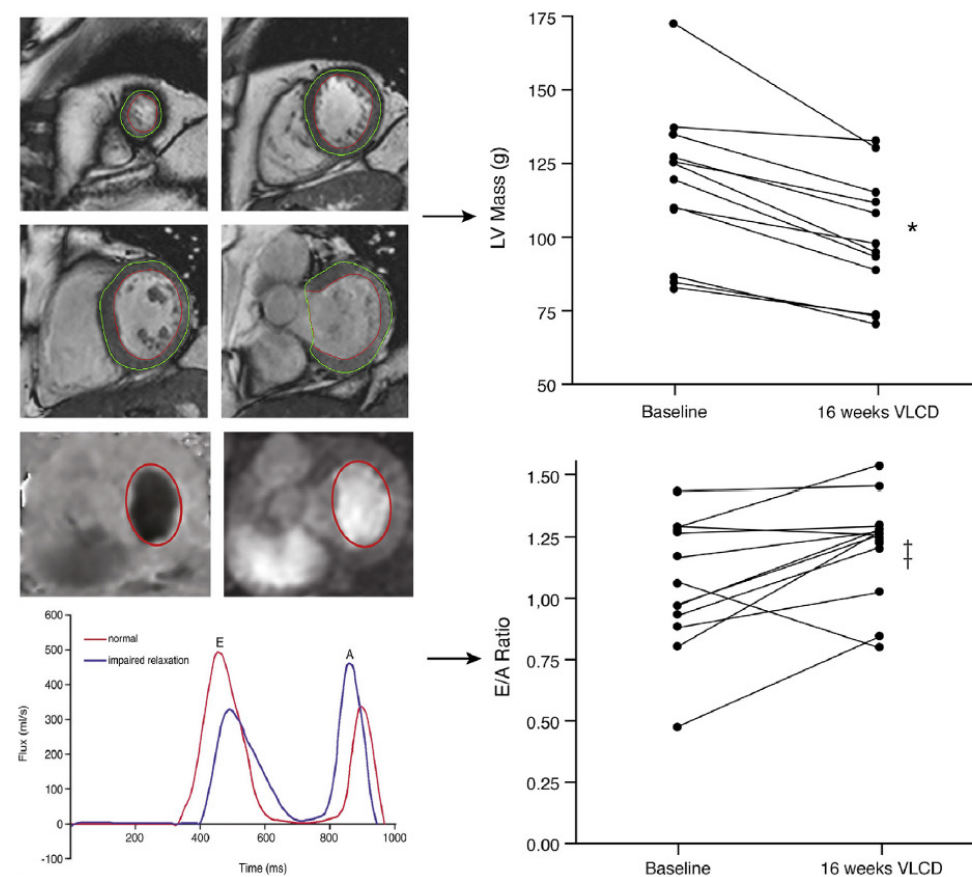


FIGURE 9. Reversible cardiac manifestations in metabolic syndrome: hypertrophy and diastolic dysfunction. MR measures left ventricular (LV) mass and diastolic function reliably and quantitatively, enabling detection of, for example, the effects of nutritional interventions in relatively small study populations. The upper left panel shows manual segmentation of myocardium in end-diastolic short axis images. Using dedicated software, LV mass can be calculated, showing that LV mass diminished in all type 2 diabetes mellitus patients after a 16-week very low-calorie diet (VLCD). Decreased LV mass was tightly linked with improved diastolic function as reflected by an improved E/A ratio (E = early filling phase, A = atrial late filling phase). This parameter can be measured by using phase contrast MR with velocity encoding (lower right panel). By acquiring a 2-dimensional acquisition plane

centered on the atrioventricular valve, a time-velocity or time-flow rate curve can be generated. Recent studies have shown an increased reliability of diastolic function assessment using 3-dimensional 3-directional velocity encoding with retrospective tracking to compensate for valve movement and changing flow direction throughout the cardiac cycle. * P < .001; † P < .05. [From [Left lower panel] van der Meer RW, Lamb HJ, Smit JW, et al. MR imaging evaluation of cardiovascular risk in metabolic syndrome. *Radiology* 2012;264(1):31, with permission; and [Right panel] Hammer S, Snel M, Lamb HJ, et al. Prolonged caloric restriction in obese patients with type 2 diabetes mellitus decreases myocardial triglyceride content and improves myocardial function. *J Am Coll Cardiol* 2008;52(12):1011, with permission.]

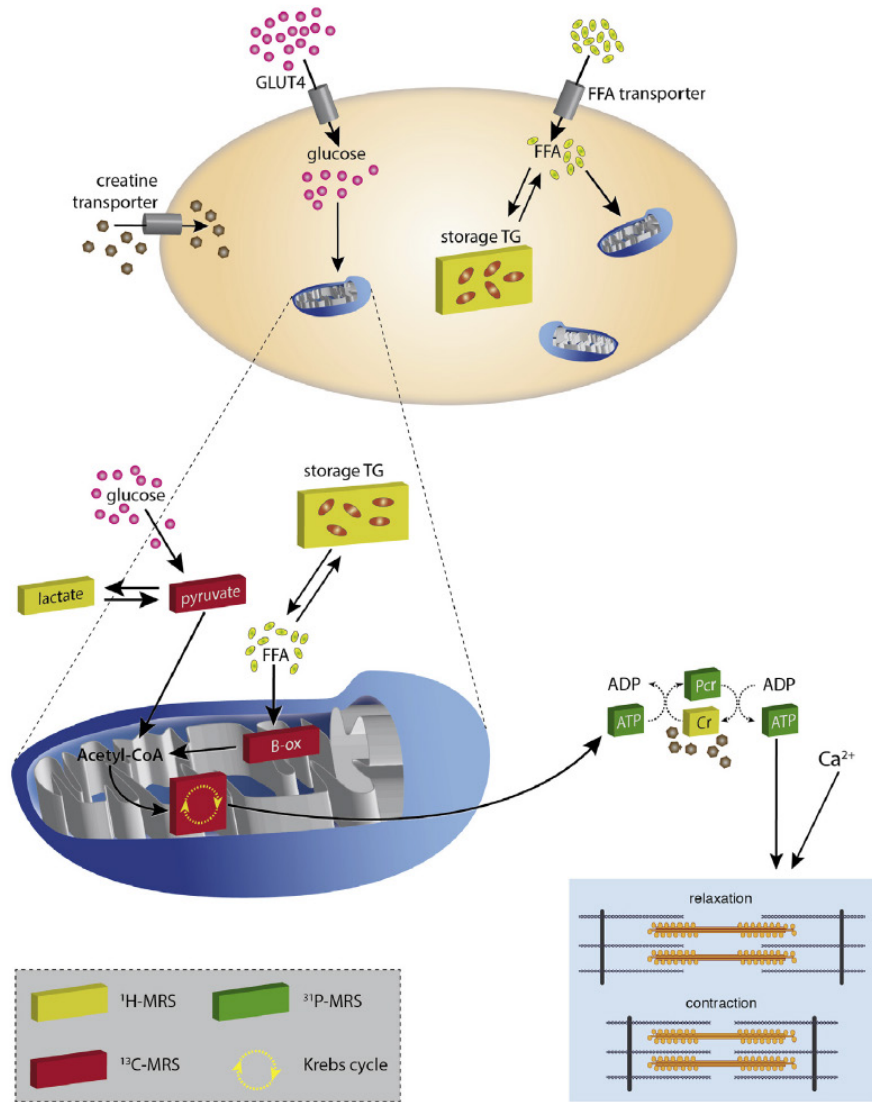


FIGURE 10. MR spectroscopy assessment of cardiac energy metabolism. The cardiomyocyte is represented in orange. FFAs and glucose, in a ratio of 3:1, are the primary sources of chemical energy for the production of ATP, which takes place in the mitochondrion (blue). FFAs are either stored as TGs or oxidized (B-ox) to give acetyl-CoA. Glucose is glycolysed—in the presence of oxygen—to pyruvate, another substrate for acetyl-CoA, which enters the Krebs cycle for oxidative phosphorylation. This process provides energy required to form ATP. In the mitochondrion, ATP and Cr give rise to phosphocreatine (PCr), which diffuses to the myofibril, where it is converted into mechanical energy, under tight control of the Ca²⁺ flux. Note here that both systole and diastole require ATP. The colored boxes (yellow, green, and red) indicate opportuni-

ties for measurement with ¹H, ³¹P and ¹³C MRS, respectively. For ¹H and ³¹P, see also Figures 15 and 16. Cardiac ¹³C-MRS has not yet been performed in humans, but animal studies using hyperpolarized metabolic tracers have shown the feasibility of using cardiac ¹³C-MRS to assess fuel flux (B-ox, Krebs cycle, pyruvate). Acetyl-CoA, acetyl-coenzyme A; ADP, adenosine diphosphate; ATP, adenosine triphosphate; B-ox, β-oxidation; Ca²⁺, ionized calcium; Cr, creatine; FFA, free fatty acid; GLUT4, glucose transporter type 4; PCr, phosphocreatine; TG, triglyceride content. [From Bizino MB, Hammer S, Lamb HJ. Metabolic imaging of the human heart: clinical application of magnetic resonance spectroscopy. *Heart* 2014;100(11):881–90; with permission.]

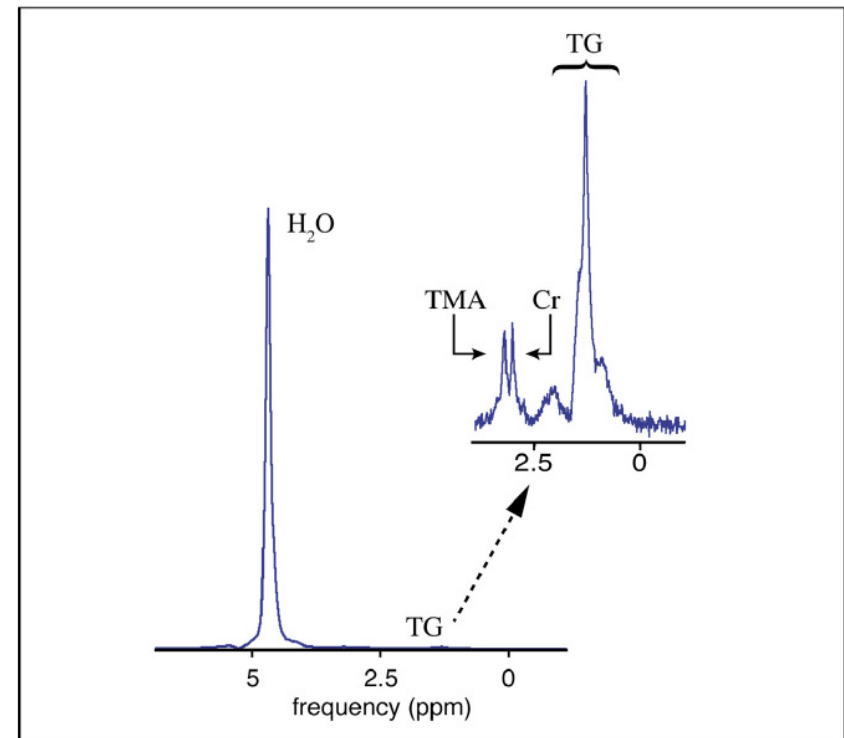
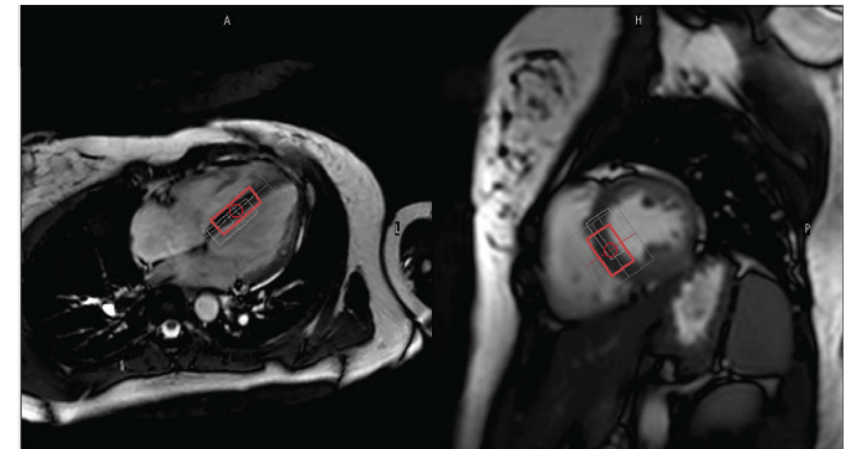


FIGURE 11. Cardiac proton magnetic resonance spectroscopy (¹H-MRS) to quantify myocardial steatosis. Cardiac ¹H-MRS was performed on 1.5 and 3 T MR systems using custom-built detectors. Cardiac ¹H-MRS is subject to motion artifacts owing to contraction and breathing. To overcome these issues, cardiac ¹H-MRS is usually performed with electrocardiographic gating and either breath-holding or free breathing with respiratory motion triggering/compensation. To prevent contamination of pericardial fat, the voxel of interest (VOI) is placed in the

interventricular septum. The most commonly used pulse sequences are stimulated echo acquisition mode (STEAM) and point resolved spectroscopy (PRESS). The low abundance of the various metabolites requires water suppression and acquisition of multiple averages resulting in relatively long scan duration. The water-suppressed spectrum displayed in the lower panel shows signals from creatine (Cr), triglycerides (TG) and trimethyl ammonium (TMA). In this example, 16 non-water-suppressed and 48 water-suppressed averages were acquired at 3 T from a VOI of 15 mL.

Extracellular Volume Expansion

Another hallmark of diabetic cardiomyopathy is ECV expansion caused by collagen deposition, referred to as myocardial fibrosis. Fibrosis is associated with mortality and activation of the renin–angiotensin–aldosterone system¹¹ and can be quantified using a modified Look Locker (MOLLI) or shortened MOLLI sequence.^{14,15} Using these sequences, native T1 mapping and postcontrast T1 mapping can be performed. By combining these images, fractional ECV can be quantified (Figure 13).

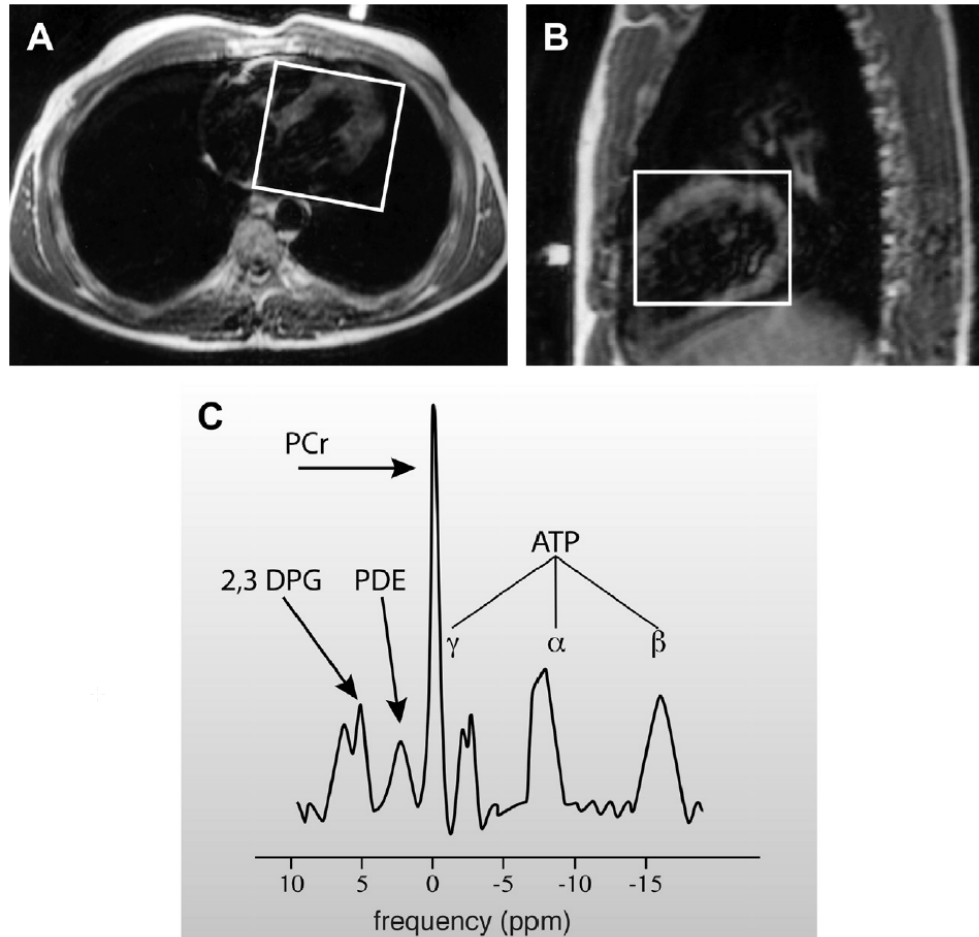


FIGURE 12. Cardiac phosphorus magnetic resonance spectroscopy (³¹P-MRS) to assess high-energy phosphates. Cardiac ³¹P-MRS at 1.5 T is performed by positioning a volume of interest (square box) over almost the entire heart (A, B); eliminating signal contamination from skeletal muscle is essential. The PCr/ATP ratio can be calculated from the spectrum (C) and is an important representation of cardiac energy reserve. In the metabolic

syndrome (MetS), a decreased PCr/ATP ratio has been found before the onset of overt heart failure. ATP, adenosine triphosphate; 2,3 DPG, 2,3-diphosphoglycerate; PCr, phosphocreatine; PDE, phosphodiester; ppm, parts per million. (From Bizino MB, Hammer S, Lamb HJ. Metabolic imaging of the human heart: clinical application of magnetic resonance spectroscopy. Heart 2014;100(11):881–90; with permission.)

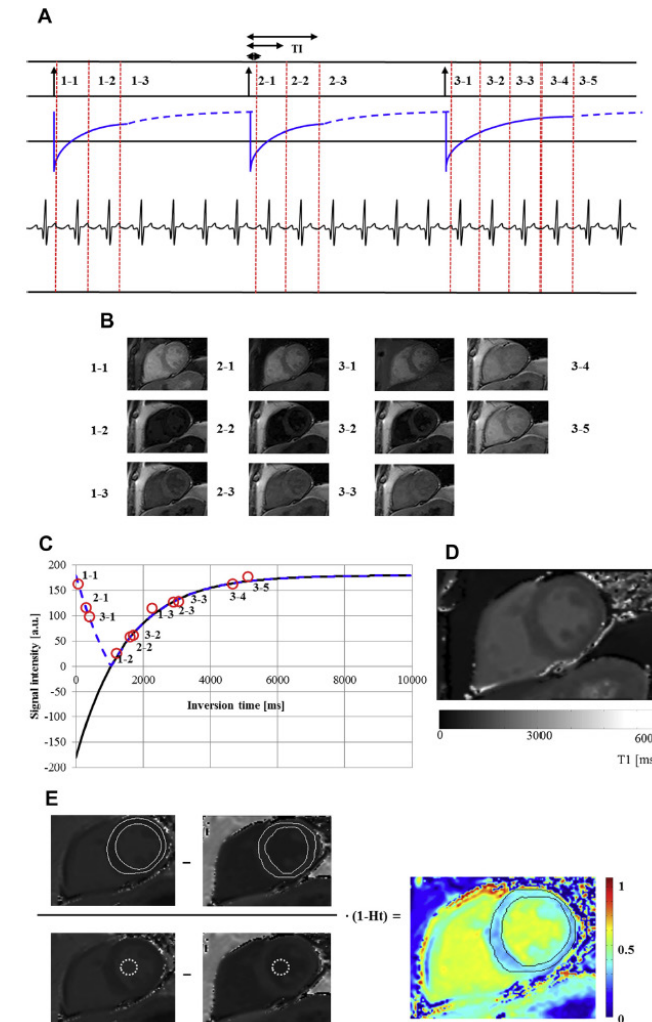


FIGURE 13. MR acquisition and image after processing to evaluate fibrosis in diabetic cardiomyopathy. Modified Look Locker inversion recovery (MOLLI) sequence to determine T1 values of myocardium and subsequent use of precontrast and postcontrast T1 maps to calculate extracellular volume, acquired at 3 T. (A) The MOLLI experiment. This technique consists of 3 consecutive electrocardiogram triggered look locker (LL) experiments, with a three (1), three (2), and five (3) segment single-shot readout. Between each LL experiment, 4 heartbeats are used for magnetization recovery. (B, C) In total, within a 17–heartbeat breath-hold, the longitudinal relaxation curve is sampled at 11 different inversion times. The images are reordered based on increasing inversion time, that is, the time between the inversion pulse and the readout. (D) The T1 map can be calculated by performing voxel wise fitting the signal intensity (SI):

$SI[a.u.] = A - B \times e^{-T1/T1^*}$, $T1 = T1^* \cdot ((B/A) - 1)$. A commonly used variation on the MOLLI method is the shortened MOLLI (ShMOLLI), where only 2 consecutive electrocardiogram-triggered LL experiments are performed with a 5 and 1 single shot read out. (E) The formula used to calculate the extracellular volume fraction (ECV):

$$ECV_{myo} = \frac{R_{1,post,myo} - R_{1,pre,myo}}{R_{1,post,blood} - R_{1,pre,blood}} (1 - H_t)$$

The ECV is determined with a combination of native and postcontrast T1 mapping. The gadolinium-based contrast agent will distribute in the extracellular space of the myocardium. Therefore, a higher concentration of gadolinium indicates a larger ECV, which could indicate more fibrosis. In the example given in this figure, acquired in a 66-year-old type 2 diabetes mellitus patient with myocardial infarction, the average ECV of the myocardium was 0.34, or 34%, compared with 27% in healthy volunteers.

BRAIN INVOLVEMENT IN THE METABOLIC SYNDROME

Brain Structures Involved in Feeding Behavior

Multiple brain structures are functionally involved in the regulation of food intake. Homeostatic regulation of food intake is driven by inputs from the basal ganglia, thalamus, and hippocampus. Interestingly, a recent study found increased amygdalar and hippocampal volumes, as assessed by 3-dimensional T1-weighted MRI, in elderly obese individuals.¹⁶ The finding that these morphometric changes occurred in the amygdala and hippocampus but not in other brain structures that play a role in feeding behavior suggests that cognitive aspects may be of major importance in the regulation of feeding.¹⁶ Additional studies are required to examine the mechanisms behind the observed morphometric changes.

Blood oxygen level-dependent (BOLD) functional MRI is a sensitive marker of brain activation. It has been shown previously that healthy, lean volunteers demonstrated a significant dose dependent decrease of the BOLD signal in the hypothalamus after glucose ingestion.¹⁷ In patients with DM2, hypothalamic neuronal activity is altered, as demonstrated by the absence of a BOLD signal decrease after glucose ingestion.¹⁸ Recently it has been shown that after following a very low-calorie diet for 4 days, the hypothalamus in DM2 patients responds to glucose ingestion similarly to that in healthy subjects.¹⁹ Because the hypothalamus is involved in the control of postprandial metabolism, this may explain the strong metabolic improvement that can be observed in DM2 patients upon caloric restriction.¹⁹ Future studies are needed to elucidate the fundamental mechanisms behind the hypothalamic response to glucose ingestion.

Structural Brain Damage

Although cardiovascular disease is considered to be the main long-term complication of MetS, multiple organs may be affected, including the brain.¹ Risk factors associated with MetS accelerate cerebral small vessel disease, which may result in white matter lesions, cerebral microbleeds, and brain atrophy, as detected by conventional structural MRI.²⁰ Subtle microstructural brain damage may occur in the normal appearing brain tissue in the absence of overt brain abnormalities.²¹

DTI is an MRI technique that is well suited to detect early microstructural changes in normal appearing brain tissue in a number of disease states. Using DTI, Shimoji and colleagues²² recently found that fractional anisotropy (FA) values were lower in MetS subjects relative to control subjects. FA reflects the “coherence” of highly structured tissue, such as axon bundles. Accordingly, lower FA values indicate microstructural brain tissue decline. Regional brain analysis showed that mean FA values of the right inferior fronto-occipital fasciculus were lower in MetS subjects compared with controls subjects.²² The inferior fronto-occipital fasciculus connects all 4 major lobes of the brain and may play an important role in linking all the components of what is commonly referred to as the social brain. The social brain hypothesis may in turn be related to human feeding behavior; several functional MRI studies have detected a correlation between neural activity and eating behavior.

Magnetization transfer imaging is another sensitive MRI technique that can be used to evaluate changes in brain microstructure.²³ Using both DTI and magnetization transfer imaging, Sala and colleagues²¹ recently showed that clustering of risk factors in MetS is associated with evidence of microstructural damage in the gray and white matter as indicated by a decreased magnetization transfer ratio histogram peak height and

increased mean diffusivity. Voxel-wise analysis of cortical gray matter magnetization transfer ratio showed that changes were diffuse and symmetric in both hemispheres. Future longitudinal studies should determine whether these changes evolve into more pronounced structural deterioration or changes in cognition.

Arterial Stiffness

Pulse wave velocity (PWV) is a surrogate marker of vascular stiffness. It is defined as the velocity of the systolic wave front propagating through the vessels (Figure 14) with increased PWV, indicating arterial wall stiffening. MRI enables PWV assessment in different vascular territories, including the aortic arch and the carotid arteries. By using MRI, Roes and colleagues²⁴ found that aortic PWV was increased in MetS subjects. Another study found that aortic PWV is associated with LV mass and lacunar brain infarcts in hypertensive patients.²⁵ These observations may be explained by the concept that aortic stiffening increases exposure of the microcirculation to abnormal physical forces that may lead to endorgan damage.²⁶ MRI enables a comprehensive evaluation of the heart, large vessels, and brain. Future studies should focus on the pathogenesis of end-organ damage in MetS, and evaluate the effect of interventions.

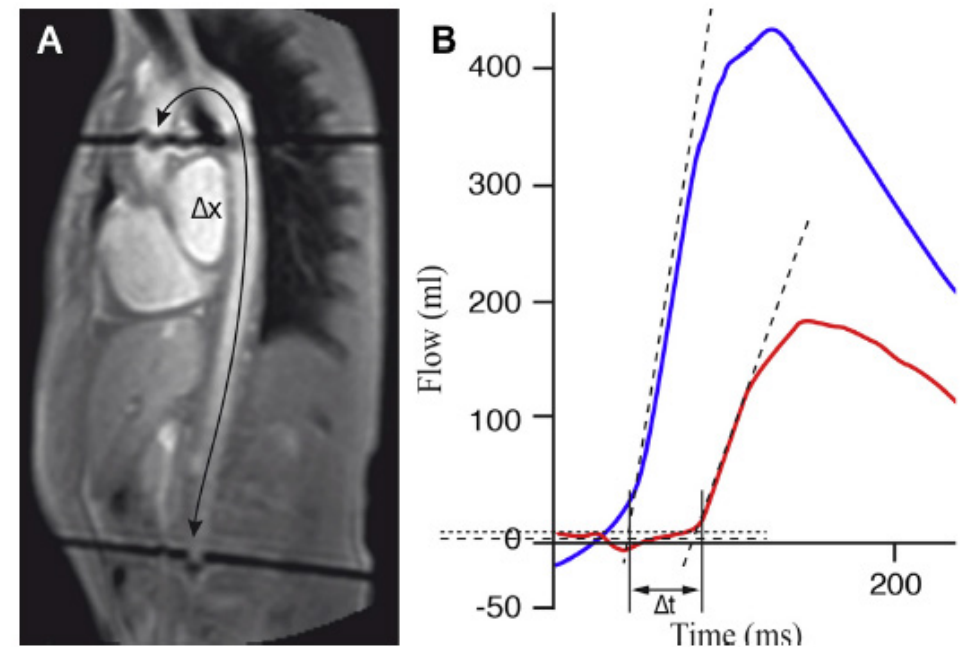


FIGURE 14. MR assessment of arterial stiffness: Pulse wave velocity (PWV). Through-plane velocity encoded MRI assessment of PWV at 1.5 T. **(A)** Sagittal gradient-echo image aligned with the long axis of the aorta shows 2 perpendicular image acquisition planes through the

ascending aorta and abdominal aorta. The path length is indicated by Δx . **(B)** Velocity curves are used to assess the time delay $[\Delta t]$ of the arrival of the proximal [blue curve] and abdominal flow [red curve]. The PWV is calculated as $\Delta x/\Delta t$.

OTHER ORGANS

Kidney

The relationship between MetS and chronic kidney disease (CKD) has become increasingly clear over the past years. Even before the onset of overt diabetes or hypertension, patients have an increased risk of microalbuminuria and renal insufficiency. CKD pathophysiology involves accumulation of toxic lipids, inflammation, neurohumoral factors, and ultimately fibrosis.²⁷ MR assessment of renal TG content (RTGC) was performed in diabetic mice, using chemical shift-selective imaging in combination with BOLD MRI. The results showed that RTGC was inversely correlated with intrarenal oxygenation, suggesting a possible causal link between RTGC and CKD.²⁸ Recently, it has been shown that human RTGC can be assessed reliably with ¹H-MRS (Figure 15).²⁹ Therefore, renal ¹H-MRS provides a tool to study the association between RTGC, MetS, and CKD in humans. As a final common pathway of CKD in MetS, quantitative imaging of renal fibrosis—in parallel with heart and liver—with MR is an obvious next step. To this end, several methods, such as quantitative susceptibility mapping and renal T1 mapping, are promising.³⁰

Pancreas

In parallel with NAFLD, fatty pancreas is associated with visceral obesity and hypertriglyceridemia. This was shown in a population study using iterative decomposition of water and fat with echo asymmetry and least squares estimation (IDEAL), which is a DIXON-based technique with 3 echoes to account for both B₀ and B₁ magnetic field inhomogeneities.³¹ Further studies are needed to clarify the role of fatty pancreas in MetS pathophysiology.

Skeletal Muscle

An increased level of intramyocellular lipids, without a corresponding increase in extramyocellular lipids, is a key feature of peripheral insulin resistance, that may play a role in the increased hepatic steatosis and dyslipidemia, observed in MetS.^{32,33} ¹H-MRS is the only technique sensitive enough to differentiate intramyocellular lipids from extramyocellular lipids (Figure 16). Using ³¹P-MRS, skeletal muscle phosphate-ATP flux can be assessed, thereby providing insight into mitochondrial (dys)function and its relationship with insulin sensitivity.³⁴

SUMMARY

MR is a powerful, noninvasive tool to assess multiorgan involvement in MetS. Key elements of MetS pathophysiology, ranging from ectopic lipid accumulation to end-organ damage of liver, heart, brain, kidney, pancreas, and skeletal muscle, can be evaluated using a multitude of MR techniques. As such, MR has proven its utility with respect to unraveling MetS pathophysiology, as well as monitoring efficacy of therapeutic interventions.

ACKNOWLEDGMENT

The authors thank G. Kracht for figure composition and layout.

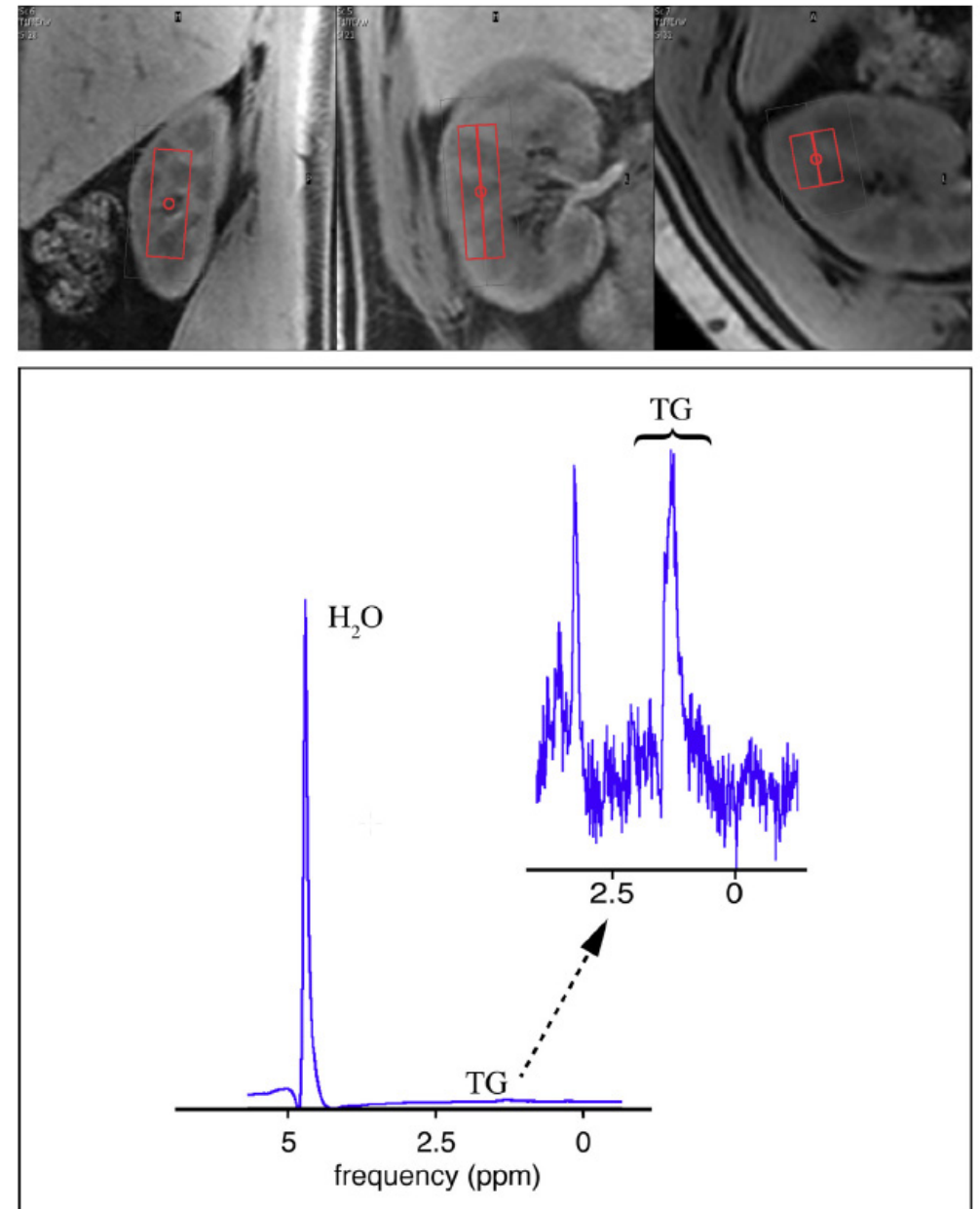


FIGURE 15. Proton magnetic resonance spectroscopy (¹H-MRS) for the evaluation of renal steatosis. MR spectra of the kidney at 3 T. Sixteen water spectra and 64 water-suppressed breath-hold spectra were acquired with a PRESS sequence from a 4-mL voxel. The renal fat fraction in this healthy volunteer was 0.28%. Compared with

liver, lipid levels are lower, and also owing to the smaller organ size, the voxel of interest (VOI) must be smaller; both result in lower signal-to-noise ratio (SNR) in the kidney, requiring greater signal averaging. TG, triglycerides; ppm, parts per million.

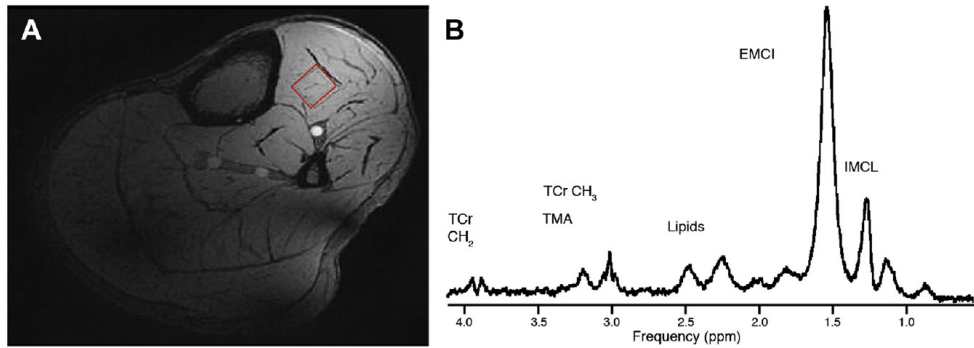


FIGURE 16. Skeletal muscle proton magnetic resonance spectroscopy (^1H -MRS) at 7 T. **(A)** The red box shows the voxel of interest in the tibialis anterior muscle of a healthy volunteer scanned on a 7 T system. **(B)** The corresponding ^1H spectrum shows clear separation of intramyocellular

lipids (IMCL) and extramyocellular lipids (EMCL). IMCL is strongly linked to insulin resistance, whereas EMCL is not. Other peak assignments: tCr, total creatine (CH_2 and CH_3 resonances); TMA, tri-methyl ammonium.

REFERENCES

- van der Meer RW, Lamb HJ, Smit JW, et al. MR imaging evaluation of cardiovascular risk in metabolic syndrome. *Radiology* 2012;264(1):21–37.
- Bamberg F, Parhofer KG, Lochner E, et al. Diabetes mellitus: long-term prognostic value of whole-body MR imaging for the occurrence of cardiac and cerebrovascular events. *Radiology* 2013;269(3):730–7.
- Despres JP, Lemieux I. Abdominal obesity and metabolic syndrome. *Nature* 2006;444(7121):881–7.
- Hu HH, Kan HE. Quantitative proton MR techniques for measuring fat. *NMR Biomed* 2013; 26(12):1609–29.
- Iozzo P. Myocardial, perivascular, and epicardial fat. *Diabetes Care* 2011;34(Suppl 2):S371–9.
- Cobbold JF, Patel D, Taylor-Robinson SD. Assessment of inflammation and fibrosis in non-alcoholic fatty liver disease by imaging-based techniques. *J Gastroenterol Hepatol* 2012;27(8):1281–92.
- Kim D, Kim WR, Talwalkar JA, et al. Advanced fibrosis in nonalcoholic fatty liver disease: noninvasive assessment with MR elastography. *Radiology* 2013;268(2):411–9.
- Banerjee R, Pavlides M, Tunnicliffe EM, et al. Multiparametric magnetic resonance for the noninvasive diagnosis of liver disease. *J Hepatol* 2014; 60(1):69–77.
- Bandula S, Banyersad SM, Sado D, et al. Measurement of Tissue interstitial volume in healthy patients and those with amyloidosis with equilibrium contrast-enhanced MR imaging. *Radiology* 2013; 268(3):858–64.
- Sebastianova K, Hakkarainen A, Kotronen A, et al. Nonalcoholic fatty liver disease: detection of elevated nicotinamide adenine dinucleotide phosphate with in vivo 3-T ^31P MR spectroscopy with proton decoupling. *Radiology* 2010;256(2):466–73.
- Shah RV, Abbasi SA, Kwong RY. Role of cardiac MRI in diabetes. *Curr Cardiol Rep* 2014;16(2):449.
- Widya RL, van der Meer RW, Smit JW, et al. Right ventricular involvement in diabetic cardiomyopathy. *Diabetes Care* 2013;36(2):457–62.
- Bizino MB, Hammer S, Lamb HJ. Metabolic imaging of the human heart: clinical application of magnetic resonance spectroscopy. *Heart* 2014; 100(11):881–90.
- Messroghli DR, Radjenovic A, Kozierke S, et al. Modified look-locker inversion recovery (MOLLI) for high-resolution T1 mapping of the heart. *Magn Reson Med* 2004;52(1):141–6.
- Piechnik SK, Ferreira VM, Dall'Armellina E, et al. Shortened modified look-locker inversion recovery (ShMOLLI) for clinical myocardial T1-mapping at 1.5 and 3 T within a 9 heartbeat breathhold. *J Cardiovasc Magn Reson* 2010;12:69.
- Widya RL, de Roos A, Trompet S, et al. Increased amygdalar and hippocampal volumes in elderly obese individuals with or at risk of cardiovascular disease. *Am J Clin Nutr* 2011;93(6):1190–5.
- Smeets PA, de GC, Stafleu A, et al. Functional MRI of human hypothalamic responses following glucose ingestion. *Neuroimage* 2005;24(2):363–8.
- Vidarsdottir S, Smeets PA, Eichelsheim DL, et al. Glucose ingestion fails to inhibit hypothalamic neuronal activity in patients with type 2 diabetes. *Diabetes* 2007;56(10):2547–50.
- Teeuwisse WM, Widya RL, Paulides M, et al. Short-term caloric restriction normalizes hypothalamic neuronal responsiveness to glucose ingestion in patients with type 2 diabetes. *Diabetes* 2012;61(12):3255–9.
- Kloppenborg RP, Nederkoorn PJ, Grool AM, et al. Cerebral small-vessel disease and progression of brain atrophy: the SMART-MR study. *Neurology* 2012;79(20):2029–36.
- Sala M, de RA, Berg AV, et al. Microstructural brain tissue damage in metabolic syndrome. *Diabetes Care* 2014;37(2):493–500.
- Shimoji K, Abe O, Uka T, et al. White matter alteration in metabolic syndrome: diffusion tensor analysis. *Diabetes Care* 2013;36(3):696–700.
- Seiler S, Cavalieri M, Schmidt R. Vascular cognitive impairment - an ill-defined concept with the need to define its vascular component. *J Neurol Sci* 2012;322(1–2):11–6.
- Roes SD, Alizadeh DR, Westenberg JJ, et al. Assessment of aortic pulse wave velocity and cardiac diastolic function in subjects with and without the metabolic syndrome: HDL cholesterol is independently associated with cardiovascular function. *Diabetes Care* 2008;31(7):1442–4.
- Brandts A, van Elderen SG, Westenberg JJ, et al. Association of aortic arch pulse wave velocity with left ventricular mass and lacunar brain infarcts in hypertensive patients: assessment with MR imaging. *Radiology* 2009;253(3):681–8.
- Mitchell GF, van Buchem MA, Sigurdsson S, et al. Arterial stiffness, pressure and flow pulsatility and brain structure and function: the age, gene/environment susceptibility - Reykjavik study. *Brain* 2011; 134(Pt 11):3398–407.

27. Singh AK, Kari JA. Metabolic syndrome and chronic kidney disease. *Curr Opin Nephrol Hypertens* 2013; 22(2):198–203.
28. Peng XG, Bai YY, Fang F, et al. Renal lipids and oxygenation in diabetic mice: noninvasive quantification with MR imaging. *Radiology* 2013;269(3): 748–57.
29. Hammer S, de Vries AP, de Heer P, et al. Metabolic imaging of human kidney triglyceride content: reproducibility of proton magnetic resonance spectroscopy. *PLoS One* 2013;8(4):e62209.
30. Xie L, Sparks MA, Li W, et al. Quantitative susceptibility mapping of kidney inflammation and fibrosis in type 1 angiotensin receptor-deficient mice. *NMR Biomed* 2013;26(12):1853–63.
31. Wong VW, Wong GL, Yeung DK, et al. Fatty pancreas, insulin resistance, and beta-cell function: a population study using fat-water magnetic resonance imaging. *Am J Gastroenterol* 2014;109(4): 589–97.
32. Flannery C, Dufour S, Rabol R, et al. Skeletal muscle insulin resistance promotes increased hepatic de novo lipogenesis, hyperlipidemia, and hepatic steatosis in the elderly. *Diabetes* 2012;61(11):2711–7.
33. Boesch C, Machann J, Vermathen P, et al. Role of proton MR for the study of muscle lipid metabolism. *NMR Biomed* 2006;19:968–88.
34. Kemp GJ, Brindle KM. What do magnetic resonance-based measurements of Pi – ATP flux tell us about skeletal muscle metabolism. *Heart Fail Rev.* 2013;18:657–668.

**METABOLIC IMAGING
OF HUMAN KIDNEY
TRIGLYCERIDE
CONTENT:
REPRODUCIBILITY OF
PROTON MAGNETIC
RESONANCE
SPECTROSCOPY**

6 METABOLIC IMAGING OF HUMAN KIDNEY TRIGLYCERIDE CONTENT: REPRODUCIBILITY OF PROTON MAGNETIC RESONANCE SPECTROSCOPY

Adapted from PLOS ONE. 2013 Apr 19;8(4).

Authors

Sebastiaan Hammer¹, Aiko P. J. de Vries², Paul de Heer^{1,2}, Maurice B. Bizino^{1,3}, Ron Wolterbeek⁴, Ton J. Rabelink², Joost Doornbos¹, Hildo J. Lamb¹

¹ Department of Radiology, Leiden University Medical Center (Leiden University), Leiden, The Netherlands

³ Department of Endocrinology, Leiden University Medical Center, Leiden, The Netherlands

² Department of Nephrology, Leiden University Medical Center, Leiden, The Netherlands

⁴ Department of Medical Statistics, Leiden University Medical Center, Leiden, The Netherlands

ABSTRACT

Objective:

To assess the feasibility of renal proton magnetic resonance spectroscopy for quantification of triglyceride content and to compare spectral quality and reproducibility without and with respiratory motion compensation in vivo.

Materials and Methods:

The Institutional Review Board of our institution approved the study protocol, and written informed consent was obtained. After technical optimization, a total of 20 healthy volunteers underwent renal proton magnetic resonance spectroscopy of the renal cortex both without and with respiratory motion compensation and volume tracking. After the first session the subjects were repositioned and the protocol was repeated to assess reproducibility. Spectral quality (linewidth of the water signal) and triglyceride content were quantified. Bland-Altman analyses and a test by Pitman were performed.

Results:

Linewidth changed from 11.5 ± 0.4 Hz to 10.7 ± 0.4 Hz (all data pooled, $p < 0.05$), without and with respiratory motion compensation respectively. Mean % triglyceride content in the first and second session without respiratory motion compensation were respectively $0.58 \pm 0.12\%$ and $0.51 \pm 0.14\%$ ($P = \text{NS}$). Mean % triglyceride content in the first and second session with respiratory motion compensation were respectively $0.44 \pm 0.10\%$ and $0.43 \pm 0.10\%$ ($P = \text{NS}$ between sessions and $P = \text{NS}$ compared to measurements with respiratory motion compensation). Bland-Altman analyses showed narrower limits of agreement and a significant difference in the correlated variances (correlation of -0.59 , $P < 0.05$).

Conclusion:

Metabolic imaging of the human kidney using renal proton magnetic resonance spectroscopy is a feasible tool to assess cortical triglyceride content in humans in vivo and the use of respiratory motion compensation significantly improves spectral quality and reproducibility. Therefore, respiratory motion compensation seems a necessity for metabolic imaging of renal triglyceride content in vivo.

INTRODUCTION

The global increase in chronic kidney disease (CKD) parallels the obesity epidemic.¹ Obese subjects have a weight-dependent 2- to 7-fold increased risk in progression of CKD irrespective of the underlying cause.^{2,3} Surprisingly, little is known on how obesity can progress or even lead to renal disease. Obesity is associated with a secondary form of focal segmental glomerulosclerosis, coined obesity-related glomerulopathy (ORG) when no other primary renal disease appears present. A recent study found a ten-fold increased incidence of ORG in native kidney biopsies between 1986–2000, suggesting a newly emerging epidemic.⁴ Accumulating evidence from experimental and scarce limited human biopsy studies link ectopic lipid deposition in the kidney (renal adiposity or fatty kidney) to the development of ORG.^{5–8} Unfortunately, clinical research on renal adiposity is hampered by the fact that it is considered unethical to biopsy human kidneys (repeatedly) without clear evidence of (late) renal disease.

Proton magnetic resonance spectroscopy (¹H-MRS) is a tool for metabolic imaging to non-invasively assess triglyceride (TG) content in different human tissues in vivo, including the heart, liver and skeletal muscle.^{9,10} Spectral quality and reproducibility of e.g. cardiac ¹H-MRS are influenced by respiratory motion.¹¹ Compensation for respiratory motion using navigator gating and volume tracking improves myocardial spectral quality and reproducibility.^{11,12} However, ¹H-MRS for detection of renal TG content has never been performed to our knowledge. Furthermore, the possible effects of respiratory motion on reproducibility are unknown.

The purpose of this study was to assess the feasibility of renal ¹H-MRS and to compare spectral quality and reproducibility without and with respiratory motion compensation in vivo. The results show that ¹H-MRS is a feasible tool to assess cortical TG content in humans in vivo and use of respiratory motion compensation with navigator echoes significantly improves spectral quality and reproducibility.

MATERIALS AND METHODS

Ethics statement

The Institutional Review Board of our institution (Leiden University Medical Center) approved the study protocol, and written informed consent was obtained from all participants. The research was conducted according to the principles expressed in the Declaration of Helsinki.

Study design

A total of 37 healthy volunteers without a history of renal or cardiovascular disease, were prospectively included in the study. ¹H-MRS of the renal cortex was performed at rest. ¹H-MRS with and without respiratory motion compensation and volume tracking was performed during one session with the same parameters, without changing the position of the voxel. Thereafter, the volunteer was removed from the scanner. The volunteer was repositioned in the scanner and planning and ¹H-MRS was repeated with and without respiratory navigator gating and volume tracking. The coil position was not marked.

MR Technique

Measurements were performed at 1.5 T (Gyrosan ACS/NT15; Philips, Best, the Netherlands) using a 17 cm diameter circular surface coil, centered at the level of the left kidney. Scout images of the left kidney were made in a coronal, sagittal and axial orientation to verify coil position, Figure 1 (single-shot TSE sequence, shortest TR, TE = 80 ms, slice thickness = 3 mm, no gap).

¹H-MR Spectroscopic Technique

Renal ¹H-MR spectra were obtained from the cortex of the left kidney. The built-in body coil was used for RF transmission and the surface coil was used for signal reception. A 4 ml voxel (40x10x10 mm³ [height x length x width]) was positioned in the cortex on the scout images avoiding contamination from perirenal and renal sinus fat (Figure 1). In a subset of volunteers spectra with deliberate voxel misplacement with localization in the renal sinus were also measured. A point resolved spectroscopy sequence was used to acquire single voxel MR spectroscopic data. Per acquisition 1024 data points were



FIGURE 1. Planning of the proton magnetic resonance spectroscopy voxel. Placement of the proton magnetic resonance spectroscopy (¹H-MRS) voxel (40x10x10 mm), avoiding contamination with intra-abdominal/perirenal

and renal sinus fat. Coronal (A), sagittal (B) and transverse (C) scout images (single shot turbo spin echo). doi:10.1371/journal.pone.0062209.g001

acquired using 1000 Hz spectral bandwidth and averaged over 64 acquisitions. A TR of 3000 ms was chosen to approach complete relaxation of the TG signals. For respiratory motion compensation a pencil beam navigator was positioned on the right hemi-diaphragm.¹²⁻¹⁴ A two-dimensional spatially selective RF pulse for pencil beam-shaped excitation was used. A pencil beam of 25 mm diameter was selected. Respiratory navigator gated spectroscopic data were accepted during in a predefined acceptance window of 5 mm diaphragm displacement in end-expiration. Residual motion was compensated with motion tracking.

Preparation phases, including F0 determination, gradient shimming and water suppression were performed using respiratory motion compensation. To generate an internal reference, a spectrum without water suppression with a repetition time of 10 s and 4 averages was obtained, without changing any other parameter. Total acquisition time for both a water suppressed and water unsuppressed spectrum, including (re)positioning of the patient, shimming, and parameter adjustment for water suppression, was on average 20 min.

Spectral Quantification

¹H-MR spectroscopic data were fitted in the time domain, directly on free-induction decays using Java-based MR user interface software (jMRUI version 4.0; developed by A. van den Boogaart, Katholieke Universiteit Leuven, Leuven, Belgium).¹⁵ Data were analyzed within consensus by two authors with 7 (S.H.) and 20 (H.L.) years of experience. The Hankel-Lanczos filter (single-variable decomposition method) was used to remove residual water signal from spectra acquired with water suppression. Renal cortical TG signal amplitudes were analyzed automatically by using the frequency estimates for renal lipids, described with the assumption of Gaussian line shapes at 0.9, 1.3, and 2.1 ppm. Prior knowledge was incorporated into the fitting.¹⁶⁻¹⁸ Fixed frequencies for TG peaks were used, line widths and amplitudes were unconstrained. The zero-order phase correction was estimated by using the AMARES algorithm. The water signal peak at 4.7 ppm was quantified and its linewidth was estimated by using a Lorentzian line shape in the AMARES algorithm. The percentage of myocardial TG relative to water (%TG) was calculated as area under TG peak/area under water peak x 100. Spectral quality was quantified as the full width at half maximum (FWHM) of the water resonance in the unsuppressed spectra with, and without respiratory motion compensation.

Statistical Analysis

FWHM was quantified using a paired T-Test for all data pooled (linewidth). Mean coefficients of variations for both ungated and gated measurements were quantified separately. To compare reproducibility of renal %TG with and without respiratory navigator gating and volume tracking, the intra-class correlation coefficients (ICC, two-way mixed, absolute agreement) were calculated by using a mixed effects ANOVA (with patients as random factor) for both conditions separately. Moreover, Bland-Altman plots were constructed. A test by Pitman was performed to analyze whether the correlated variances of the two techniques differed.¹⁹ P < 0.05 was considered significant. Means ± standard errors (SE) are displayed. Statistical analyses were performed by using SPSS, version 20.01.

RESULTS

Participants

Since the start of the technique developmental phase, ^1H -MRS of the kidney was performed prospectively in 37 consecutive healthy volunteers without a history of renal or cardiovascular disease. A total of 17 volunteers were excluded from analyses during this initial phase: A) due to technical optimization and time constraints the scanning could not be completed [9 subjects], B) erroneous navigator [2 subjects] and C) impossible fitting procedure of all acquired spectra [6 subjects]). Based on these initial scans, the optimal technical protocol was defined.

In 20 volunteers the complete scanning protocol was completed (12 males, mean age \pm SD 26.3 ± 8.3 yrs, range 20.3 – 57.9 yrs). In 4 of these volunteers the spectra acquired without respiratory motion compensation were not used for analysis, due to their degraded quality.

The linewidth of the unsuppressed water signal changed from 11.5 ± 0.4 Hz to 10.7 ± 0.4 Hz (all data pooled, $p < 0.05$), without and with respiratory navigator gating respectively. A typical example of a ^1H -MR spectrum of renal cortical TG content is shown in Figure 2. An example of a spectrum obtained in the region of the renal sinus shows an expectedly high percentage of TG content (Figure 3).

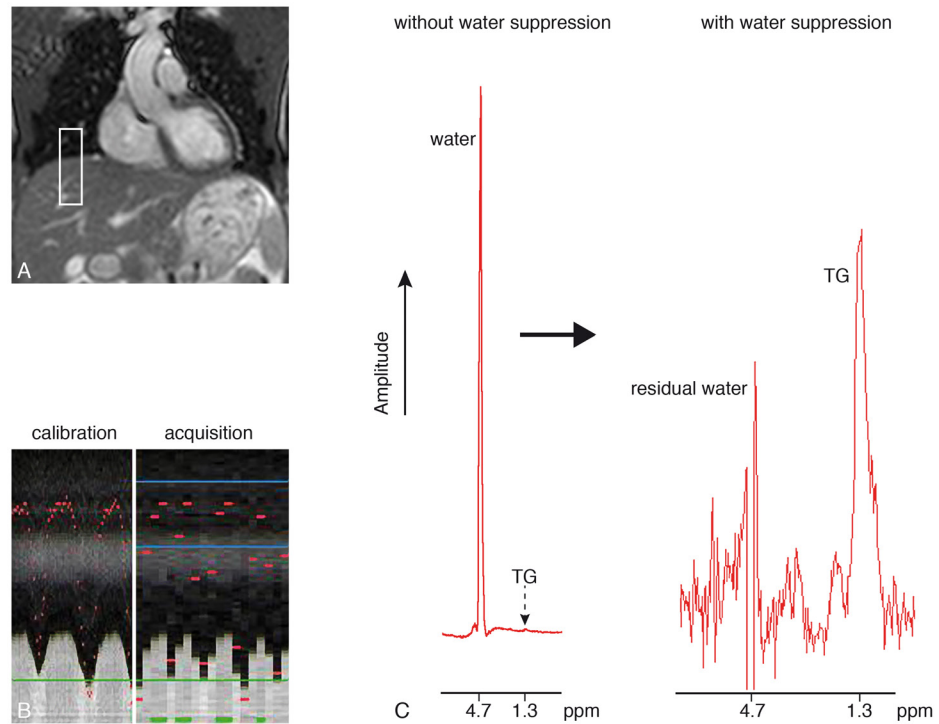


FIGURE 2. Planning of the respiratory navigator. The navigator pencil beam is positioned on the right hemidiaphragm (panel A). Panel B shows the calibration phase with a high temporal resolution, in which the lung-liver interface is detected during free breathing, as well as the acquisition phase showing the accepted measurements in

the predefined end-expiratory window (lower temporal resolution). Panel C shows a typical non-suppressed (left) and a suppressed (right) localized renal proton spectrum, obtained using respiratory motion compensation and gating. doi:10.1371/journal.pone.0062209.g002

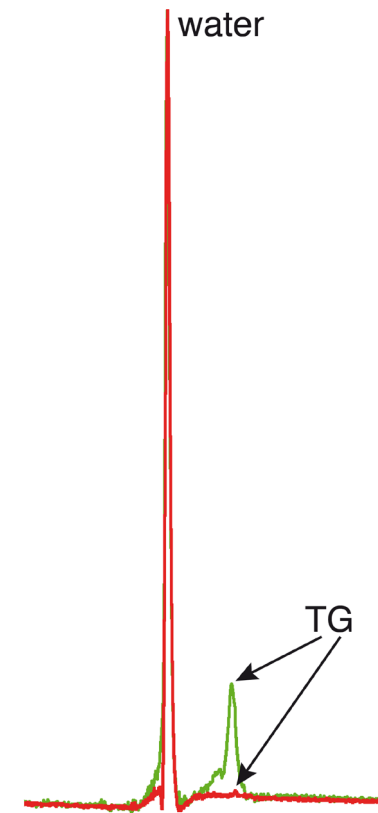


FIGURE 3. Examples of spectra including the renal parenchyma and sinus, and including only the renal parenchyma. Unsuppressed localized renal proton spectra of triglyceride (TG) content with deliberate planning of the voxel including the renal sinus (in green) and including only the renal parenchyma (in red). Percentages TG content in this particular volunteer were 18% (renal sinus) and 0.64% (parenchyma). doi:10.1371/journal.pone.0062209.g003

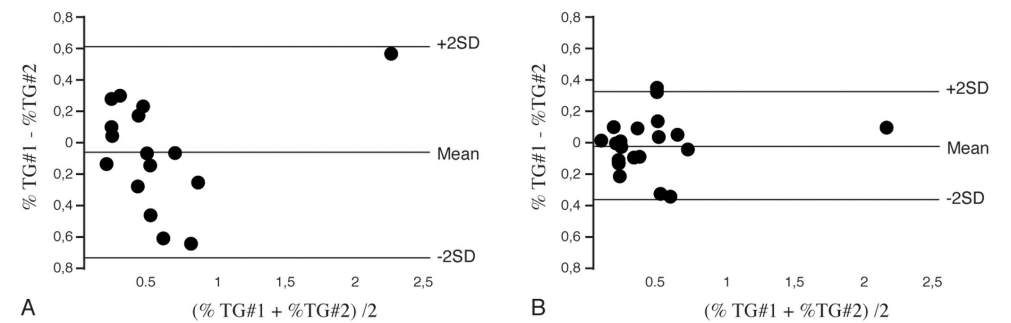


FIGURE 4. Reproducibility plots of renal triglyceride content. Bland-Altman plots of renal cortical triglyceride (TG) content calculated from spectra without ($n = 16$, A) the use of the respiratory navigator, and with ($n = 20$, B) the

use of the respiratory navigator showing narrower limits of agreement/improved reproducibility. doi:10.1371/journal.pone.0062209.g004

Mean %TG in the first and second session without the use of the respiratory navigator were respectively $0.58 \pm 0.12\%$ and $0.51 \pm 0.14\%$ ($P = \text{NS}$). Mean %TG in the first and second session with respiratory navigator gating were respectively $0.44 \pm 0.10\%$ and $0.43 \pm 0.10\%$. ($P = \text{NS}$ between sessions and $P = \text{NS}$ compared to respiratory gated measurements). One volunteer showed higher TG content compared to all others (2.1 and 2.2% with the use of respiratory motion compensation and without motion compensation respectively), albeit no technical explanation could be found (e.g. erroneous planning or navigator dysfunction).

Coefficient of variation without the use of the navigator was 42% which improved to 27% with use of respiratory motion compensation. ICC without the use of the respiratory navigator was 0.79 [95% confidence interval 0.51–0.92, $P < 0.001$] and improved to 0.92 [95% confidence interval 0.81–0.97, $P < 0.001$] with the use of respiratory motion compensation. Moreover, Bland-Altman plots (Figure 4) showed narrower limits of agreements with the use of the respiratory navigator, with a significant improvement in variability with the use of the respiratory navigator compared to ungated measurements, Pearson correlation (derived from the test by Pitman) of -0.59 , $P < 0.05$.

DISCUSSION

The present study shows that metabolic imaging of the human kidney for detection of cortical TG content using $^1\text{H-MRS}$ is feasible. Respiratory motion compensation improves spectral quality and measurement reproducibility.

Intracellular lipid accumulation causing lipotoxicity in humans with the metabolic syndrome or type-2 diabetes mellitus, as assessed with $^1\text{H-MRS}$, has been associated with organ dysfunction, such as non-alcoholic fatty liver disease,²⁰ cardiac diastolic dysfunction^{9,21} and pancreatic beta cell dysfunction.^{22,23} Moreover, respiratory motion compensation techniques to assess these lipid pools have been used in $^1\text{H-MRS}$ previously, including the heart and pancreas.^{11,24,25} The mean percentage of renal TG content in the present study content is in line with previous, Dixon-based techniques.²⁶

The ratio of TG and water show values which are comparable to the quantified amounts of TG found in the human heart.¹¹ However, one subject showed a consistently higher percentage, which could not be attributed to technical failure, physical activity or nutritional status. Moreover, this volunteer was not different from other subjects in terms of age. In contrast, deliberate planning of the voxel in the region of the renal sinus in a subset of volunteers showed clear overestimation, with TG values ranging from 8 to 25 percent. We can therefore not exclude a relatively wide range in physiological TG content in humans. Future studies on the effects of age, gender differences and the relation of renal cortical TG content with parameters of renal function or proteinuria should address this variability in TG content. A recent study indeed showed an age related increase in renal lipid content in mice, associated with increased glomerulosclerosis,²⁷ as well as an increase after a high-fat diet.²⁸ Moreover, high-fat diet induced renal steatosis is reversed with the use of a peroxisome proliferator-activated alpha agonist (which regulates renal lipolysis) in mice, with associated improvements in albuminuria and fibrosis.²⁹ In addition to the PPAR-gamma pathway, the reninangiotensin aldosterone system activation has also been linked to renal adipogenesis. Lisinopril, an ACE-inhibitor, caused normalization of renal adipogenesis and diminished lipid accumulation in uninephrectomized rats.³⁰ Moreover, it was shown in pigs with the metabolic syndrome that renal adiposity was associated with glomerular hyperfiltration and microvascular proliferation.⁶ These

animal studies suggest that renal adipogenesis is linked to critical pathways in obesity-associated renal disease with possibilities for intervention. However, data in humans is scarce. In humans renal sinus fat is associated with intra-abdominal and retroperitoneal fat content and with control of hypertension.³¹

During respiration, movement of the diaphragm causes a displacement of the kidney relative to the spectroscopic voxel. Respiration may thereby influence spectral accuracy and reproducibility by influencing shimming, water suppression as well as varying partial volume changes in fat fraction. To overcome these problems, respiratory motion compensation has been used before to improve $^1\text{H-MRS}$ spectral quality. For example by using triggering on exhalation,³² or with breath-hold acquisition.³³ Both studies were not primarily designed for detection and reproducibility of renal TG content. However, one study reports variations in lipid content as a consequence of contamination with lipids from outside the region of interest during free breathing. The present results are in line with these findings, as spectral quality and reproducibility of renal TG stores improved with respiratory motion compensation. Moreover, all spectra obtained with respiratory motion compensation could be accurately fitted, whereas 4 of the spectra obtained without respiratory motion compensation were of insufficient quality, due to poor water suppression or ghosting signals.

The improvements in spectral quality in terms of linewidth are in line with previous reported values for cardiac and skeletal muscle spectroscopy.^{11,34}

Moreover, the use of the respiratory navigator improved the coefficient of variation and showed narrower limits of agreement in Bland-Altman analyses. However, the resulting coefficient of variation of 27% remains relatively high. We hypothesize this may be due to local inhomogeneities in renal parenchymal TG content, or variations in cortical and medullar TG content contribution within the voxel, as the voxel is close to the renal medulla and TG content may be distributed differentially.^{35,36} Nevertheless, reproducibility improved with respiratory motion compensation and seems necessary for human in vivo TG quantification.

A limitation of our study may be that $^1\text{H-MR}$ spectra were obtained in one position in a single kidney only. Future studies should focus on possible regional differences in lipid content, possible differences in position in the cortex or medulla and the relationship with parameters of the metabolic syndrome, such as abdominal fat content, liver fat content and clinical parameters such as body mass index, serum TG content, cholesterol as well as renal function and proteinuria.

CONCLUSIONS

Metabolic imaging of the human kidney using $^1\text{H-MRS}$ is a feasible tool to assess cortical TG content in humans in vivo and the use of respiratory motion compensation with navigator echoes significantly improves spectral quality and reproducibility. Therefore, respiratory motion correction seems a necessity for metabolic imaging of renal TG content in vivo.

REFERENCES

- Meguid EL NA, Bello AK (2005) Chronic kidney disease: the global challenge. *Lancet* 365: 331–340. S0140673605177897 [pii];10.1016/S0140-6736(05)17789-7 [doi].
- Ejerblad E, Fored CM, Lindblad P, Fryzek J, McLaughlin JK, et al. (2006) Obesity and risk for chronic renal failure. *J Am Soc Nephrol* 17: 1695–1702. ASN.2005060638 [pii];10.1681/ASN.2005060638 [doi].
- Hsu CY, McCulloch CE, Iribarren C, Darbinian J, Go AS (2006) Body mass index and risk for end-stage renal disease. *Ann Intern Med* 144: 21–28. 144/1/21 [pii].
- Kambham N, Markowitz GS, Valeri AM, Lin J, D'Agati VD (2001) Obesity-related glomerulopathy: an emerging epidemic. *Kidney Int* 59: 1498–1509. kid646 [pii];10.1046/j.1523-1755.2001.0590041498.x [doi].
- Dominguez J, Wu P, Packer CS, Temm C, Kelly KJ (2007) Lipotoxic and inflammatory phenotypes in rats with uncontrolled metabolic syndrome and nephropathy. *Am J Physiol Renal Physiol* 293: F670–F679. 00021.2007 [pii];10.1152/ajprenal.00021.2007 [doi].
- Li Z, Woollard JR, Wang S, Korsmo MJ, Ebrahimi B, et al. (2011) Increased glomerular filtration rate in early metabolic syndrome is associated with renal adiposity and microvascular proliferation. *Am J Physiol Renal Physiol* 301: F1078–F1087. ajprenal.00333.2011 [pii];10.1152/ajprenal.00333.2011 [doi].
- Wang Z, Jiang T, Li J, Proctor G, McManaman JL, et al. (2005) Regulation of renal lipid metabolism, lipid accumulation, and glomerulosclerosis in FVBdb/db mice with type 2 diabetes. *Diabetes* 54: 2328–2335. 54/8/2328 [pii].
- Wu Y, Liu Z, Xiang Z, Zeng C, Chen Z, et al. (2006) Obesity-related glomerulopathy: insights from gene expression profiles of the glomeruli derived from renal biopsy samples. *Endocrinology* 147: 44–50. en.2005-0641 [pii];10.1210/en.2005-0641 [doi].
- van der Meer RW, Lamb HJ, Smit JW, de Roos A (2012) MR Imaging Evaluation of Cardiovascular Risk in Metabolic Syndrome. *Radiology* 264: 21–37. 264/1/21 [pii];10.1148/radiol.12110772 [doi].
- Boesch C, Machann J, Vermathen P, Schick F (2006) Role of proton MR for the study of muscle lipid metabolism. *NMR Biomed* 19: 968–988. 10.1002/nbm.1096 [doi].
- van der Meer RW, Doornbos J, Kozerke S, Schar M, Bax JJ, et al. (2007) Metabolic imaging of myocardial triglyceride content: reproducibility of 1H MR spectroscopy with respiratory navigator gating in volunteers. *Radiology* 245: 251–257. 245/1/251 [pii];10.1148/radiol.2451061904 [doi].
- Schar M, Kozerke S, Boesiger P (2004) Navigator gating and volume tracking for double-triggered cardiac proton spectroscopy at 3 Tesla. *Magn Reson Med* 51: 1091–1095.
- Wang Y, Rossman PJ, Grimm RC, Riederer SJ, Ehman RL (1996) Navigatorecho-based real-time respiratory gating and triggering for reduction of respiration effects in three-dimensional coronary MR angiography. *Radiology* 198: 55–60.
- Kozerke S, Schar M, Lamb HJ, Boesiger P (2002) Volume tracking cardiac 31P spectroscopy. *Magn Reson Med* 48: 380–384.
- Naressi A, Couturier C, Devos JM, Janssen M, Mangeat C, et al. (2001) Javabased graphical user interface for the MRUI quantitation package. *MAGMA* 12: 141–152.
- Boesch C, Slotboom J, Hoppeler H, Kreis R (1997) In vivo determination of intra-myocellular lipids in human muscle by means of localized 1H-MR spectroscopy. *Magn Reson Med* 37: 484–493.
- Rico-Sanz J, Hajnal JV, Thomas EL, Mierisova S, Ala-Korpela M, et al. (1998) Intracellular and extracellular skeletal muscle triglyceride metabolism during alternating intensity exercise in humans. *J Physiol* 510 (Pt 2): 615–622.
- Schick F, Eismann B, Jung WI, Bongers H, Bunse M, et al. (1993) Comparison of localized proton NMR signals of skeletal muscle and fat tissue in vivo: two lipid compartments in muscle tissue. *Magn Reson Med* 29: 158–167.
- Pitman EJG (1939) A note on normal correlation. *Biometrika* 31: 9–12.
- Reeder SB, Cruite I, Hamilton G, Sirlin CB (2011) Quantitative Assessment of Liver Fat with Magnetic Resonance Imaging and Spectroscopy. *J Magn Reson Imaging* 34: spcone. 10.1002/jmri.22775 [doi].
- Hammer S, Snel M, Lamb HJ, Jazet IM, van der Meer RW, et al. (2008) Prolonged caloric restriction in obese patients with type 2 diabetes mellitus decreases myocardial triglyceride content and improves myocardial function. *J Am Coll Cardiol* 52: 1006–1012. S0735-1097(08)02226-2 [pii];10.1016/j.jacc.2008.04.068 [doi].
- Szczepaniak LS, Victor RG, Mathur R, Nelson MD, Szczepaniak EW, et al. (2012) Pancreatic Steatosis and Its Relationship to beta-Cell Dysfunction in Humans: Racial and ethnic variations. *Diabetes Care* 35: 2377–2383. dc12-0701 [pii];10.2337/dc12-0701 [doi].
- Tushuizen ME, Bunck MC, Pouwels PJ, Bontemps S, van Waesberghe JH, et al. (2007) Pancreatic fat content and beta-cell function in men with and without type 2 diabetes. *Diabetes Care* 30: 2916–2921. dc07-0326 [pii];10.2337/dc07-0326 [doi].
- Lingvay I, Esser V, Legendre JL, Price AL, Wertz KM, et al. (2009) Noninvasive quantification of pancreatic fat in humans. *J Clin Endocrinol Metab* 94: 4070–4076. jc.2009-0584 [pii];10.1210/jc.2009-0584 [doi].
- Reingold JS, McGavock JM, Kaka S, Tillery T, Victor RG, et al. (2005) Determination of triglyceride in the human myocardium by magnetic resonance spectroscopy: reproducibility and sensitivity of the method. *Am J Physiol Endocrinol Metab* 289: E935–E939. 00095.2005 [pii];10.1152/ajpendo.00095.2005 [doi].
- Sijens PE, Edens MA, Bakker SJ, Stolk RP (2010) MRI-determined fat content of human liver, pancreas and kidney. *World J Gastroenterol* 16: 1993–1998.
- Jiang T, Liebman SE, Lucia MS, Li J, Levi M (2005) Role of altered renal lipid metabolism and the sterol regulatory element binding proteins in the pathogenesis of age-related renal disease. *Kidney Int* 68: 2608–2620. KID733 [pii];10.1111/j.1523-1755.2005.00733.x [doi].
- Jiang T, Wang Z, Proctor G, Moskowitz S, Liebman SE, et al. (2005) Diet-induced obesity in C57BL/6J mice causes increased renal lipid accumulation and glomerulosclerosis via a sterol regulatory element-binding protein-1c-dependent pathway. *J Biol Chem* 280: 32317–32325. M500801200 [pii];10.1074/jbc.M500801200 [doi].
- Tanaka Y, Kume S, Araki S, Isshiki K, Chin-Kanasaki M, et al. (2011) Fenofibrate, a PPARalpha agonist, has renoprotective effects in mice by enhancing renal lipolysis. *Kidney Int* 79: 871–882. ki2010530 [pii];10.1038/ki.2010.530 [doi].
- Sui Y, Zhao HL, Fan RR, Guan J, He L, et al. (2010) Renin-angiotensin system activation in renal adipogenesis. *Am J Physiol Renal Physiol* 298: F391–F400. 00445.2009 [pii];10.1152/ajprenal.00445.2009 [doi].
- Chughtai HL, Morgan TM, Rocco M, Stacey B, Brinkley TE, et al. (2010) Renal sinus fat and poor blood pressure control in middle-aged and elderly individuals at risk for cardiovascular events. *Hypertension* 56: 901–906. HYPERTENSIONAHA.110.157370 [pii];10.1161/HYPERTENSIONAHA.110.157370 [doi].
- Dixon RM, Frahm J (1994) Localized proton MR spectroscopy of the human kidney in vivo by means of short echo time STEAM sequences. *Magn Reson Med* 31: 482–487.
- Katz-Brull R, Rofsky NM, Lenkinski RE (2003) Breathhold abdominal and thoracic proton MR spectroscopy at 3T. *Magn Reson Med* 50: 461–467. 10.1002/mrm.10560 [doi].
- Torriani M, Thomas BJ, Halpern EF, Jensen ME, Rosenthal DI, et al. (2005) Intramyocellular lipid quantification: repeatability with 1H MR spectroscopy. *Radiology* 236: 609–614. 236/2/609 [pii];10.1148/radiol.2362041661 [doi].
- Gold M (1970) An investigation of the lipid metabolism of dog kidney medulla and cortex. *Lipids* 5: 293–298.
- Garrod S, Humpfer E, Spraul M, Connor SC, Polley S, et al. (1999) AIDMRM6.3.0. CO;2-M [pii].

A large, semi-transparent green number '7' is positioned in the background on the right side of the slide.

**METABOLIC IMAGING
OF FATTY KIDNEY
IN DIABESITY
VALIDATION AND
DIETARY INTERVENTION**

7 METABOLIC IMAGING OF FATTY KIDNEY IN DIABESITY: VALIDATION AND DIETARY INTERVENTION

Adapted from *Nephrology Dialysis Transplantation*. 2017 Sep 15 [Epub ahead of print].

Authors

Jacqueline T. Jonker,^{1*} Paul de Heer,^{2*} Marten A. Engelse,¹ Evelien H. van Rosenberg,¹ Celine Q.F. Klessens,³ Hans J. Baelde,³ Ingeborg M. Bajema,³ Sietse Jan Koopmans,⁴ Paulo G. Coelho,⁵ Trea C.M. Streefland,⁶ Andrew G. Webb,⁷ Ilona A. Dekkers,² Ton J. Rabelink,² Patrick C.N. Rensen,⁶ Hildo J. Lamb,² Aiko P.J. de Vries.¹

¹ Department of Nephrology, Leiden University Medical Center, Leiden, The Netherlands

² Department of Radiology, C.J. Gorter Center for High Field MR, Leiden University Medical Center, Leiden, The Netherlands

³ Department of Pathology, Leiden University Medical Center, Leiden, The Netherlands

⁴ Animal Science Group, Wageningen University and Research, Wageningen, The Netherlands

⁵ Department of Biomaterials and Biomimetics, New York University College of Dentistry, New York University, New York, USA

⁶ Department of Endocrinology, Department of Medicine, Leiden University Medical Center, Leiden, the Netherlands

⁷ Department of Radiology, Leiden University Medical Center, Leiden, The Netherlands

⁸ Einthoven Laboratory for Experimental Vascular Medicine, Leiden University Medical Center, Leiden, The Netherlands

* These authors contributed equally to this work.

ABSTRACT

Background

Obesity and type 2 diabetes have not only been linked to fatty liver, but also to fatty kidney and chronic kidney disease. Since non-invasive tools are lacking to study fatty kidney in clinical studies, we explored agreement between proton magnetic resonance spectroscopy (¹H-MRS) and enzymatic assessment of renal triglyceride content (without and with dietary intervention). We further studied the correlation between fatty kidney and fatty liver.

Methods

Triglyceride content in the renal cortex was measured by ¹H-MRS on a 7-Tesla scanner in 27 pigs, among which 15 minipigs had been randomized to a 7-month control diet, cafeteria diet (CAF) or CAF with low-dose streptozocin (CAF-S) to induce insulin-independent diabetes. Renal biopsies were taken from corresponding MRS-voxel locations. Additionally, liver biopsies were taken and triglyceride content in all biopsies was measured by enzymatic assay.

Results

Renal triglyceride content measured by ¹H-MRS and enzymatic assay correlated positively ($r = 0.86$, $P < 0.0001$). Compared with control diet-fed minipigs, renal triglyceride content was higher in CAF-S-fed minipigs (137 ± 51 nmol/mg protein, mean \pm standard error of the

mean, $P < 0.05$), but not in CAF-fed minipigs (60 ± 10 nmol/mg protein) compared with controls (40 ± 6 nmol/mg protein). Triglyceride contents in liver and kidney biopsies were strongly correlated ($r = 0.97$, $P < 0.001$).

Conclusions

Non-invasive measurement of renal triglyceride content by ¹H-MRS closely predicts triglyceride content as measured enzymatically in biopsies, and fatty kidney appears to develop parallel to fatty liver. ¹H-MRS may be a valuable tool to explore the role of fatty kidney in obesity and type 2 diabetic nephropathy in humans in vivo.

INTRODUCTION

Over the past decades, the prevalence of obesity and type 2 diabetes has grown to epidemic proportions.¹ Obesity, in particular central obesity, is associated with metabolic dysfunction, which drives the development of insulin resistance leading to type 2 diabetes and ultimately end organ damage. The combination of obesity and type 2 diabetes, also referred to as diabetes, is often accompanied by other cardiovascular risk factors, including hypertension and dyslipidaemia. Common early markers of renal disease like glomerular hyperfiltration and increased urinary albumin are more prevalent in both obesity and type 2 diabetes.² Furthermore, renal pathology has shown considerable overlap between obesity and type 2 diabetes.³

How (early) diabetes may lead to incipient chronic kidney disease remains to be understood, but ectopic lipid accumulation in the kidney (fatty kidney) has gained appreciation as a novel potential pathway.^{2,4-6} Diabetes is associated with lipid accumulation in non-adipose tissue such as liver, skeletal muscle and heart, and this so-called ectopic fat may interfere with cellular function in the respective organ.⁷⁻¹⁰ Notably, obesity and type 2 diabetes have been associated with renal lipid accumulation in both human and porcine kidneys with differences in anatomical distribution between glomeruli and tubuli, as well as cortex and medulla.^{11,12} Increased renal lipid content has also been linked to functional and structural renal hyperfiltration¹², obesity-related glomerulopathy² and type 2 diabetic nephropathy¹³. Various rodent models have shown that intervention in cellular lipid pathways attenuated obesity-related glomerulopathy or diet-induced chronic kidney disease.¹⁴ To date, translation of such experimental evidence to the clinical arena has been hampered by lack of a non-invasive diagnostic tool to sequentially monitor renal lipid accumulation in obesity and type 2 diabetes mellitus.

Proton magnetic resonance spectroscopy (¹H-MRS) is a non-invasive and reproducible technique that has been used successfully to quantify lipid content in heart, liver and muscle.¹⁵⁻¹⁷ Recently, feasibility and reproducibility of renal ¹H-MRS in vivo was shown.¹⁸ However, few ¹H-MRS protocols have been validated against tissue biopsies.

Therefore, we explored the agreement of the non-invasive ¹H-MRS renal triglyceride measurement, using a 7-Tesla magnetic resonance (MR) scanner, against a biochemical assay (as gold standard) to determine lipid accumulation in of porcine kidneys. Secondly, we measured renal triglyceride content after a dietary intervention study in minipigs. We investigated the effects of a high-fat, high-cholesterol cafeteria diet without (CAF) and with low-dose streptozocin (STZ) (CAF-S) to induce non-insulin-dependent diabetes mellitus, compared with standard diet on renal and hepatic triglyceride content and distribution.

MATERIALS AND METHODS

Group A

Fourteen left-sided porcine kidneys were harvested from two Dutch pig slaughter lines. The kidneys were harvested within 30 min of termination to limit warm ischaemia time and were placed on ice. Kidneys were flushed with University of Wisconsin (UW) fluid and were scanned upon arrival. Tissue biopsies were taken from both the upper and lower pole of each kidney, immediately after scanning. The biopsy locations were visually matched to the areas where the ¹H-MRS measurements were performed. Biopsies were snap-frozen in liquid nitrogen and stored at -80°C.

Group B

A total of 15 Göttingen minipigs¹⁹ were studied after they had been randomized to two different diets. The control group received a diet consisting primarily of barley, wheat and soya bean oil. The CAF group was fed a cafeteria diet²⁰, with a high content of lard, fructose, sucrose and added cholesterol. Five of the CAF-fed pigs were additionally treated with STZ after 5 months. The dose of STZ was individually adjusted to induce non-insulin-dependent diabetes to model type 2 diabetes. After 7 months of diet, the pigs were euthanized. Directly after termination, blood was drawn and a liver biopsy was taken. The whole study was executed at Ecole Veterinaire D'Alfort, France, and was approved by the local ethics committee for animal experiments. The same harvesting and analyses protocols performed for Group A were followed: left-sided kidneys were harvested with a maximum of 30 min warm ischaemia time, kidneys were flushed with UW fluid and transported to the hospital in the Netherlands on ice, for subsequent 7-Tesla MR scanning. After each MR scan, renal biopsies were taken from the corresponding MRS-voxel location of the upper and lower kidney poles. Biopsies were snap-frozen and stored at -80°C. For both Groups A and B, all kidneys had a maximum cold ischaemia time of 20 h before ¹H-MRS was performed.

Measurements

Proton Magnetic Resonance Spectroscopy

A 7-Tesla Philips Magnetic Resonance Imaging (MRI) scanner (Philips Healthcare, Best, The Netherlands) was used to measure renal triglyceride content by ¹H-MRS. A Nova quadrature transmit and 32-channel receive head coil (Nova Medical, Wilmington, MA, USA) was used for transmission and reception. A survey together with a Dixon water-fat scan was performed to position the MRS voxel (10 x 10 x 10mm³) within the cortex of the kidney trying to avoid the medulla as much as possible.²¹ On the Dixon scan fat image (Figure 1B) correct placement was confirmed, carefully avoiding extracellular (sinus or perirenal) lipids in the voxel. Secondly, measurements were performed in the upper and lower pole of each kidney. Stimulated echo acquisition mode (STEAM) spectra were acquired with an echo time of 8.2 ms without water suppression [repetition time (TR) 9 s, 3 averages] and with Multiply Optimized Insensitive Suppression Train (MOIST) water suppression (TR 3.5 s, 96 averages).^{22,23} The MRS acquisition had a bandwidth of 3000 Hz and 4096 samples were acquired resulting in a spectral resolution of 0.73 Hz/sample. All spectra were fitted in the time-domain using the Java-based MR User Interface (jMRUI).²⁴ The advanced method for accurate, robust and efficient spectral fitting (AMARES) algorithm was used to fit the resonances to a Gaussian line shape. Triglyceride content was calculated as a percentage of the (unsuppressed) water peak using the following equation:

$$TG = \frac{TG \text{ methyl } (CH_3) + TG \text{ methylene } (CH_2n)}{Water + TG \text{ methyl } (CH_3) + TG \text{ methylene } (CH_2n)} \times 100\% \quad (1)$$

where, TG = renal triglyceride content (%), TG methyl = area of the methyl resonance at 0.9 ppm (arbitrary unit), TG methylene = area of the methylene resonance at 1.3 ppm (arbitrary unit), Water = area of the water resonance (arbitrary unit).

Enzymatic measurement of lipids in renal and liver biopsy

The biopsies from the upper and lower pole of each kidney, as well as the liver biopsies, were snap-frozen in liquid nitrogen, homogenized and total lipids were extracted according to a modified protocol from Bligh and Dyer.²⁵ Total triglycerides were measured by an enzymatic kit (no. 11488872, Roche Diagnostics, Rotkreuz ZG, Switzerland). The triglyceride content per biopsy was divided by the protein content (nmol triglycerides/mg protein) to correct for the size of the biopsy.

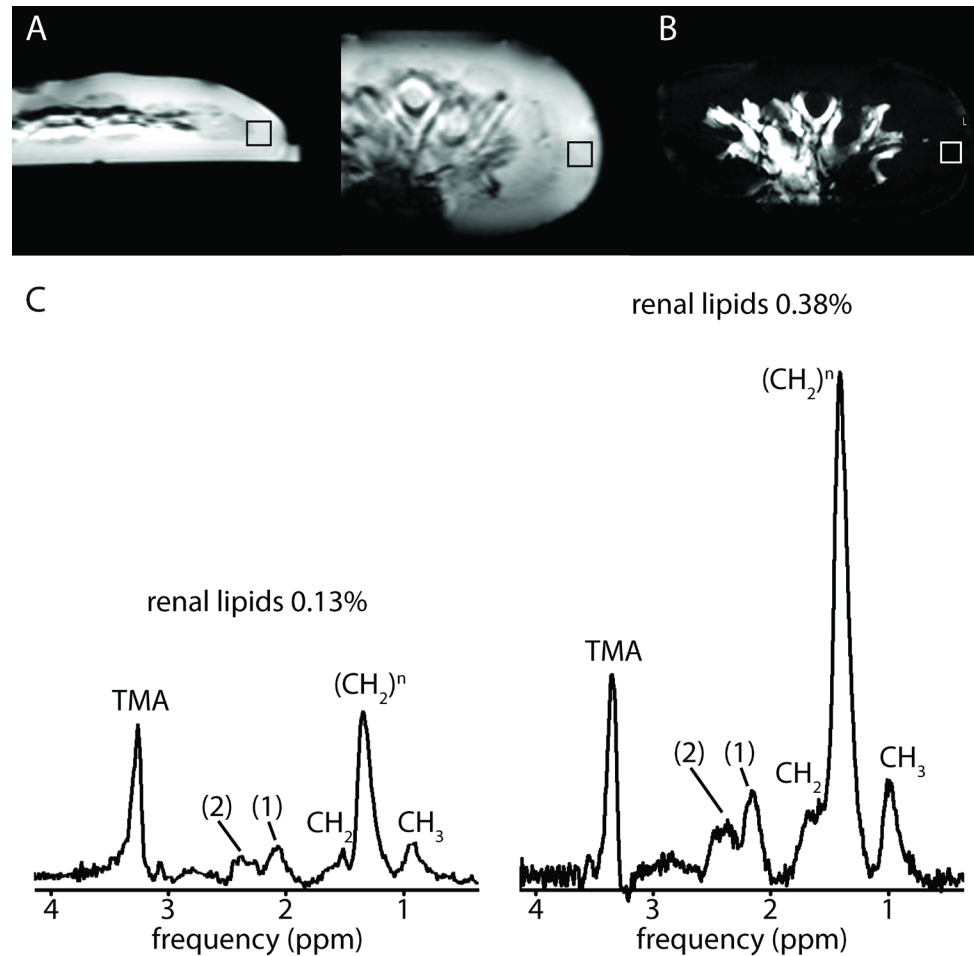


FIGURE 1: Placement of the voxel (black box) in the kidney cortex on a transverse and coronal survey **(A)** and Dixon fat image **(B)**. Below the surveys are two spectra **(C)** acquired from the kidney cortex of two different kidneys. Spectra have been selected to show an example of low and high renal triglyceride (TG) content and have been scaled to the water signal to be able to visually compare the two.

For quantification of TG content the (CH₂)ⁿ (1.3 ppm) and the CH₃ (0.9 ppm) resonances are used. Other visible resonances in the spectra are CH₂CH₂COO marked with number 1 at 1.5 ppm, CHCH₂=CHCH₂ marked with number 2 at 2 ppm and CH₂COO marked with number 3 at 2.2 ppm, and a trimethylamine (TMA) resonance at 3.2 ppm.

Oil-red-O staining

Frozen kidney sections (10 μm thickness) were cut on a Reichert cryostat microtome. Oil Red O (ORO) staining was performed by incubation of the slides with an ORO solution (2 mg/mL in 40% isopropanol). Sections were rinsed with ethanol, covered with Aqua-Mount mounting media and digitized with a Philips Ultra-Fast 1.6 RA Scanner (Philips, Best, The Netherlands). The ORO-positive surface area was measured using ImageJ (US National Institutes of Health, Bethesda, MD, USA) on five random selected areas of the renal cortex, and the percentage of the positive area was calculated.

Other laboratory measurements

Concentrations of plasma triglycerides and creatinine [both total coefficient of variation (C_v): 1.0–1.2%, determined by vendor], urinary creatinine (total C_v: 0.5–0.7%) and urinary protein (total C_v: 0.2–0.6%) were measured on a Modular P800 analyser (Roche, Basel, Switzerland). Plasma fructosamine (total C_v: 1.2–1.5%) was measured using a Cobas 6000 analyser (Roche).

Statistics

All statistical analyses were performed using SPSS version 22.0 (IBM SPSS Statistics for Windows, IBM Corp., Armonk, NY, USA). Plots were created using Graph Pad (Graph Pad Software, La Jolla, CA, USA). All but one analysis were performed with the average triglyceride content from the upper and lower pole of each kidney. Bland–Altman analysis was performed to evaluate the agreement between renal triglyceride content by ¹H-MRS and renal lipid content by enzymatic assay, after normalization of the data. In one case, the triglyceride content of a single pole was taken due to a corrupt MRS data file. Agreement between the triglyceride measurement techniques was evaluated by linear regression with a 95% prediction interval. Group differences between the three experimental groups were analysed using analysis of variance (ANOVA). Least significant difference (LSD) post hoc tests were used in case of a significant difference. Non-normally distributed data were log-transformed and checked for normality after transformation. Data are expressed as mean values ± standard error of the mean (SEM) and a probability value of < 0.05 was considered statistically significant.

RESULTS

Validation of renal triglyceride quantification by $^1\text{H-MRS}$

Renal triglyceride content was measured in 29 left-sided porcine kidneys by $^1\text{H-MRS}$ and by enzymatic assay. Two measurements had to be excluded from further analysis due to a failed measurement in the enzymatic assay and one due to a corrupt MRS data file, resulting in a total of 27 measurements ($n = 12$ from Group A, $n = 15$ from Group B). In Group A (slaughter pigs), the mean renal triglyceride content was $0.23 \pm 0.03\%$ (mean \pm SEM) as measured by $^1\text{H-MRS}$ and 111 ± 15 nmol/mg protein as measured by enzymatic assay. The mean renal triglyceride content in Group B (minipigs) was $0.15 \pm 0.03\%$ as measured by $^1\text{H-MRS}$ and 79 ± 20 nmol/mg protein as quantified by enzymatic assay. Data from Groups A and B were pooled and triglyceride content measured by $^1\text{H-MRS}$ and enzymatic assay showed a positive correlation ($r = 0.86$, $P < 0.0001$, Figure 2). The regression equation was as follows: triglycerides measured by $^1\text{H-MRS}$ (%) = $0.03 + 0.0017 \times$ triglycerides measured by enzymatic assay (nmol/mg). The triglyceride content for the pooled data ranged from 0.06% to 0.8% as measured by $^1\text{H-MRS}$ and from 30 to 331 nmol/mg protein as measured by enzymatic assay. The Bland-Altman analysis using the normalized data showed good agreement with a bias of 0.00 (limits of agreement -0.8 ; 0.8) for $^1\text{H-MRS}$ and enzymatic assay measurements of renal lipid content over the metabolic spectrum (Figure 2B).

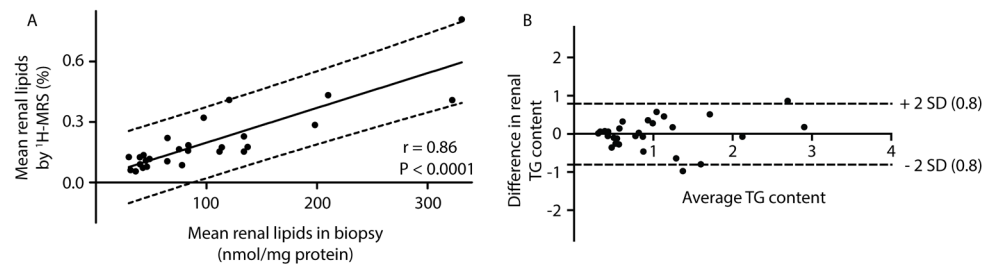


FIGURE 2: Correlation (left) and Bland-Altman difference-average plot (right) of renal triglyceride (TG) content measured by $^1\text{H-MRS}$ and enzymatic assay in biopsies, using pooled data from both Group A (A) (12 slaughter pigs) and Group B (B) (15 minipigs) showing a positive correlation ($R=0.86$, $P < 0.0001$).

Effects of CAF and STZ

The minipigs were 2.7 ± 0.2 years of age at termination. The pigs in the control group were heavier at the start of the study (62.7 ± 3.3 kg, $P < 0.05$) than the pigs in the CAF group (51.4 ± 2.0 kg) and CAF-S group (49.7 ± 2.8 kg). The 7-month CAF induced a significantly larger weight gain (39.6 ± 3.6 kg) than the control diet (23.4 ± 3.1 kg, $P < 0.05$) and the CAF-S diet (23.2 ± 5.5 kg, $P < 0.05$, Figure 3). Serum fructosamine was higher in the CAF-S group (358 ± 31 mmol/L, $P < 0.05$), than in the CAF (264 ± 6 mmol/L) and control groups (259 ± 11 mol/L). Serum triglycerides, serum creatinine and urine protein did not significantly differ between the groups.

Renal triglyceride content was higher in the CAF-S group (137 ± 51 nmol/mg protein) compared with the control group (40 ± 6 nmol/mg protein, $P < 0.05$) (Figure 3). Renal triglyceride content in the CAF group (60 ± 10 nmol/mg protein) was not significantly different from the control group (Figure 3). Renal triglyceride content measured by proton

MR spectroscopy showed a similar trend between the groups, however, this was not statistically significant.

Similarly, hepatic triglyceride content after the 7-month diet was higher in the CAF-S group (417 ± 157 nmol/mg protein) compared with the control group (67 ± 11 nmol/mg protein, $P < 0.05$). The CAF group (141 ± 49 nmol/mg protein) had a trend towards higher hepatic triglyceride content than the control group, but this was not significantly different (Figure 3). We observed a significant correlation between renal and hepatic triglyceride content measured by enzymatic assay ($n = 14$, $r = 0.97$, $P < 0.001$, Figure 4).

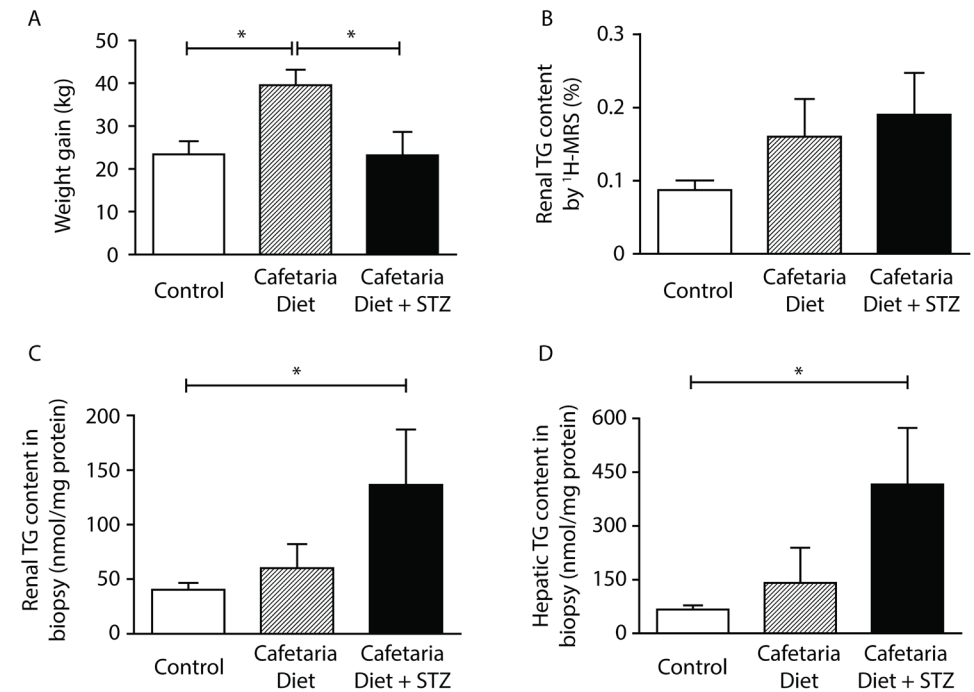


FIGURE 3: Weight gain (A), renal triglyceride (TG) content measured by proton magnetic resonance spectroscopy ($^1\text{H-MRS}$, B), renal TG content from renal biopsy by enzymatic assay (C) and hepatic TG content from liver biopsy by

enzymatic assay (D) after 7 months of control diet, CAF or CAF-S. Data are presented as mean \pm SEM ($n = 15$ for renal triglycerides, $n = 14$ for hepatic triglycerides). * $P < 0.05$.

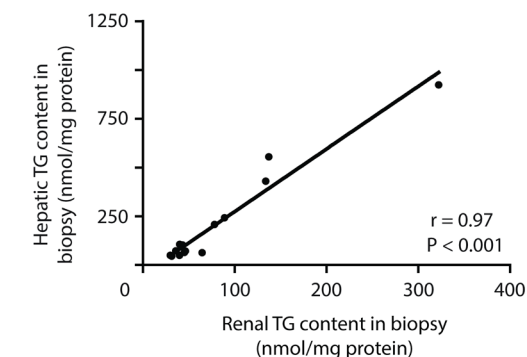


FIGURE 4: Correlation between renal and hepatic triglyceride (TG) content after 7 months of diet, measured by enzymatic assay in biopsies ($n = 14$).

Lipid distribution

We also assessed lipid localization by ORO staining. The lipid content was very low in biopsies of the control diet group (percentage staining: $0.2 \pm 0.0\%$), and markedly higher in those of the CAF group ($3.7 \pm 1.9\%$, $P < 0.05$ versus control diet) and CAF-S group ($9.6 \pm 6.3\%$, $P < 0.05$ versus control diet). There was pronounced lipid accumulation in the tubuli and to a lesser extent ORO staining was visible in the glomeruli (Figure 5).

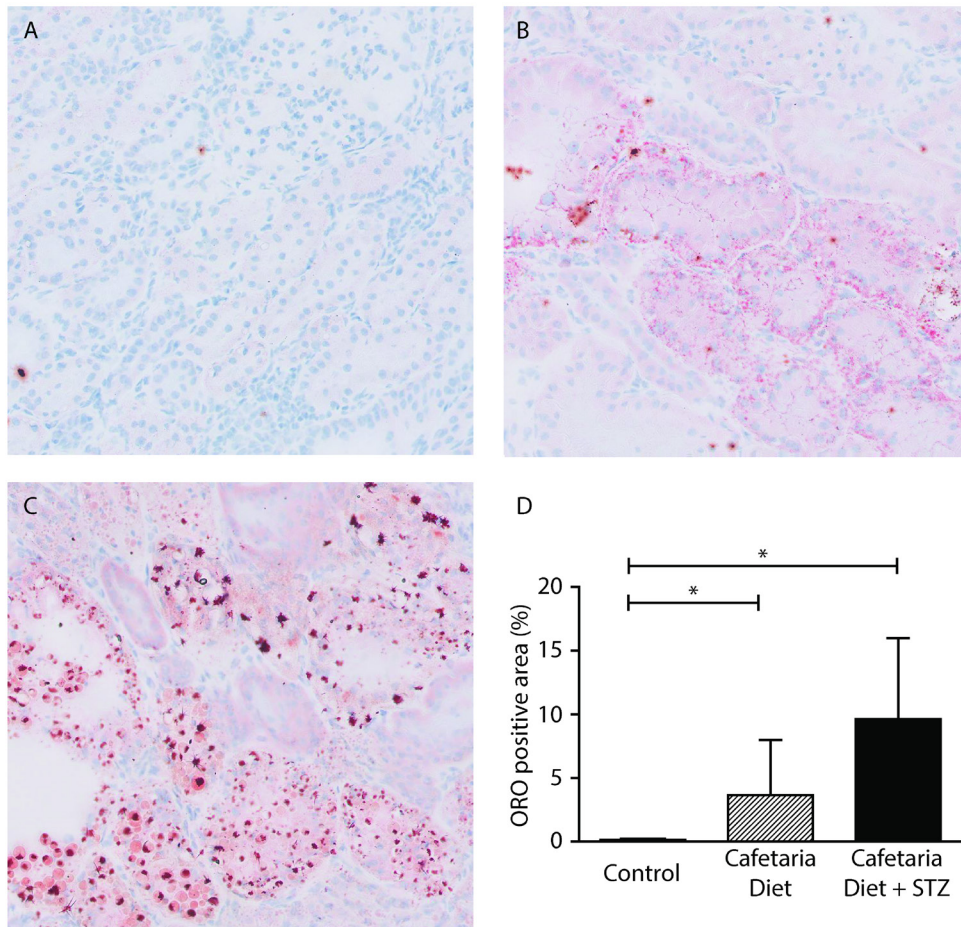


FIGURE 5: Three representative examples of ORO staining for lipids in kidney biopsies from minipigs on a 7 months control (A), CAF (B) or CAF-S (C) diet. (D) Percentage of

biopsy with ORO staining in the three diet groups (mean \pm SEM, $n = 5$ per group). * $P < 0.05$ compared with the control diet.

DISCUSSION

The merit of clinical ^1H -MRS to investigate the role of ectopic lipid accumulation has been clearly established for other organs such as liver, muscle and heart.^{17,26,27} In fact, the development of ^1H -MRS of the heart has led to a better understanding of factors influencing myocardial triglyceride accumulation in relation to cardiac function in both health and diabetes.^{9,17} Our present study is one of the first to explore ^1H -MRS as a non-invasive tool to study fatty kidney in diabetes and to study agreement with tissue biopsies.

Thus far, only few studies have reported on ^1H -MRS of the kidney, most likely owing to the technical difficulties of developing and applying this technique reliably to the kidney for several reasons. Firstly, adjustment for respiratory motion and carefully avoiding contamination by perirenal and sinus fat is necessary to obtain reliable measurements from the kidney cortex only, and not surrounding structures. Secondly, kidney tissue is not homogenous with substantial anatomical and functional variation between cortex and medulla as well as glomeruli and tubuli. Lastly, due to the limited space in the kidney cortex, the volume of the measured voxel has to be small, resulting in a much lower signal-to-noise-ratio compared with e.g. heart and liver.

This notwithstanding, we previously reported a feasibility and reproducibility study of renal ^1H -MRS in healthy (non-obese) volunteers in vivo, but variation was apparent even in this relative homogenous group of subjects.¹⁸ Consequently, we aimed to improve our knowledge on triglyceride distribution across the metabolic spectrum of diabetes and across kidney anatomy with regard to voxel placement and data acquisition. Also, few spectroscopy protocols underwent validation and testing against invasive, gold standard assessment of triglycerides. Because of the impossibility of obtaining enough discarded kidneys from obese and type 2 diabetic post mortem kidney donors to perform a validation study (those kidneys are often not offered for transplantation), we turned to similar-sized porcine kidneys to test our clinical ^1H -MRS protocol. This study in porcine kidneys shows that ^1H -MRS closely predicts the triglyceride content as measured by enzymatic assay of kidney biopsies (gold standard) and, therefore, it may also be a valuable tool to study fatty kidney in humans.

To evaluate the renal triglyceride content over the metabolic spectrum in conjunction with the hepatic triglyceride content, we used minipigs fed a high fat, high cholesterol diet to develop a metabolic syndrome phenotype including high amounts of visceral fat and insulin resistance.¹⁹ Because those pigs have a large pancreatic beta cell capacity, it takes a very long time to develop type 2 diabetes. Therefore, the pigs were individually treated with a low dose of STZ to damage a part of the pancreatic beta cell capacity, to create non-insulin-dependent diabetes that reflects type 2 diabetes. Using this model, we showed that renal triglyceride content increased over the metabolic spectrum in conjunction with hepatic triglycerides.

We observed a trend to an increase in both renal and hepatic triglyceride content in the CAF-only group, however this was not significant. Previous studies have shown correlation between increased bodyweight and increased hepatic and renal triglyceride content in both animals and humans^{11,12,28,29} As our study was exploratory and the animal groups small, the study may have been underpowered to detect a significant difference between the control and CAF group. One possible confounder in this study is the difference in baseline weight of the minipigs, as controls were significantly heavier than the pigs in the intervention groups.

Interestingly, pigs in the CAF-S group, albeit that they had a lower baseline weight and equal increase in body weight during the study, did have increased renal triglyceride content compared with the controls. In diabetes, the increase in inflammation or chronic kidney disease might lead to additional triglyceride redistribution into organs beyond mere obesity and thus accentuate the findings.² We found a strong positive correlation between renal and hepatic triglyceride content. A study in mice has shown that from a certain bodyweight, the expandability of white adipose tissue becomes limited and fat starts to rapidly accumulate ectopically within e.g. the liver.²⁹ It is likely that a similar mechanism may underlie renal triglyceride accumulation, which needs to be explored in future studies.

By using ORO staining, we observed similar trends, with increasing triglyceride content in the CAF group and even more in the CAF-S group. We found that renal triglyceride accumulation was most prominent in renal tubuli, albeit some triglyceride staining was also observed in the glomeruli. This is in accordance with a recent study of human nephrectomies, where triglyceride droplets were predominantly found in tubular cells and to a lesser extent in glomeruli.¹¹ Future studies should focus on even better understanding of how triglyceride accumulation may lead to chronic kidney disease in diabetes and whether this process can be reversed.

CONCLUSION

Non-invasive measurement of renal triglyceride content by ¹H-MRS closely predicts the triglyceride content as measured enzymatically in biopsies. Renal triglyceride content increases over the metabolic spectrum of diabetes and in the current study fatty kidney develops in parallel with fatty liver. ¹H-MRS seems suitable to explore the role of fatty kidney in obesity and type 2 diabetic nephropathy in humans in vivo.

ACKNOWLEDGEMENTS

Part of this work was presented at the ASN Kidney Week 2016 in Chicago. J.T.J. and P.H. are the guarantors of this work and, as such, had full access to all the data in the study and take responsibility for the integrity of the data and the accuracy of the data analysis.

REFERENCES

1. WHO. Global Status Report On Noncommunicable Diseases [article online]. http://apps.who.int/iris/bitstream/10665/148114/1/9789241564854_eng.pdf
2. de Vries AP, Ruggenti P, Ruan XZ et al. Fatty kidney: emerging role of ectopic lipid in obesity-related renal disease. *Lancet Diabetes Endocrinol* 2014; 2: 417–426
3. Klessens CQ, Woutman TD, Verraar KA et al. An autopsy study suggests that diabetic nephropathy is underdiagnosed. *Kidney Int* 2016; 90: 149–156
4. Bobulescu IA. Renal lipid metabolism and lipotoxicity. *Curr Opin Nephrol Hypertens* 2010; 19: 393–402
5. D'Agati VD, Chagnac A, de Vries APJ et al. Obesity-related glomerulopathy: clinical and pathologic characteristics and pathogenesis. *Nat Rev Nephrol* 2016; 12: 453–471
6. Guebre-Egziabher F, Alix PM, Koppe L et al. Ectopic lipid accumulation: a potential cause for metabolic disturbances and a contributor to the alteration of kidney function. *Biochimie* 2013; 95: 1971–1979
7. Gastaldelli A, Cusi K, Pettiti M et al. Relationship between hepatic/visceral fat and hepatic insulin resistance in nondiabetic and type 2 diabetic subjects. *Gastroenterology* 2007; 133: 496–506
8. Perseghin G, Scifo P, De CF et al. Intramyocellular triglyceride content is a determinant of in vivo insulin resistance in humans: a ¹H-¹³C nuclear magnetic resonance spectroscopy assessment in offspring of type 2 diabetic parents. *Diabetes* 1999; 48: 1600–1606
9. Rijzewijk LJ, van der Meer RW, Smit JW et al. Myocardial steatosis is an independent predictor of diastolic dysfunction in type 2 diabetes mellitus. *J Am Coll Cardiol* 2008; 52: 1793–1799
10. Snel M, Jonker JT, Schoones J et al. Ectopic fat and insulin resistance: pathophysiology and effect of diet and lifestyle interventions. *Int J Endocrinol* 2012; 2012: 983814
11. Bobulescu IA, Lotan Y, Zhang J et al. Triglycerides in the human kidney cortex: relationship with body size. *PLoS One* 2014; 9: e101285
12. Li Z, Woollard JR, Wang S et al. Increased glomerular filtration rate in early metabolic syndrome is associated with renal adiposity and microvascular proliferation. *Am J Physiol Renal Physiol* 2011; 301: F1078–F1087
13. Rutledge JC, Ng KF, Aung HH et al. Role of triglyceride-rich lipoproteins in diabetic nephropathy. *Nat Rev Nephrol* 2010; 6: 361–370
14. Wang XX, Jiang T, Shen Y et al. The farnesoid X receptor modulates renal lipid metabolism and diet-induced renal inflammation, fibrosis, and proteinuria. *Am J Physiol Renal Physiol* 2009; 297: F1587–F1596
15. de Heer P, Bizino MB, Lamb HJ et al. Parameter optimization for reproducible cardiac ¹H-MR spectroscopy at 3 Tesla. *J Magn Reson Imaging* 2016; 44: 1151–1158
16. Jonker JT, de Mol P, de Vries ST et al. Exercise and type 2 diabetes mellitus: changes in tissue-specific fat distribution and cardiac function. *Radiology* 2013; 269: 434–442
17. van der Meer RW, Doornbos J, Kozerke S et al. Metabolic imaging of myocardial triglyceride content: reproducibility of ¹H MR spectroscopy with respiratory navigator gating in volunteers. *Radiology* 2007; 245: 251–257
18. Hammer S, de Vries AP, de Heer P et al. Metabolic imaging of human kidney triglyceride content: reproducibility of proton magnetic resonance spectroscopy. *PLoS One* 2013; 8: e62209
19. Koopmans SJ, Schuurman T. Considerations on pig models for appetite, metabolic syndrome and obese type 2 diabetes: from food intake to metabolic disease. *Eur J Pharmacol* 2015; 759: 231–239
20. Koopmans SJ, Dekker R, Ackermans MT et al. Dietary saturated fat/cholesterol, but not unsaturated fat or starch, induces C-reactive protein associated early atherosclerosis and ectopic fat deposition in diabetic pigs. *Cardiovasc Diabetol* 2011; 10: 64
21. Dixon WT. Simple proton spectroscopic imaging. *Radiology* 1984; 153: 189–194
22. Frahm J, Merboldt KD, Hanicke W. Localized proton spectroscopy using stimulated echoes. *J Magn Reson* 1987; 72: 502–508
23. Murdoch JB, Lampman DA. Beyond WET and DRY: optimized pulses for water suppression. *Proc Intl Soc Mag Reson Med* 1993: 1191
24. Naressi A, Couturier C, Devos JM et al. Java-based graphical user interface for the MRUI quantitation package. *MAGMA* 2001; 12: 141–152
25. Bligh EG, Dyer WJ. A rapid method of total lipid extraction and purification. *Can J Biochem Physiol* 1959; 37: 911–917
26. Boesch C, Machann J, Vermathen P et al. Role of proton MR for the study of muscle lipid metabolism. *NMR Biomed* 2006; 19: 968–988

- 27.** Longo R, Pollesello P, Ricci C et al. Proton MR spectroscopy in quantitative in vivo determination of fat content in human liver steatosis. *J Magn Reson Imaging* 1995; 5: 281–285
- 28.** van derMeer RW, Hammer S, Lamb HJ et al. Effects of short-term high-fat, high-energy diet on hepatic and myocardial triglyceride content in healthy men. *J Clin EndocrinolMetab* 2008; 93: 2702–2708
- 29.** van Beek L, van Klinken JB, Pronk AC et al. The limited storage capacity of gonadal adipose tissue directs the development of metabolic disorders in male C57Bl/6Jmice. *Diabetologia* 2015; 58: 1601–1609

PART THREE
SUMMARY,
GENERAL
DISCUSSION
AND
APPENDICES

8

**SUMMARY
AND GENERAL
DISCUSSION**

SUMMARY

The aim of this thesis was to develop advanced body MR techniques that can contribute to the knowledge of the metabolic syndrome (MetS). Such techniques are important since the incidence of the metabolic syndrome is reaching pandemic proportions.

In the first part of this thesis, consisting of chapters 2, 3 and 4, new techniques for body MR were developed. Body MR is routinely conducted using MR scanners up to 1.5 T. However in the recent years, a substantial number of these 1.5 T scanners have been replaced by high field scanners (≥ 3 T). The main drive to switch to higher field scanners is that the higher magnetic field will result in a larger effective magnetization of the spins, thereby increasing the signal-to-noise ratio (SNR). Nevertheless, in body MR it is challenging to achieve this gain in SNR due to an increase in imaging artefacts. One of the causes for these artefacts is that due to decreasing wavelength of the RF signal resulting in constructive and destructive interference, it is more difficult to create a homogeneous transmit field. In **chapter two**, (Increasing Signal Homogeneity and Image Quality in Abdominal Imaging at 3 T with Very High Permittivity Materials) we addressed this problem by applying high dielectric pads which significantly reduce the coefficient of variance creating a more uniform transmit field for abdominal imaging using a 3 T MR scanner. Furthermore, the high dielectric pads decreased average power, thereby reducing the global specific absorption rate (SAR). This was the case for both the quadrature driven and the RF shimmed 3 T birdcage coil.

In **chapter three**, a similar approach (Improved Cardiac Proton Magnetic Resonance Spectroscopy at 3 T Using High Permittivity Pads) was used to increase the SNR of cardiac proton spectra. The pads were optimized using a finite time domain solver to obtain maximal RF field in the septum of the heart instead of a more homogeneous RF field over the whole heart region. In-vivo, the pads demonstrated an average increase in spectral SNR of 60%. If the SNR is high, this gain in SNR can be traded for a reduction in acquisition time by a factor of two and a half, addressing one of the biggest problems with MRS, namely the relatively long total acquisition time.

Even after optimizing the transmit field and receive sensitivity, MR spectroscopy remains technically challenging to perform reliably. This is partly due to the dynamic field fluctuations introduced by respiratory motion, and in the case of heart, cardiac motion. Furthermore, there is an inherent low SNR of the metabolites of interest as well as a great dependency on the homogeneity of the static magnetic field. For cardiac MR spectroscopy in particular, there are no standard (clinical) protocols offered by manufacturers. Since there are many parameters that significantly impact the spectral quality, designing such a scan protocol remains challenging. In **chapter four** (Parameter Optimization for Reproducible Cardiac ^1H -MR Spectroscopy at 3 Tesla) we described how cardiac proton MR spectroscopy can be optimized and measured the reproducibility of these measurements. The optimized protocol involves a local power optimization, pencil beam B_0 shimming, a cardiac trigger delay of 200 ms, pencil beam navigator-based respiratory compensation, and MOIST water suppression. Using this optimized protocol, a high intra- ($C_v = 5\%$) and intersession ($C_v = 6.5\%$) reproducibility of the myocardial triglyceride content was achieved.

In the second part of this thesis (chapters five, six and seven), the previously developed techniques were applied in clinical studies to gain additional insight in the development/treatment of the MetS. In **chapter five** (MR of Multi-Organ Involvement in the Metabolic Syndrome), a literature review of the MetS was provided, focussing on the primary organs

affected including the brain, skeletal muscle, pancreas, heart, liver and kidney. Crucial symptoms of MetS pathophysiology, ranging from ectopic lipid accumulation to end-organ damage can be evaluated using multiple MR techniques. Therefore, MR could be of added value in attempts to unravel the MetS pathophysiology as well as monitoring of therapy efficacy.

At present, much remains unknown as to how MetS affects the kidneys. Subsequently, there is a strong need for non-invasive tools to measure renal fat content. Although spectroscopy in the heart and liver has become the non-invasive gold standard for metabolite quantification, it was not yet performed in the kidneys. As with heart and liver measurements breathing complicates the application of spectroscopy in the kidney, but more importantly the limited size of the spectroscopy voxel results in low SNR. In **chapter six** (Metabolic Imaging of Human Kidney Triglyceride Content: Reproducibility of Proton Magnetic Resonance Spectroscopy), we demonstrated that MR spectroscopy can be performed in the kidney. Furthermore, we showed that pencil beam navigator respiratory triggering significantly improves both spectral quality and reproducibility.

In liver and cardiac spectroscopy several studies have been performed to validate the technique to the criterion standard; biopsy. However, to our knowledge there has been no validation study performed to test the accuracy of renal MR spectroscopy. In **chapter seven** (Metabolic imaging of fatty kidney in diabetes: validation and dietary intervention), we validated this technique by comparing lipid measurements using renal proton MR spectroscopy with biopsies of porcine kidneys. The lipids measured by proton MR spectroscopy and the enzymatic assay (biopsy) correlated significantly ($r=0.86$, $p < 0.0001$). In addition, the effects of dietary intervention on the renal lipids were measured. One group was fed a regular diet (group A), one a high lipid diet (group B) and a third group followed the same high lipid diet combined with a low-dose of streptozocin (group C) to induce insulin-independent diabetes. After the 9-month diet, the renal lipids in group C (high lipid diet combined with streptozocin) were significantly higher compared to group A (regular diet). Renal lipids were not significantly different between group B (high lipid diet) and group A (regular diet).

GENERAL DISCUSSION

PART ONE: TECHNICAL DEVELOPMENTS - HIGH FIELD BODY MR

Body MR can benefit from higher field strengths (3 T and higher) but often acquisition protocols cannot directly be transferred from lower field scanners since the increase in field strength introduces new artefacts, in addition to exacerbating the existing ones. Therefore, it can be challenging to achieve the theoretical improvements in image and spectral quality. These artefacts are to a large extent caused by the shortening of the wavelength of the transmit (RF) field in comparison to the size of the imaging object. The RF field then constructively and destructively adds causing hyper and hypointense areas in the image.

This problem of decreased transmit homogeneity has been addressed by MR manufacturers by the introduction of multi-transmit systems. Alternatively, it has been shown that in neuro and cardiac imaging dielectric pads can be used to homogenize the transmit field.^{29,59} In this thesis a new application of the pads in abdominal imaging was examined. When using the high dielectric pads for liver imaging, the shading artefacts (caused by the inhomogeneous transmit field) have been reduced resulting in higher image quality. In particular, the high dielectric pads may be of added value in patients with ascites or pregnant women, where effect of such shading artefacts is the highest. Application of these pads could be the difference between an unusable and an useful scan for the radiologist.

In this thesis, we have shown that the high dielectric materials used for passive shimming can also be applied in MR spectroscopy to increase the signal-to-noise ratio. When designing such pads for MRS, maximal transmit/receive sensitivity is a more important optimization parameter than transmit inhomogeneity since the MRS voxel is small in contrast to regular imaging. This results in pads that are of higher permittivity and thicker than the pads used when the main optimization parameter is the homogeneity of the transmit field. By applying these pads for cardiac spectroscopy, an increase of 60% in SNR was achieved. This effect was predominantly attributed to an increase in receive sensitivity. This effect will most likely also translate to spectroscopy of other organs, however, additional studies are needed. Furthermore, although passive radiofrequency shimming increases image and spectral quality, the dielectric pads have to be placed on the patient which is an extra step that limits implementation feasibility in the clinic.

Moreover, correct placement of the dielectric pads requires the MR operator to have a basic knowledge about the methodology of the pads. A potential solution to this problem could be to incorporate the dielectric pads into phased array receive coils.

MR spectroscopy is known to be a challenging technique to perform in the body and the reproducibility is often a major concern. As shown in this thesis, many variables can affect the reproducibility of MR spectroscopy. For example, respiratory triggering is an important factor that should be addressed carefully. At present, most studies use breath holds or a pencil beam navigator at the lung-liver interface to address this problem. When using breath holds, it is known that the amount of air in the lungs varies between subsequent breath holds resulting in variation of the location of the volume of interest between the breath holds and thus decreases the reproducibility. Furthermore, a breath hold scan is not ideal for body scans in clinical populations since patients often have reduced breath-holding capability. Application of a pencil beam navigator is better suited for MRS acquisitions since it triggers the spectroscopy sequence consistently in the same respiratory state without the need for breath-holds. Unfortunately even though such a

pencil beam navigator is standard practice for body imaging the MR manufacturers do not offer this function for spectroscopy. The navigator can be made available by adapting the scanner software but not all research groups have access to the scanner software. Secondly, a pencil beam navigator can only track the lung liver interface in one dimension (lung-liver interface in feet-head direction). This may be sufficient when measuring the liver, but the movement of other organs like the heart and kidneys have to be estimated from this indirect respiratory measurement. Nonetheless, in this thesis we have shown that the current 1D implementation of the navigator allows for reproducible cardiac spectra, although it would be more optimal if the navigator could track the 3D displacement of the organ of interest. Such a 3D navigator would also decrease the need for the subject to lie perfectly still in the scanner since it is often challenging for patients to lay completely still throughout an entire scan session (from the acquisition of the spectroscopy planning scan until the end of the spectroscopy acquisition). When a patient has moved substantially, it can lead to incorrect lipid quantification when peri-organ adipose tissue becomes included in the MRS voxel due to the movement. This can be confirmed by acquiring an additional post-MRS plan scan or in the post processing of the separate averages of the spectroscopy data.

Another variable of great importance for the reproducibility of MRS is the power optimization. If the power of the excitation is over or underestimated, the desired flip angle will not be reached which will result in a signal loss. This signal loss in single voxel spectroscopy (eg. PRESS, STEAM) is, due to the multiple refocussing pulses, much higher than most imaging sequences. When looking solely to the signal dependence on the flip angle for the STEAM it can be described by,

$$S(\theta)_{STEAM} = S_0 \sin \theta_1 \sin \theta_2 \sin \theta_3 \quad (\text{Equation 1})$$

where S_0 is the signal when flip angles $\theta_{1-3} = \pi/2$.⁶⁰⁻⁶¹ For the PRESS sequence the signal dependence to the flip angle is even greater due to the two 180 degree refocusing pulses. Here the signal equation becomes,

$$S(\theta)_{PRESS} = S_0 \sin \theta_1 \sin^2 (\theta_2/2) \sin^2 (\theta_3/2) \quad (\text{Equation 2})$$

where S_0 is the signal when flip angle $\theta_1 = \pi/2$ and $\theta_{2-3} = \pi$.⁶²⁻⁶⁴ For example, when the deviation of the flip angle is 20% when using the PRESS sequence, this will result in a signal loss of approximately 22%. This loss in signal will have a strong impact on the reproducibility stressing the need for a good power optimization. In this thesis we compared the standard system "global" power optimization with "local" power optimization. Global in this case refers to the fact that power optimization is performed by integrating the signal intensity over an entire transverse slice through the heart, whereas local applies only to the spectroscopic VOI. Local power optimization method was performed by monitoring the intensity of the water peak and incrementing the tip angles of the excitation pulse and the two refocusing pulses in the PRESS sequence in steps of 5% (range, 90%–150% of the global power optimization result), and choosing the power which produced the maximum signal intensity. In terms of SNR, using local rather than global power optimization showed a significant increase. Local power optimization requires no changes to the system software, and so is easy to implement in a clinical setting. We observed that the power underestimation from a global power measurement was

greatest in subjects with either high body mass index or athletic subjects with high lung volume, but further study would be required to confirm this observation.

Even though MR spectroscopy has been used for several decades in organs like the liver and heart, little research has been conducted examining whether this technique can be applied in the kidney as well. This thesis showed that MR spectroscopy of the human kidney for detection of cortical triglyceride content is feasible. However, it remains challenging to apply renal MR spectroscopy since the limited maximum size of the spectroscopy voxel as well as very low lipid levels in the kidney cortex result in a low SNR with a subsequent need for many signal averages to get sufficient SNR. Secondly, kidney tissue is not homogenous with substantial anatomical and functional variation between cortex and medulla as well as glomeruli and tubuli. Finally, due to the close proximity of lipid contamination sources such as sinus and perirenal lipids, accurate voxel placement and reliable respiratory triggering are of great importance. To improve voxel planning, a fat image from a water-fat acquisition can be used since the contaminating sources are clearly visible. For respiratory triggering, a pencil beam navigator is preferred, although a 3D navigator might prove even more valuable since the kidney is relatively far from the lung liver interface. However, with kidney spectroscopy, small motion artefacts can still remain. Therefore, in post processing, averages should be analysed separately to confirm that none of the averages are contaminated by perirenal or sinus lipids.

At present, clinical application of MRS is mostly limited to neurology and the prostate.^{65,66} In this thesis, a main challenge of implementation of the technique was overcome; the reproducibility. It was shown that both in the heart, as well as the kidney it is possible to acquire good quality and reliable spectra. Furthermore, it was shown that in porcine kidneys, the MR spectroscopy triglyceride levels strongly correlated with 'criterion standard' enzymatic assessment of triglyceride content. This opens up new possibilities to extend the (clinical) application of body MR spectroscopy.

However, the complexity of the acquisition and post-processing also contribute to the difficulties in the application of body MR spectroscopy. At present, the acquisition and reconstruction of MR spectroscopy requires extensive knowledge about the technique to obtain reliable results. In order to achieve a broader implementation of body MR spectroscopy, MR manufacturers need to play an important role since apart from the liver spectroscopy, no protocols are offered by the MR manufacturers for body MR spectroscopy. Moreover, on-scanner reconstruction and post-processing methods for spectroscopy data are limited and in most cases, off-line post-processing and analysis of the spectra is required.^{67,68} Finally, the aforementioned 3D navigator that can track the separate organs could contribute to further improvement of reproducibility and support a wider application of body MR in general.

PART TWO: CLINICAL APPLICATIONS - METABOLIC SYNDROME

MetS is a systemic disease with a complex pathophysiology including insulin resistance, atherogenic dyslipidemia, hypertension, ectopic lipid accumulation, low-grade inflammation, prothrombotic state, and fibrosis resulting in end-organ damage.⁴⁸ Application of the techniques and optimizations described in this thesis, functional and structural consequences of MetS can be evaluated with MR throughout the entire body.

Using a porcine model, we demonstrated that renal triglyceride content increased over the metabolic spectrum in conjunction with hepatic triglycerides. Previous studies have shown a correlation between increased bodyweight and increased hepatic and renal

triglyceride content in both animals and humans.^{53,56} We observed similar trends, with increasing triglyceride content in the diabetic type 2 group. Using Oil Red O staining it was shown that renal lipid accumulation was most prominent in renal tubuli, albeit some lipid staining was also observed in the glomeruli. This is in accordance with a recent study of human nephrectomies, where lipid droplets were predominantly found in tubule cells and to a lesser extent in the glomeruli.⁵⁶

OVERALL CONCLUSION OF THIS THESIS

As part of the present thesis advanced MR techniques were developed, including development and application of high dielectric materials for body MR imaging and spectroscopy, resulting in improved signal-to-noise ratio and reproducibility. These technical advances were used to study the metabolic syndrome, showing dietary effects on renal fat content.

REFERENCES

1. Despres JP, Lemieux I. Abdominal obesity and metabolic syndrome. *Nature* 2006;444(7121):881-7
2. Johnson NA, Walton DW, Sachinwalla T, et al. Noninvasive assessment of hepatic lipid composition: advancing understanding and management of fatty liver disorders. *Hepatology*. 2008;47:1513-1523.
3. Szczepaniak LS, Nurenberg P, Leonard D, et al. Magnetic resonance spectroscopy to measure hepatic triglyceride content: prevalence of hepatic steatosis in the general population. *Am J Physiol Endocrinol Metab*. 2005;288:E462-E468.
4. Thomas EL, Hamilton G, Patel N, et al. Hepatic triglyceride content and its relation to body adiposity: a magnetic resonance imaging and proton magnetic resonance spectroscopy study. *Gut*. 2005;54: 122-127.
5. van Werven JR, Hoogduin JM, Nederveen AJ, et al. Reproducibility of 3.0 Tesla magnetic resonance spectroscopy for measuring hepatic fat content. *J Magn Reson Imaging*. 2009;30:444-448.
6. Machann J, Stefan N, Schick F. (1)H MR spectroscopy of skeletal muscle, liver and bone marrow. *Eur J Radiol*. 2008;67:275-284.
7. van der Meer RW, Doornbos J, Kozerke S, et al. Metabolic imaging of myocardial triglyceride content: reproducibility of 1H MR spectroscopy with respiratory navigator gating in volunteers. *Radiology* 2007; 245:251-257.
8. Felblinger J, Jung B, Slotboom J, Boesch C, Kreis R. Methods and reproducibility of cardiac/respiratory double-triggered (1)H-MR spectroscopy of the human heart. *Magn Reson Med* 1999;42:903-910.
9. Szczepaniak LS, Dobbins RL, Metzger GJ, et al. Myocardial triglycerides and systolic function in humans: in vivo evaluation by localized proton spectroscopy and cardiac imaging. *Magn Reson Med* 2003;49:417-423.
10. Ith M, Stettler C, Xu J, Boesch C, Kreis R. Cardiac lipid levels show diurnal changes and long-term variations in healthy human subjects. *NMR Biomed* 2014;27:1285-1292.
11. Fuss TL, Cheng LL. Evaluation of Cancer Metabolomics Using ex vivo High Resolution Magic Angle Spinning (HRMAS) Magnetic Resonance Spectroscopy (MRS). *Metabolites*. 2016 Mar 22;6(1). pii: E11. doi: 10.3390/metabo6010011.
12. Ulmer S1, Backens M, Ahlhelm FJ. Basic Principles and Clinical Applications of Magnetic Resonance Spectroscopy in Neuroradiology. *J Comput Assist Tomogr*. 2016 Jan-Feb;40(1):1-13. doi: 10.1097/RCT.0000000000000322.
13. in 't Zandt H1, van Der Graaf M, Heerschap A. Common processing of in vivo MR spectra. *NMR Biomed*. 2001 Jun;14(4):224-32.
14. Drost DJ1, Riddle WR, Clarke GD; AAPM MR Task Group #9. Proton magnetic resonance spectroscopy in the brain: report of AAPM MR Task Group #9. *Med Phys*. 2002 Sep;29(9):2177-97.
15. Teeuwisse WM1, Brink WM, Webb AG. Quantitative assessment of the effects of high-permittivity pads in 7 Tesla MRI of the brain. *Magn Reson Med*. 2012 May;67(5):1285-93. doi: 10.1002/mrm.23108. Epub 2011 Aug 8.
16. Brink WM, Webb AG. High permittivity pads reduce specific absorption rate, improve B1 homogeneity, and increase contrast-to-noise ratio for functional cardiac MRI at 3 T. *Magn Reson Med*. 2014 Apr;71(4):1632-40. doi: 10.1002/mrm.24778.
17. Brink WM, van der Jagt AM, Versluis MJ, Verbist BM, Webb AG. High permittivity dielectric pads improve high spatial resolution magnetic resonance imaging of the inner ear at 7 T. *Invest Radiol*. 2014 May;49(5):271-7. doi: 10.1097/RLI.0000000000000026.
18. Brink WM, Versluis MJ, Peeters JM, Börnert P, Webb AG. Passive radiofrequency shimming in the thighs at 3 Tesla using high permittivity materials and body coil receive uniformity correction. *Magn Reson Med*. 2016 Dec;76(6):1951-1956. doi: 10.1002/mrm.26070.

**DUTCH SUMMARY /
NEDERLANDSE
SAMENVATTING**

NEDERLANDSE SAMENVATTING

Het doel van dit proefschrift was om geavanceerde MR-technieken te ontwikkelen die kunnen bijdragen aan de kennis van het metabool syndroom (MetS). Dergelijke technieken zijn belangrijk omdat in de afgelopen jaren de incidentie van het metabool syndroom pandemische proporties heeft bereikt.

In het eerste deel van dit proefschrift, bestaande uit de hoofdstukken 2, 3 en 4, zijn nieuwe technieken ontwikkeld die toegepast kunnen worden in het afbeelden en meten van de organen van het bovenlichaam, ook wel genaamd "Body MR". Body MR wordt routinematig uitgevoerd met MR-scanners met een veldsterkte van 1,5 T. In de afgelopen jaren is echter een aanzienlijk deel van deze 1,5 T-scanners vervangen door hoge veldscanners (≥ 3 T). De belangrijkste reden om over te schakelen naar hoge veldscanners is dat het hogere magnetische veld resulteert in een grotere effectieve magnetisatie van de spins, waardoor de signaal-ruisverhouding (SNR) toeneemt. Desalniettemin is het in Body MR een uitdaging om deze toename in SNR te bereiken als gevolg van een toename van imaging-artefacten bij een hoger magnetisch veld.

Een van de oorzaken van deze artefacten is dat de golflengte van het zend signaal korter wordt wat resulteert in constructieve en deconstructieve interferentie. Dit maakt het moeilijker is om een homogeen zend veld te creëren dat nodig is voor een artefact vrije afbeelding. In **hoofdstuk twee** (Increasing Signal Homogeneity and Image Quality in Abdominal Imaging at 3 T with Very High Permittivity Materials) is dit probleem aangepakt door sterk diëlektrische kussens toe te passen die de variantie coëfficiënt aanzienlijk verminderen, waardoor een meer uniform zend veld wordt gecreëerd met behulp van een 3 T MR-scanner. Tevens verlagen de sterk diëlektrische kussens het gemiddeld benodigde zend vermogen, waardoor de globale gemiddeld opgenomen vermogen (SAR) wordt verlaagd. Dit was het geval voor zowel de in quadratuur aangestuurde alsmede de RF shimmed 3 T zend spoel.

In **hoofdstuk drie** werd een vergelijkbare benadering (Improved Cardiac Proton Magnetic Resonance Spectroscopy at 3 T Using High Permittivity Pads) gebruikt om de SNR van cardiale MR proton spectra te verhogen. De kussens werden geoptimaliseerd met behulp van een eindige differentie methode in het tijd domein (FDTD) om een maximaal RF-veld in het kamertussenschot van het hart te verkrijgen in plaats van een homogeen zend veld over het gehele hartgebied. In vivo vertoonden de sterk diëlektrische kussens een gemiddelde toename in spectrale SNR van 60%. Mits de SNR hoog genoeg is, kan deze winst in SNR worden geruild voor een verkorting van de acquisitietijd met een factor van tweeënhalf, waarbij één van de grootste problemen met MR spectroscopie wordt aangepakt, namelijk de relatief lange totale acquisitietijd.

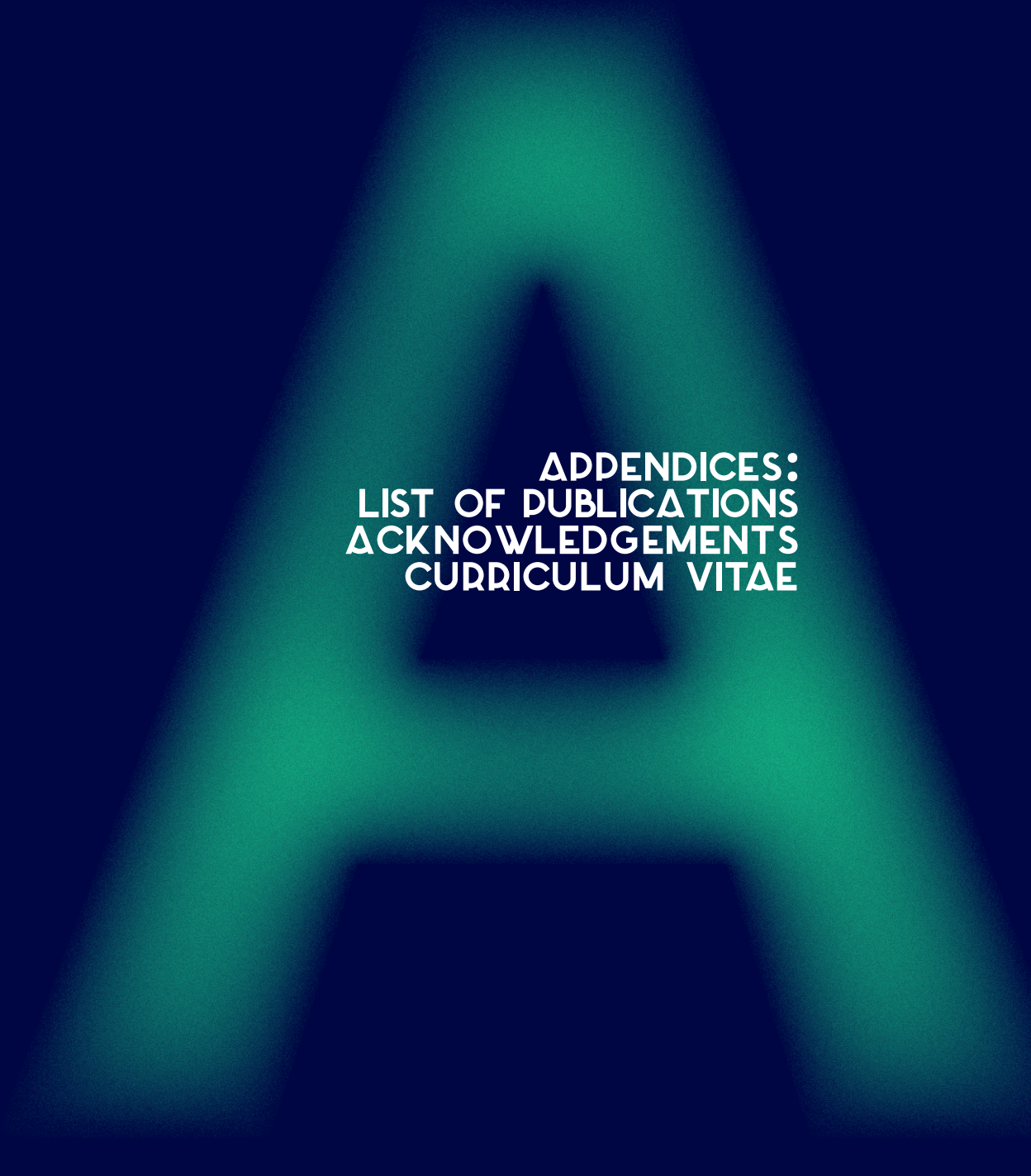
Zelfs na het optimaliseren van het zendveld en de ontvangstgevoeligheid met behulp van de diëlektrische kussens, blijft body MR-spectroscopie technisch gezien uitdagend om betrouwbaar uit te voeren. Dit is gedeeltelijk te wijten aan de dynamische veldfluctuaties geïntroduceerd door de ademhalingsbeweging, en in het geval van het hart, de hartbeweging. Verder is er een inherent lage SNR van de relevante metaboliëten en een grote afhankelijkheid van de homogeniteit van het statische magnetische veld. Met name voor cardiale MR spectroscopie zijn er geen standaard (klinische) protocollen die door MR fabrikanten worden aangeboden. Omdat er veel parameters zijn die de spectrale kwaliteit aanzienlijk beïnvloeden, blijft het ontwerpen van zo'n scanprotocol een uitdaging. In **hoofdstuk vier** (Parameter Optimization for Reproducible Cardiac 1H-MR Spectroscopy at 3 Tesla) is beschreven hoe cardiale proton MR-spectroscopie kan worden geoptimali-

seerd en de reproduceerbaarheid van deze metingen bepaald. Het geoptimaliseerde protocol omvat een lokaal zend vermogen optimalisatie, statisch veld homogenisatie (B_0 -shimming) met behulp van negen projecties door het shimvolume, een meet vertraging van 200 ms na de R-top van het ECG, op navigator gebaseerde respiratie compensatie en MOIST-wateronderdrukking. Met behulp van dit geoptimaliseerde protocol werd een hoge intra- ($C_v = 5\%$) en inter-sessie ($C_v = 6,5\%$) reproduceerbaarheid van de MTGC bereikt. In het tweede deel van dit proefschrift (hoofdstukken vijf, zes en zeven) zijn de eerder ontwikkelde technieken toegepast in klinische studies om extra inzicht te krijgen in de ontwikkeling / behandeling van het metabool syndroom (MetS). In **hoofdstuk vijf** (MR of Multi-Organ Involvement in the Metabolic Syndrome) werd een literatuuroverzicht van het MetS gegeven, met de nadruk op de primaire organen waaronder de hersenen, skeletspier, pancreas, hart, lever en nier. Cruciale symptomen van MetS-pathofysiologie, lopend van ectopische lipide accumulatie tot onherstelbare orgaan schade, kunnen worden geëvalueerd met behulp van verscheidene MR-technieken. Daarom zou MR van toegevoegde waarde kunnen zijn bij het ontrafelen van de MetS-pathofysiologie, evenals bij het monitoren van de van therapieën.

Op dit moment is er nog veel onbekend over hoe MetS de nier beïnvloedt. Hierdoor is er een sterke behoefte aan niet-invasieve hulpmiddelen om het vetgehalte van de nier te meten.

Hoewel spectroscopie in het hart en de lever de niet-invasieve gouden standaard is voor het meten van het vetgehalte, werd deze techniek nog niet toegepast op de nier. Net als hart- en levermetingen bemoeilijkt ademhaling de toepassing van spectroscopie in de nier.

Daarnaast is bij nier spectroscopie het voxel kleiner vanwege de beperkte ruimte in de cortex van de nier wat resulteert in een zeer lage SNR. Ondanks deze uitdagingen wordt in **hoofdstuk zes** (Metabolic Imaging of Human Kidney Triglyceride Content: Reproducibility of Proton Magnetic Resonance Spectroscopy) aangetoond dat MR-spectroscopie in de nier kan worden uitgevoerd. Verder is aangetoond dat de navigator gebaseerde respiratie triggering zowel de spectrale kwaliteit als de reproduceerbaarheid aanzienlijk verbetert. In lever- en hartspectroscopie zijn verschillende onderzoeken uitgevoerd om de MR spectroscopie te valideren aan de gouden standaard; biopsie. Voor zover bekend was er echter geen validatiestudie uitgevoerd om de nauwkeurigheid van renale MR-spectroscopie te testen. In **hoofdstuk zeven** (Metabolic imaging of fatty kidney in diabetes: validation and dietary intervention) hebben we deze techniek gevalideerd met behulp van varkensnieren door de MR-spectroscopie lipide metingen te vergelijken met de vetbepaling uit biopten. De lipiden gemeten met proton MR-spectroscopie en de enzymatische test (biopsie) waren significant gecorreleerd ($r = 0,86$, $p < 0,0001$). Bovendien werden de effecten van dieetinterventie op de nier lipiden gemeten. Eén groep kreeg een normaal dieet (groep A), één een vetrijk dieet (groep B) en een derde groep volgde hetzelfde vetrijke dieet gecombineerd met een lage dosis streptozocine (groep C) om insuline-onafhankelijke diabetes te induceren. Na het 9-maanden durende dieet waren de renale lipiden in groep C (hoog-lipidedieet gecombineerd met streptozocine) significant hoger in vergelijking met groep A (normaal dieet). Nierlipiden waren niet significant verschillend tussen groep B (hoog lipidedieet) en groep A (gewoon dieet).



**APPENDICES:
LIST OF PUBLICATIONS
ACKNOWLEDGEMENTS
CURRICULUM VITAE**

LIST OF PUBLICATIONS

Journal Publications

IA Dekkers, **P de Heer**, MB Bizino, APJ Vries, HJ Lamb. ^1H -MRS for the assessment of renal triglyceride content in humans at 3T: A primer and reproducibility study. *Journal of Magnetic Resonance Imaging* 2018 Mar 8. doi: 10.1002/jmri.26003

JT Jonker *, **P de Heer** *, MA Engelse, EH van Rossenberg, CQF Klessens, HJ Baelde, IM Bajema, S Koopmans, PG Coelho, TCM Streefland, AG Webb, IA Dekkers, TJ Rabelink, PCN Rensen, HJ Lamb, APJ de Vries. Metabolic imaging of fatty kidney in diabetes: validation and dietary intervention. *Nephrology Dialysis Transplantation* 2018 Feb 1;33(2):224-230. doi: 10.1093/ndt/gfx243 [* shared first author]

P de Heer, MB Bizino, HJ Lamb, AG Webb. Parameter optimization for reproducible cardiac 1H-MR spectroscopy at 3 Tesla. *Journal of Magnetic Resonance Imaging* 2016 Nov;44(5):1151-1158. doi: 10.1002/jmri.25254.

P de Heer, MB Bizino, MJ Versluis, AG Webb, HJ Lamb. Improved Cardiac Proton Magnetic Resonance Spectroscopy at 3 T Using High Permittivity Pads. *Investigative radiology* 2016 Feb;51(2):134-8. doi: 10.1097/RLI.0000000000000214

MB Bizino, ML Sala, **P de Heer**, P van der Tol, JW Smit, AG Webb, A de Roos, HJ Lamb. MR of Multi-Organ Involvement in the Metabolic Syndrome. *Magnetic Resonance Imaging Clinics of North America* 2015 Feb;23(1):41-58. doi: 10.1016/j.mric.2014.09.010.

S Hammer, APJ de Vries, **P de Heer**, MB Bizino, R Wolterbeek, TJ Rabelink, J Doornbos, HJ Lamb. Metabolic imaging of human kidney triglyceride content: reproducibility of proton magnetic resonance spectroscopy. *PLoS one* 2013 Apr 19;8(4):e62209. doi: 10.1371/journal.pone.0062209

P de Heer, WM Brink, BJ Kooij, AG Webb. Increasing signal homogeneity and image quality in abdominal imaging at 3 T with very high permittivity materials. *Magnetic Resonance in Medicine* 2012 Oct;68(4):1317-24. doi: 10.1002/mrm.24438.

Conference Proceedings

P de Heer, WM Brink, BJ Kooij, AG Webb. Increasing B1+ homogeneity in abdominal imaging at 3T with high dielectric materials
- ISMRM Benelux 2012, oral presentation

P de Heer, WM Brink, AG Webb. Polarization Effect of Dielectric Shimming for Abdominal Imaging at 3T and Neuro Imaging at 7T.
- ISMRM Benelux 2013, poster presentation

P de Heer, HJ Lamb, AG Webb. Improved Cardiac 1H-MR Spectroscopy at 3 T using High Permittivity Materials.
- RSNA 2014, oral presentation
- ISMRM Benelux 2014, oral presentation
- ISMRM 2015, oral presentation, Magna Cum Laude Award

P de Heer, Jacqueline T Jonker, Evelien H van Rossenberg, Marten A Engelse, Trea CM Streefland, Ton J Rabelink, Andrew G Webb, Patrick CN Rensen, Hildo J Lamb, Aiko PJ de Vries. Metabolic Imaging of Renal Triglyceride Content: Validation by Porcine Kidney Biopsies.
- ISMRM 2015, poster presentation
- ISMRM Benelux 2015, poster presentation

Paul de Heer, Maurice B. Bizino, Hildo J. Lamb, Andrew G. Webb. Parameter Optimization for Reproducible Cardiac 1H-MR Spectroscopy at 3 T.
- ISMRM 2016, Electronic-poster presentation
- ISMRM Benelux 2016, Poster presentation

Paul de Heer, Jos Oudeman, Aart J Nederveen, Andrew G Webb. Improved MR Neurography of the Brachial Plexus Using High Permittivity Pads.
- ISMRM 2016, Poster presentation

Paul de Heer, Robert Hemke, Cristina Lavini, Jasper Schoormans, Bram Coolen, Anouk Barendregt, Gustav Strijkers, Mario Maas, Jaap Stoker, Aart Nederveen, Jurgen Runge. Feasibility of GRASP DCE-MRI in children with Juvenile Idiopathic Arthritis.
- ISMRM 2017 - Electronic-poster presentation
- ISMRM Benelux 2017 - Poster presentation

Paul de Heer, Oliver Gurney-Champion, Jurgen Runge, Remy Klaassen, Jasper Schoormans, Bram Coolen, Hanneke van Laarhoven, Gustav Strijkers, Jaap Stoker, Aart Nederveen. Free Breathing T2* Mapping of the Liver Using a Compressed Sensing Reconstruction.
- ISMRM 2017 - Power-pitch presentation.
- ISMRM Benelux 2017 - Poster presentation.

Paul de Heer, Anne-Sophie van Schelt, Jasper Schoormans, Gustav J. Strijkers, Bram F. Coolen, Jurgen H. Runge, Jaap Stoker, Aart J. Nederveen. Respiratory binning showdown: self-gated, respiration belt or pencil beam?
- ISMRM 2018 - Poster presentation.
- ISMRM Benelux 2018 - Poster presentation.

ACKNOWLEDGEMENTS

Het succesvol volbrengen van een PhD is een uitdagend traject dat voor mij niet mogelijk was geweest zonder alle geweldige mensen om mij heen. Tijdens je promotie traject zijn er zo veel mooie mensen die impact hebben op je leven en ik wil die graag allemaal bedanken voor alle steun op het professionele vlak maar ook juist voor de gezelligheid op en naast de werkvloer.

Ik wil graag alle vrijwilligers bedanken die ik in al die jaren heb verveeld met talloze adempauzes en natuurlijk de ECG plakkers die altijd weer een uitdaging zijn om te verwijderen.

Verder wil ik alle geweldige collega's van het Gorter centrum. bedanken voor alle mooie tijden die we samen beleefd hebben, de verscheidene conferenties die we bezocht hebben, en de afleiding aan het einde van de week. Ik denk nog met veel plezier terug aan onze gezellige avonden in Lemmy's.

Andrew, bedankt voor alle adviezen en begeleiding tijdens mijn PhD en na vier jaar onder jouw begeleiding gewerkt te hebben is het nog steeds een raadsel hoe je met zo een volle agenda toch nog altijd tijd vind om altijd direct klaar te staan. Verder is het inspirerend geweest hoe jouw ogenschijnlijke simpele (praktische) oplossingen altijd verreweg het beste resultaat opleveren. Hildo, jouw enthousiasme en constante toevoer van nieuwe ideeën werkt als een goede motivatie om meer uit je data en ontwikkelingen te halen. Dankzij jou ben ik in contact gekomen met het mooie onderwerp spectroscopie waar ik heerlijk mijn ei in kwijt kon. Aiko bedankt voor je begeleiding en het verbreden van mijn klinische kennis. Je kon de technische verhalen van mij altijd mooi transleren naar een klinisch verhaal.

Jacqueline als ik aan de onze samenwerking denk moet ik meteen aan de tripjes die gedaan moesten worden om onze varkens nieren te bemachtigen. Dank je wel voor de fijne samenwerking met een prachtig resultaat. Beste Joost bedankt voor de hulp met het uitsplitsen van een proton spectra. Ik ben nog ver van een volledige scheikundige maar inmiddels voel ik me comfortabel rond de CH²tjes. Pieter in het begin moet je wel gedacht hebben daar heb je weer zo een PhDer die zelf moet gaan scannen maar met jouw uitleg en assistentie was het scannen van een 4-kamer een fluitje van een cent. Maurice, dank je wel voor onze geweldige samenwerking. We hebben samen wat uurtjes achter de scanner doorgebracht om nieuwe patches te testen. Hopelijk heb je geen trauma over gehouden van de woordjes "Goed nieuws! Ik heb weer een nieuwe patch gemaakt!". Maarten bedankt voor de onmisbare assistentie met het ontcijferen van de scanner software. De hoeveelheid kennis die jij standaard paraat heb is onvoorstelbaar!

Lieve AMC collega's, toen ik begon bij het AMC voelde het als een warm bad. Binnen enkele weken voelde het al alsof ik er jaren rond liep! Heerlijk om met zulke talentvolle mensen te werken die ook lekker gek kunnen zijn! Aart wat heb je een geweldige groep mensen bij elkaar gekregen op ZO. Dank ook voor de mogelijkheid om op ZO mijn carrière voort te zetten, dit keer in imaging want verandering van spijs doet eten.

Joep en Jason. Op de TU waren wij de drie praktische buitenbeentjes die stiekem ook altijd lekker wilde knutselen naast al die academische stof. Daarnaast had ik voor de TU nog weinig geproefd van het studentenleven maar samen met jullie heb ik dat dubbel en dwars ingehaald. Joep geweldig ook dat wij nog samen onze PhD in MR hebben kunnen doen, het was altijd super om met je te sparren. Geweldig dat ik tijdens mijn verdediging op je kan rekenen als paranymf. Verder wil ook de Den Haag club voor de broodnodige afleiding met feestjes en de geweldige jaarlijkse traditie "Ardennen weekend". Jullie hebben mij geleerd om niet altijd alles en vooral jezelf niet al te serieus te nemen. Vincent en Thys heerlijk dat wij dezelfde 'uitlaat' klep delen samen met Joep en Jason. Voorheen waren we altijd vooral aan het dromen van grote avonturen maar met ons clubje is het eindelijk gelukt om dit te verwezenlijken. Op naar ons volgend avontuur. William en Sander jullie ook bedankt voor de niet MR gerelateerde "congressen". Italiano aka Dennis, dank je wel voor al je hulp met het ontwerp van zowel de binnen als buitenkant van deze thesis. Het is echt een prachtig boekwerk geworden wat me zonder jou niet was gelukt. Verder wil ik ook de rest van de maatjes uit Heemskerk bedanken. We zien elkaar misschien niet meer zo vaak maar al we elkaar weer zien is het altijd weer als vanouds.

Uiteraard wil ook mijn familie bedanken voor de interesse die jullie altijd hebben getoond in mijn promotie wanneer we elkaar weer zagen. Linda, lieve zus, wat mooi dat jij straks als paranymf naast mij staat. Met jou en Joep naast me kan ik niet meer falen. Dank je wel ook voor alle gezelligheid, adviezen en steun die je als mijn "grote" zus hebt gegeven. Pap en Mam, bedankt dat jullie mij altijd onvoorwaardelijk gesteund hebben. Jullie motto van het maakt niet uit wat je doet als je maar gelukkig ben is iets wat ik mijn leven lang zal volgen. Ouders kan je niet kiezen maar zelfs als dat het geval was had ik jullie zeker nog steeds als ouders gehad!

CURRICULUM VITAE

Paul de Heer werd op 22 juni 1983 geboren in Heemskerk. In 1999 behaalde hij zijn diploma elektrotechniek aan de lagere technische school in IJmuiden. Hierna begon hij aan zijn middelbaar beroepsonderwijs elektrotechniek aan het Nova college in Santpoort-Noord waar hij zijn diploma behaald in 2003. Na het afronden van zijn MBO elektrotechniek startte hij met de versnelde bacheloropleiding elektrotechniek aan InHolland Alkmaar. Deze ronde hij af waarna hij zijn academische carrière voortzette op de TU Delft en begon met een pre-master opleiding. Tijdens deze periode heeft hij een internship van zeven maanden gedaan bij Philips Research in Shanghai. Na het succesvol afronden van de pre-master opleiding start hij in 2008 met de masteropleiding Electrical Engineering met de specialisatie in telecommunicatie. Naast zijn studie was hij werkzaam bij Mapper Lithography waar hij meewerkte aan de bouw van de aansturing van een elektronen lithografie machine. Voor zijn eindstage had hij de mogelijkheid om bij het LUMC onderzoek te doen naar hoog diëlektrische materialen die toegepast kunnen worden voor het verbeteren van abdominale afbeeldingen met behulp van de MRI scanner. Dit leidde in 2012 tot een PhD positie binnen de Radiologie afdeling van het LUMC. Onder de begeleiding van Prof. Andrew Webb, Prof. Hildo Lamb en Dr. Aiko de Vries heeft hij onderzoek gedaan naar nieuwe MR beeldvormende en spectroscopie technieken die kunnen assisteren bij diagnosticeren van abdominale afwijkingen. Momenteel is Paul aangesteld als postdoctorale onderzoeker bij Prof. Aart Nederveen in het Academisch Medisch Centrum Amsterdam. Hier werkt hij aan de klinische implementatie van versnellings technieken voor het afbeelden van abdominale organen.

